12-2014

Hi-Fidelity Simulation of the Self-Assembly and Dynamics of Colloids and Polymeric Solutions with Long Range Interactions

Mahdy Malekzadeh Moghani
University of Tennessee - Knoxville, mmalekza@vols.utk.edu

To the Graduate Council:

I am submitting herewith a dissertation written by Mahdy Malekzadeh Moghani entitled "Hi-Fidelity Simulation of the Self-Assembly and Dynamics of Colloids and Polymeric Solutions with Long Range Interactions." I have examined the final electronic copy of this dissertation for form and content and recommend that it be accepted in partial fulfillment of the requirements for the degree of Doctor of Philosophy, with a major in Chemical Engineering.

Bamin Khomami, Major Professor

We have read this dissertation and recommend its acceptance:

Brian J. Edwards, Stephen J. Paddison, Dibyendu Mukherjee

Accepted for the Council:

Carolyn R. Hodges

Vice Provost and Dean of the Graduate School

(Original signatures are on file with official student records.)

12-2014

Hi-Fidelity Simulation of the Self-Assembly and Dynamics of Colloids and Polymeric Solutions with Long Range Interactions

Mahdy Malekzadeh Moghani
University of Tennessee - Knoxville, mmalekza@vols.utk.edu

To the Graduate Council:

I am submitting herewith a dissertation written by Mahdy Malekzadeh Moghani entitled "Hi-Fidelity Simulation of the Self-Assembly and Dynamics of Colloids and Polymeric Solutions with Long Range Interactions." I have examined the final electronic copy of this dissertation for form and content and recommend that it be accepted in partial fulfillment of the requirements for the degree of Doctor of Philosophy, with a major in Chemical Engineering.

<div align="right">Bamin Khomami, Major Professor</div>

We have read this dissertation and recommend its acceptance:

Brian J. Edwards, Stephen J. Paddison, Dibyendu Mukherjee

<div align="right">Accepted for the Council:
<u>Carolyn R. Hodges</u></div>

<div align="right">Vice Provost and Dean of the Graduate School</div>

(Original signatures are on file with official student records.)

Hi-Fidelity Simulation of the Self-Assembly and Dynamics of Colloids and Polymeric Solutions with Long Range Interactions

A Dissertation Presented for the

Doctor of Philosophy

Degree

The University of Tennessee, Knoxville

Mahdy Malekzadeh Moghani

December 2014

Abstract

Modeling the equilibrium properties and dynamic response of the colloidal and polymeric solutions provides valuable insight into numerous biological and industrial processes and facilitates development of novel technologies. To this end, the center-piece of this research is to incorporate the long range electrostatic or hydrodynamic interactions via computationally efficient algorithms and to investigate the effect of these interactions on the self-assembly of colloidal particles and dynamic properties of polymeric solutions. Specifically, self-assembly of a new class of materials, namely bipolar Janus nano-particles, is investigated via molecular dynamic simulation in order to establish the relationship between individual particle characteristics, such as surface charge density, particle size, etc., and the final structure formation. Furthermore, the importance of incorporating the long range electrostatic interaction in achieving the corresponding final morphology is discussed.

The dynamic properties of polymeric solutions are investigated via two parallel pathways. In the first approach, force-extension behavior of the flexible polyelectrolytes is probed via fine-grained Brownian dynamics simulation of the bead-rod model. The presented model accurately incorporates the excluded volume interaction in order to capture the effect of salt concentration on the force-extension response of polyelectrolyte chain as observed in the single chain experiments. It is shown that accurate incorporation of the excluded volume effect on a long chain of more than 500 Kuhn segments is necessary to reach the universal scaling both for equilibrium properties and force-extension response. Next, a new force law is extracted using a

novel discrete Padè approximant from the constant-force ensemble result of the bead-rod model. The new force law is implemented in the coarse-grained meso-scale bead-spring model with hydrodynamic interactions in order to investigate the dynamics of flexible macromolecules in the athermal solvent.

In the second approach the computational cost of the long range hydrodynamic interaction in dilute solution of polymeric chains with constrains is reduced via development of a new computational technique based on the conjugate gradient and Krylov subspace methods. Moreover, an algorithm for estimating the contribution of various forces to the transient polymeric stress tensor is introduced and employed in order to investigate transient dynamics of the solution of the flexible polymeric chains.

Table of Contents

List of Tables

List of Figures

Chapter 1

INTRODUCTION

In the past three decades, innovative synthesis methods of colloidal particles and single chain manipulation techniques of macromolecules has emerged as effective means to respond to the growing demand for engineered micro-structures and materials in a variety of applications such as: drug delivery systems, high throughput screening, microfluidics, liquid optics, etc. Advancing these technologies and scaling up the lab protocols up to the industrial level, demands fundamental understanding of the equilibrium properties and dynamics of these complex systems.

While the nonlinear and multivariate nature of such complex liquids discourages pure theoretical approaches, fermented by the steady improvement of available computational power, simulations have gradually moved to the forefront of scientific advancement in the past few decades as the indispensable tool to elucidate the underlying physics necessary in development of the new technologies. Micro- and meso-scale modeling techniques are specifically distinguished due to the general applicability in nanotechnology and microfabrication where thorough understanding of equilibrium properties (such as self-assembly of colloidal systems) and dynamic properties (such as stress relaxation of polymeric chains) of the individual particle or chain are the key elements in the continuum level response of the system.

Two of the most prominent methods for modeling systems at these scales are the molecular dynamics method and the Brownian dynamics simulations. Evolution of the particle trajectories in both methods is based on the Newton's second law (inertial less in the latter) and therefore their accuracy depends directly on the accuracy of the estimation of the force exerted on each particle. Long range forces correspond to any distance dependent force law, $f(r)$, for which if r is the distance from the force action point then $F(r) = \int_r f(r)dV$ does not converge with increasing r for an admissible particle distribution. For a uniform distribution of particles, a spatial dependence equal or slower than $1/r^{d-1}$, where d corresponds to the system dimensionality, constitutes long range effects such as electrostatic or hydrodynamic interactions. Accurate and efficient incorporation of these effects and the investigation of their influence on the time evolution of the phase-space is the center piece of this research. As demonstrated in this work, long range interactions have a major effect on the collective motion of particles and significantly alters both self-assembly and dynamical properties of colloidal and polymeric systems.

Self-assembly is the spontaneous organization of system components (particles, polymeric segments, functional groups etc...) directed via specific interactions of the constituent and/or indirectly via the environmental parameters such as wall interactions or ion concentration (Grzelczak et al., 2010). Therefore the design of the interaction sites on building blocks is the key factor in achieving the desired pattern or functionality for applications such as nanosystem fabrications, microelectronics (Whitesides and Grzybowski, 2002), drug delivery systems, etc. Patchy particles with ionic electrostatic interactions are an excellent choice for directed self-assembly since their interaction range, strength and directionality can be regulated through environment characteristics, external electric fields and size and number of patches.

Innovative synthesis techniques have enabled fabrication of asymmetrically charged spherical particles called Janus particles in various sizes and shapes (see chapter 2). A host of visualization techniques ranging from SEM (Erhardt et al., 2003) to

epi-fluorescence microscopy (Hong et al., 2006) have been utilized to study the self-assembly of nano- to micrometer size spherical Janus particles. These developments plea for a detailed study that incorporates long range electrostatic effect on the structure formation of this class of material in order to establish the relationship between the characteristics and the self-assembly of the Janus particles.

The second part of this dissertation focuses on dynamical properties of polymeric systems consisting of flexible polymeric chains with long range hydrodynamic interactions (HI). This study intends to discover and/or capture distinct properties of flexible macromolecules compared to semi-flexible and rigid chains and connect these findings to experimental observations through Brownian Dynamics simulation.

The probability of transition between the gauche and the trans states and hence chain flexibility is mainly determined by the chemical structure of the backbone, such as side groups, existence of double bonds etc. In the Kuhn and Grün (1946) representation of a polymer chain where detail chemical structure is ignored in favor of set of connected uncorrelated statistical segments, flexibility translates into the size of the statistical segments per chain, and therefore when comparing two chains with similar contour length it translates into the number of Kuhn segments, i.e. more flexible chains consists of more Kuhn steps. For instance, at fixed contour length, double stranded DNA (dsDNA) with chemical bonds between the strands has less Kuhn steps compared to a flexible macromolecule such as single stranded DNA. Since most commercial polymers and numerous biomacromolecules fall under the flexible category, understanding the dynamics and force-extension behavior of this class of macromolecules has attracted significant interest in the last two decades.

A major breakthrough for such investigations is due to introduction of single macromolecule manipulation and microscopy techniques (Smith et al., 1992a; Perkins et al., 1997; Rief et al., 1997; Smith et al., 1999; Bustamante et al., 2000). Recently a series of novel experiments utilizing single molecule manipulation (Saleh et al., 2009; Brockman et al., 2011) have shown the distinctive behavior of flexible polymer chains with large contour length, which had not been addressed in previous experimental

or computational studies. Another important aspect of the single chain dynamics is the interaction with functional walls such as cell membranes or silicon substrates. Experimental measurement of diffusion in the vicinity of a functional substrate (Maier and Rdler, 1999; Sukhishvili et al., 2000) has shown that diffusion scaling exponent has a strong dependence on the substrate-polymer interactions. A clear picture of macromolecular flow in the vicinity of functional substrate, in confined geometries and finally in the semi-dilute regime, can also be rendered via a hi-fidelity hi-performance modeling technique developed in the course of this research. In fact, while the methods developed in this study are used to study the dilute regime of polymeric solutions, some developments such as application of multipole method are suited well for the semi-dilute regimes.

In this work a new computational approach is proposed in order to investigate the effect of long range electrostatic interactions and hydrodynamic interactions on colloidal systems and polymeric solutions, respectively. Specifically in the case of the colloidal system of Janus particles, a relationship between single nanoparticle properties and environmental variables with the structure formation can also describe the current experimental observations. In the case of the polymeric solutions, two approaches to a hi-fidelity model of polymeric system with hydrodynamic interactions and excluded volume is proposed. Firstly, upon construction of the new force-law for flexible polymer chains with the excluded volume, subsequent modeling of polymer chains with the hydrodynamic interactions is performed via the new force law in a coarse-grained representation. The second path revolves around establishing a novel method in Brownian Dynamics simulations of the bead-rod model of flexible chains with excluded volume and hydrodynamic interactions using the hybrid MPI/OpenMP programming concept.

In both of these systems, long range interaction effects are predominant and must be incorporated accurately and efficiently into any hi-fidelity modeling technique. To this end, this research is focused on addressing the following objectives:

- Establishing the relationship between the constituent characteristics and structure formation through molecular dynamics simulation that incorporates long range interaction effects in bipolar Janus particles.

- Efficient incorporation of hydrodynamic interaction effects on dynamical properties of flexible polymer chains. This objective is fulfilled via two parallel pathways; first by developing a new entropic/energetic force law from Brownian Dynamics simulation of the bead-rod model, and importing the new potential in the coarse-grained bead-spring model which enables efficient estimation of the hydrodynamic effects. An alternative approach pursues a similar objective via development of a novel algorithm for temporal evolution of the Langevin stochastic differential equation subject to constraints for the bead-rod Brownian Dynamics simulations.

Chapter 2

SELF ASSEMBLY OF SPHERICAL JANUS PARTICLES IN ELECTROLYTES

Experimental studies on nano- and micrometer sized Janus particles (JPs) have demonstrated a plethora of simple and complex self-assembled structures. In this study, molecular dynamic simulations that include long range Coulombic interaction have been utilized to elucidate the underlying physics of self-assembly of nano-scale spherical bipolar JPs as a function of surface charge density, salt concentration and particle size. Specifically, two distinct sub-structures at low JP concentration, namely, strings and rings, have been identified. As the concentration of JPs is increased these sub-structures join and/or hierarchically assemble into larger porous clusters. Moreover, it has been demonstrated that surface charge defects lead to precipitous loss of directional self-assembly. Finally, a direct connection between the ionic cloud around a single JP and the self-assembled structure morphology has been demonstrated. Overall, the results of this study should pave the way for future coordinated experimental/computational studies towards development of a mechanistic understanding of morphology development in this class of material.

2.1 Introduction

The introduction of molecular anisotropy on particles via innovative synthesis techniques has led to the development of a large class of self assembled micro- and nano-scale morphologies with long range order, specific interaction with polar solvents, desired charge distribution and reactivity. To this end, this class of material has found widespread use in many fields of science and engineering, including drug delivery, waste water treatment, oil recovery, emulsion stabilization, liquid optics and optical probes (Torchilin, 2001; Bucaro et al., 2008; Kim et al., 2008; Jiang et al., 2008).

Although, different JP building blocks such as cylindrical or pallet shapes have been introduced, the most commonly studied JPs are spheres with two distinct hemispheres. Specifically, a host of visualization techniques ranging from SEM (Erhardt et al., 2003) to epi-fluorescence microscopy (Hong et al., 2006) have been utilized to study the self-assembly of nano- to micrometer sized spherical Janus particles. For bipolar JP, in which two hemispheres have functional groups carrying opposite charges, these studies have demonstrated that chains and porous structures consisting of rings and chains are the predominant self-assembled structures for micro- and nanometer size bipolar particles, respectively (Suzuki et al., 2007; Jiang et al., 2008; Xu et al., 2010). On the other hand, for micron sized amphiphilic particles, aggregates and spiral structures are observed (Chen et al., 2011), while for nanometre sized particles porous structures have been detected (Xu et al., 2010).

Although experimental studies of structure formation as a function of particle size, concentration and polarity in JPs have provided insight into the self-assembly of this class of patchy particles, they do not provide the much needed connection between individual particle properties and the resulting self assembled structures. Clearly, development of rational design and optimization strategies to guide specific self-assembled micro- and nano-structure formation, based on individual particle

properties is a critical step in translating bench-top synthesis protocols to large-scale fabrication techniques. To this end, modeling and simulation tools, namely, coarse grained Monte Carlo (MC) and molecular dynamic (MD), have been used to develop phase diagrams for self-assembled JPs as a function of volume fraction and effective surface charge. Specifically, MC simulations with the particle modeled as a dipole inside a hard/soft sphere or with square well attractions between two hemispheres have been performed to ascertain the influence of particle volume fraction and effective surface charge on the morphology of the self-assembled structures. Specifically, it has been shown that when the attraction potential range is on the order of the particle diameter, strings and mixture of strings and body-cantered-tetragonal phase are observed for dipolar soft particles (Hynninen and Dijkstra, 2005) at low to intermediate (≈ 0.3) particle densities. On the other hand, spherical micellar clusters of amphiphilic JPs grow into larger spherical aggregates (vesicles) as the packing fraction increases (Sciortino et al., 2009). Furthermore, Miller and Cacciuto (Miller and Cacciuto, 2009), based on extensive MD simulations with varying surface-surface interaction modeled via modification of the onset angle of a smooth step potential, have suggested that subtle changes in patchiness of the individual large (relative to the interaction range) particles can lead to development of a host of morphologies, including micellar-aggregates, hexagonal bi-layers, and clusters with face-centerd cubic (FCC) order.

To date, MC and MD simulations of structure formation in spherical JPs have been based primarily on coarse-grained particle and inter particle interaction models. Specifically, particle-particle interactions have been modeled with simple angle dependent potentials between the unit normal vectors of particle hemispheres. Moreover, long range Coulombic interactions have not been taken into consideration. Although, Hong et al. (2006) have observed that aggregate formation in micron sized bipolar JPs is insensitive to the precise range and shape of potential as long as this range is about one third of the particle diameter, long range Coulombic interactions can prevent symmetrical solvation of surface charges with ions in the system. This

is even more important for nanometer sized bipolar JPs where the effective range of Coulombic interaction is on the order of the particle diameter. To this end, MD simulations with realistic representation of the JPs charge distribution and explicit treatment of long range interactions can play a central role in establishing the critical link between the individual particle properties and the resulting structures under different environmental conditions. Hence, we have performed detailed molecular dynamic simulation of the self-assembly of spherical nanometer sized JPs inclusive of long range Coulombic interactions with evenly distributed opposite charged hemispheres in electrolytes. In turn, the simulation results have been utilized to elucidate the underlying physics of self assembly of nano-scale bipolar JPs as a function of surface charge density, salt concentration, particle size, and surface charge defect density.

2.2 Simulation method

In order to realize the aforementioned objectives, MD simulations with a detailed particle model have been carried out. Specifically, the total interaction of a JP is considered to be the sum of interactions between charges distributed uniformly on a fixed radius from the center, screened by the presence of free conjugate ions in the solvent. This representation explicitly includes the orientational dependence of particle-particle interaction and multi-pole effects.

Charges are represented by the restrictive primitive method for free ions in the solution and JP surface charges. Solvent molecules are modeled as coarse grained neutral hard sphere and the electrostatic effect of the solvent is implicitly present through its dielectric constant. The aforementioned solvent model neglects hydrogen bonding. In this work, it is assumed that hydrogen bonding has a negligible effect on cluster formation, compared to the electrostatic interactions. The validity of this assumption and the exact effect of hydrogen bonding on cluster formation of Janus nano-particles with surface charges requires further investigation.

A uniform charge distribution on the JP surface is guaranteed by using a specialized spherical code (see Hardin et al., 2008) that enforces uniform cap distribution over a spherical surface, i.e., the distance between each charge and its immediate neighbors is equal for all charges. In total, 60 interaction sites were considered on the surface of the nano-particles. Different surface charge densities are realized by changing the number of elementary charges at each interaction site. All interaction sites are bonded with a very stiff harmonic spring to the center of the particle (See Fig.2.1). A secondary hard shell covers all surface charges to create the desired excluded volume effect. The total radius of the particle (restrictive shell) is the sum of bond length and radius of charges. Excluded volume effect for both JPs and electrolyte ions is incorporated via the Weeks-Chandler-Anderson (WCA) potential, which is a shifted Lennard-Jones (LJ) potential so that its minimum is zero at the cut off radius. Interaction sites are divided into two hemispheres, and sites in one hemisphere are charged positively while those on the other hemisphere carry negative charges. Electrostatic interaction up to a JP diameter from each charge is calculated in real space, for charges beyond this distance the particle-mesh method is used.

The self-assembly process was investigated via MD simulations with LAMMPS in an NVT ensemble at T=300K using the Nóse-Hoover thermostat. The solvent relative dielectric constant is set to that of pure water at 300K. Positive and negative free ions (electrolytes) are modeled as mono-valent charges with radius of 1.02 .

A variety of environmental conditions and JP characteristics were studied to ascertain their influence on morphology development. Specifically, JP diameter, a, ranging from 5.5 to 7.5 nm with surface charge densities, σ, of 0.5 to 2 e/nm^2 in absence of additional salt (hence maximizing electrostatic interaction range) and also in electrolyte concentrations, C_s, of 1 and 3 mM have been studied.

Elucidating the pathway of assembly necessitates a quantitative approach for clusters characterization, especially as the clusters become more populated. Borrowing basic concepts of weighted adjacency matrix and connectivity list from graph theory,

an in-house code was developed for cluster characterization. Specifically, the weighted adjacency is constructed following a simple strategy, namely, the ijth element is zero whenever two particles are not neighbors. If they are neighbors, the element value is equal to the cosine of the angle between connector vector of two connected JPs and the vector that connects the center of JP to the center of charge of positive hemisphere. Upon formation of the weighted adjacency matrix for each cluster, sub-clusters are identified based on this weighted adjacency matrix to resolve the building blocks of that specific cluster. Finally, each sub-cluster is quantitatively characterized based on various geometrical measures, including an angle between connector vectors, dihedrals, etc.

2.3   Results and discussion

As mentioned above, our interest lies in developing rational strategies to guide specific self-assembled micro- and nano-structure formation, based on individual particle
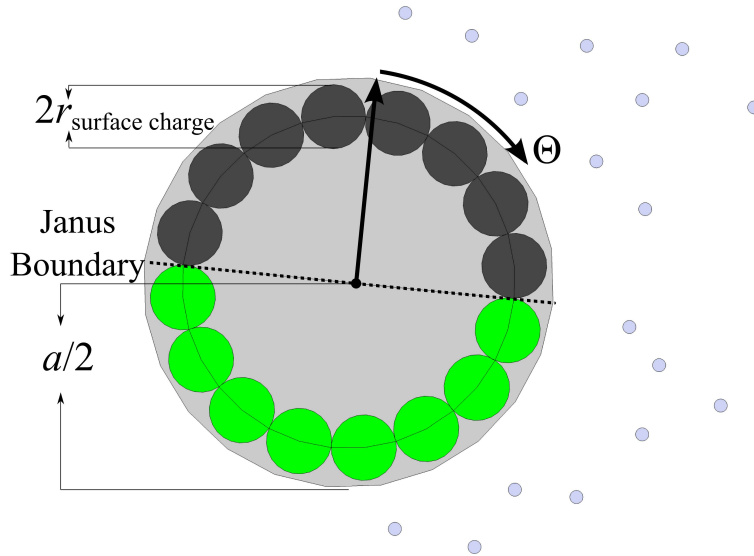
Figure 2.1: Schematic of a single Janus particle. Center of each surface charge is connected with a stiff spring to the center of the particle. Charges are placed at the center of each interaction site shown as black (positive) and green (negative) spheres. Θ-direction and Janus boundary are also defined in the schematic.

properties. To achieve this objective, the hierarchy of the self-assembly process is examined. In this approach JPs assemblies are literally followed as the system concentration is increased until the observed incipient structures can successfully predict the next level assemblies. To this end, the best starting point for the analysis is that of single JP and the electrolyte. As it will be shortly demonstrated with this simple hierarchical approach, development of complicated and more populated structures at higher concentrations can be rationalized. Subsequently, the system without salt is considered.

Investigating the unperturbed electrolyte spatial distribution around a single JP reveals two important facts about bipolar JPs. As shown in Fig.2.2, the angular dependence (Θ-direction) of free ion radial pair distribution around an isolated JP demonstrates that the Debye electrostatic screening length (κ^{-1}) of the counter ion reduces rapidly as one moves from poles to the equator of the particle. To this end, surface charges near the equator experience almost no significant net attraction/repulsion; hence, they are not likely sites for cluster growth (see Fig.2.2-inset). A detailed examination of charge concentration contour plots (Fig.2.3) around each hemisphere revealed two nonzero extrema along the Θ-direction. Since exterma occur at locations with highest electrostatic attraction (repulsion) for each counter ion, they will correspond to locations with highest probability for further addition of JPs. The primary addition site is marked by the maximum concentration of counterion. The minimum of counterion concentration (at around 55-60 degree in Fig.2.3-right) represents the secondary interaction site. As it will be shown later, this weaker interaction site comes into play when small incipient assemblies are formed. Formation of this secondary interaction site is a direct consequence of the double layer formation around the cap region (dark borders in Fig.2.3-right) and high concentration of counter ions at$\Theta > \pi/2$.

Formation of the incipient structures indeed adheres to the aforementioned scenario. With 7-8 particles in 1203 nm^3 periodic boxes two major assemblies were found: rings and strings (Fig. 2.4-e and f). Specifically, particles tend to form chains

12

at higher electrolyte concentrations. Also, for larger particles (7.5 nm vs. 5.5 nm) the chain structure is the preferred structure provided all other parameters of the system are fixed. Transition from ring (e) to chain (f) is observed for a=5.5 nm for σ=1.26 and 1.58 (e/nm^2) as electrolyte concentration increases from 0 to 1 mM. Both of these observations suggest that when $\kappa a \approx O(1)$, i.e. long range electrostatic interactions between particles is effectively screened, the cluster grows by addition of particles on the polar interaction site ultimately, leading to string formation. This observation is consistent with observation of string (Suzuki et al., 2007; Jiang et al., 2008), in micron size JPs where $\kappa a > 1$. On the other hand, when long range interactions are not screened (lower salt concentration or very high surface charge density), ring structures are observed.
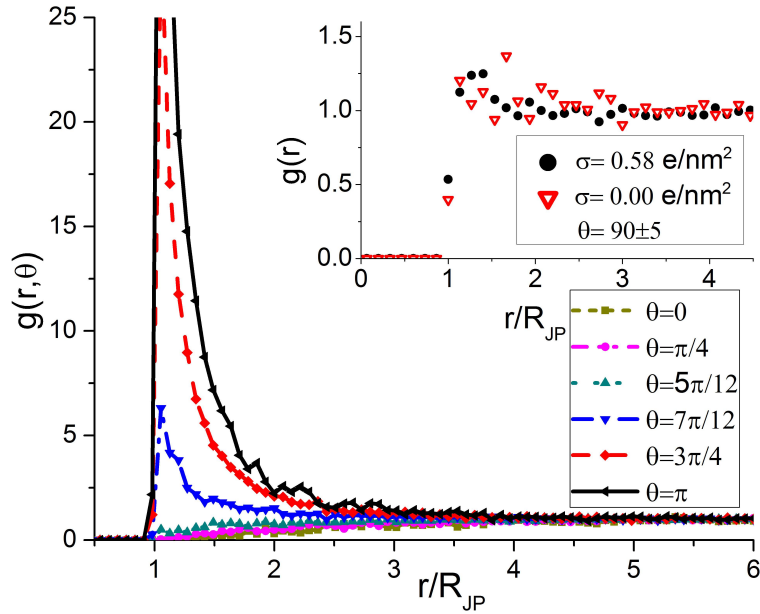
Figure 2.2: Angular dependence of radial pair distribution function of the positive free ions shows the dependence of the Debye screening length on the Θ-direction for $a = 7.5$ nm, $\sigma = 1.1$ e/nm^2, $r_{sur.ch} = 1.2$ nm. Inset compares the similarity of ion distribution at the region around the Janus boundary with the distribution around hard sphere with no surface charge. Θ-direction is divided into equal slices with θ in the legend pinning the initial coordinate of the slice in Θ-direction.

As the number of JPs in the system increases, there are two pathways to larger structures: one is longer string and the other is assembly of strings alongside each other. In the first case, strings will assume a chiral shape and in the later case they form a curvilinear chain assembly with three or more strands (Fig. 2.4-(c) and (d) respectively). A similar scenario is followed in ring structures. That is, they either form larger rings (more particles per closed circle) or rings assemble on top of each other (Fig. 2.4-(a) and (b) panels) to form a porous structure. Figure 2.5 depicts a connection map between JPs centers when chains or rings are assembled alongside each other (second pathway); the triangular elements formed in these clusters show the hexagonal packing of the particles.

Further insight into the cluster growth mechanism can be obtained via geometrical measures. If particle i is followed by particle j and k in the cluster, then the supplementary angle that two subsequent connector vectors ($\overrightarrow{ij}$ and $\overrightarrow{jk}$) make with each other is called the connector vector angle (ψ). For each particle, $\vec{p}$ is defined
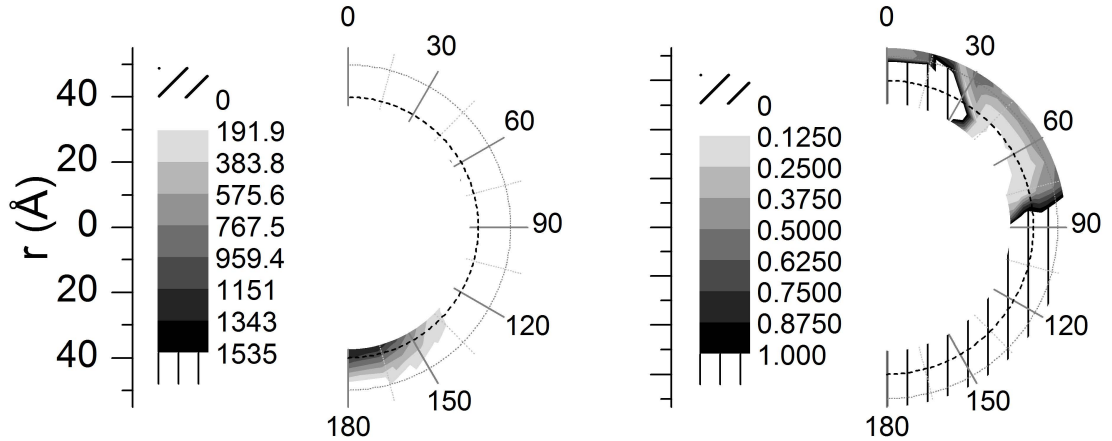
Figure 2.3: Charge distribution of the free ions around a single JP. Both panels show distribution of positive ions, with negative cap at $\Theta > 90$ degree. Legend bands are optimized to enhance visualization of maxima and local minima (in left and right panels respectively) for $a = 7.5$ nm, $\sigma = 2.2$ e/nm^2, $r_{sur.ch} = 1.2$ nm, $C_s = 1$ mM. Darker areas correspond to higher positive ion local concentration. Y-axis is distance from the center of JP and the curvilinear axis is the Θ-direction with Janus boundary at 90 degree.

as the vector that connects the center of the particle to the center of charge of the positive hemisphere. The angle between the $\vec{p}$ and the $\overrightarrow{ij}$ vector is denoted as ϕ (Fig. 2.6-right).

The ensemble averaged (over time and clusters) probability distribution function of the connector vector angle, $\langle\psi\rangle$, is depicted in Fig. 2.6. For ring formation $\langle\psi\rangle \approx 2\pi/n$, where n is the number of JPs per ring. Significant deviations of the $\langle\psi\rangle$ from zero clearly demonstrates that the chain like structure has a curved contour.

Figure 2.7 shows values of $\langle\psi\rangle$ and $\langle\phi\rangle$ for different surface charge densities and salt concentrations. Higher values indicate enhanced curvature of the cluster contour.
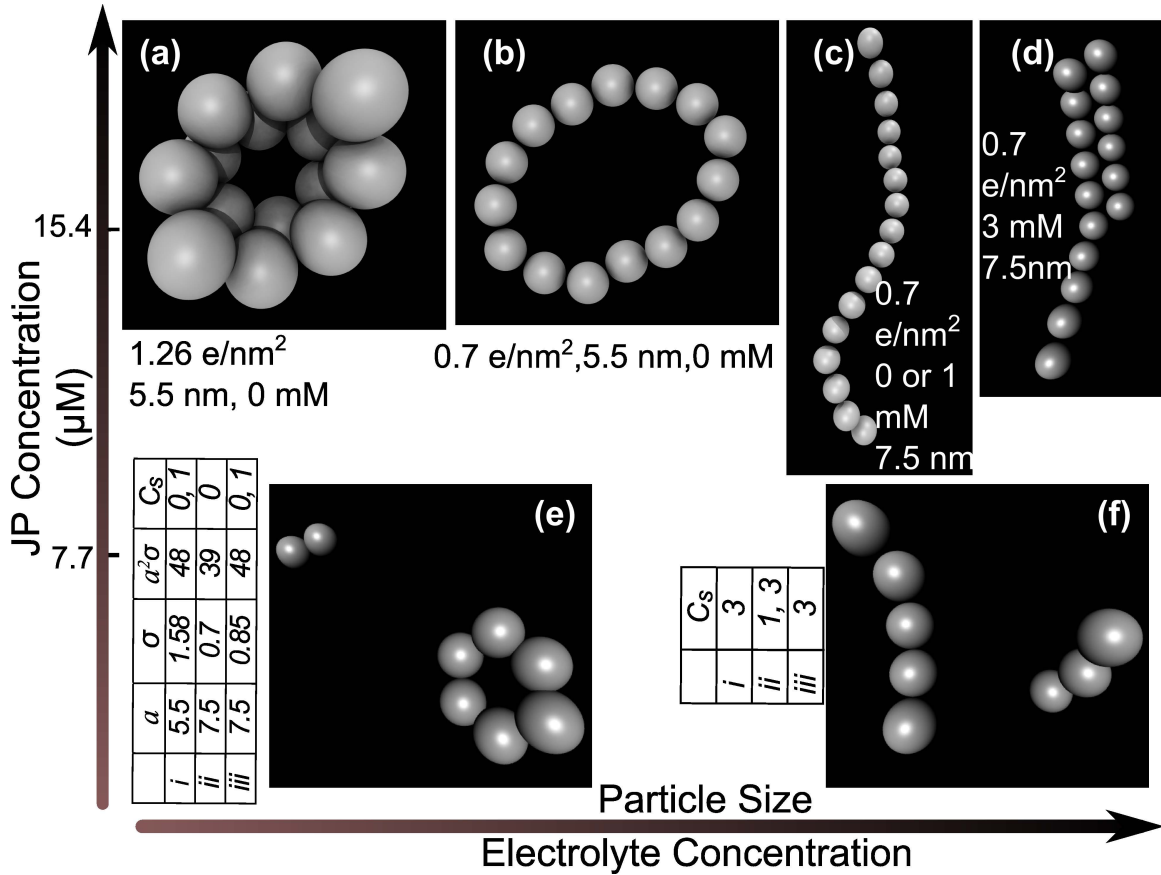
Figure 2.4: Cluster growth regimes at very low concentration region (no cluster-cluster interaction). Similar transition from single chain (c) to chains assembled alongside each other (d) occurs for 5.5 nm particles at fixed σ for increasing C_s from 1 to 3 mM. Transition from (e) to (f) is observed only when $\kappa a < 1$.

15

As surface charge density increases up to a critical value, both $\langle\psi\rangle$ and $\langle\phi\rangle$ drop nonlinearly toward zero. At higher σ a plateau is reached. However further increase of surface charge density will result in ring formation.

Ring formation is due to the competition between two different mechanisms, both acting to minimize the structure Gibbs energy: $G = U - TS$. On one hand, ring formation will decrease entropy of the system, S, since it decreases degrees of freedom
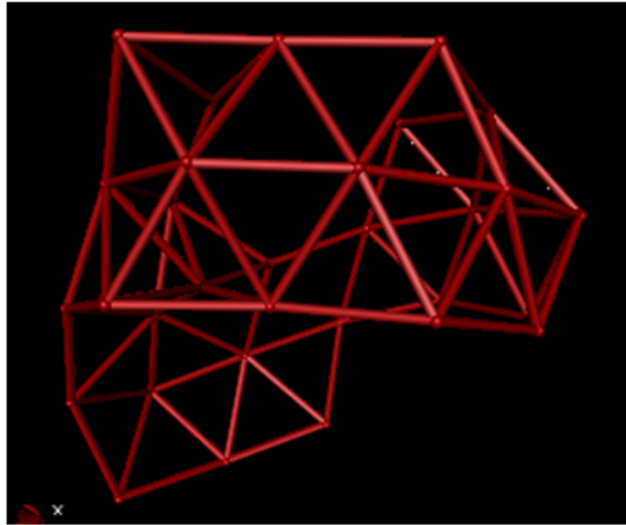
Figure 2.5: Connection pattern obtained by connecting the neighboring particles for assembly of three rings on top of each other; the final cluster is porous and particles have hexagonal packing on the surface.
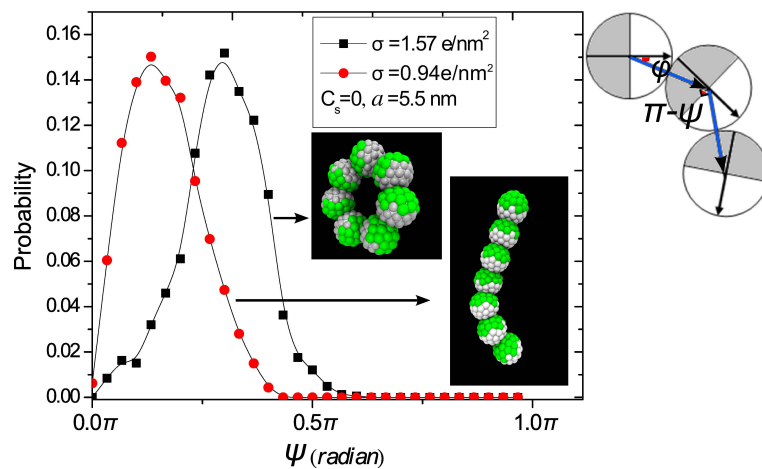
Figure 2.6: Probability Distribution functions of ψ for two different surface charge densities. On the right sketch ψ and ϕ definitions are shown.

16

of the cluster by formation of an additional bond. Additionally, transition from a chain into a ring isomer requires extra tilting of the chain contour, which acts as a barrier in the energy landscape. If the chain like structure at equilibrium has an average angle of $\langle \psi_{ch} \rangle$, then the equivalent ring consisting of n JPs will cause an over bending of $\Delta \psi_t \approx 2\pi/n - \langle \psi_{ch} \rangle$. On the other hand, the total potential energy, U, of the system will drop if two additional hemispheres of opposite charges participate in the formation of an additional contact area (bond) and form a ring.

As σ increases, $\Delta \psi_t$ reaches a plateau and the drop in electrostatic potential due to the formation of the new bond ($\Delta U_{bond} \tilde{\sigma}^2$) will ultimately compensate for the competing mechanism, namely bending penalty, therefore a ring can be formed. At lower surface charge densities, although the deviation from $\langle \psi_{ch} \rangle$ to form a ring is small, the drop in potential energy cannot compensate for the lower entropy. Since $\Delta \psi_t$ also decreases with n, it is expected that clusters with more JPs can transform from chain to rings at lower σ. In fact, this was observed in simulations where the number of JPs in system was increased from 7 to 14 (while keeping other characteristics constant).

The importance of studying assembly of a limited number of particles lies in the fact that larger assemblies at higher volume fractions are the result of hierarchical co-assembly of these smaller building blocks. This effect is shown in Fig. 2.8-a, where three spiral shape strings have come together to form a curvilinear structure before the structure bifurcate into smaller branches. In these larger systems, coexistence of rings and strings leads to formation of an ordered porous structure (Fig. 2.8) consistent with experimental observations for nano-meter sized JPs (Xu et al., 2010).

Synthesis methods based on masking, particle at interfaces (Lattuada and Hatton, 2011) or cap deposition (Ren et al., 2012) are prone to defects such as anomalous Janus boundary (Park et al., 2011), which can only become more severe at nano-scale since the relative magnitude of thermal perturbations are large compared to particle size. To investigate how such defects can influence self-assembly from the aforementioned path for JPs devoid of charge defects, the effect of surface charge defect is investigated

by random translation of the surface charges to the counter hemisphere. Effect of random translation is characterized by a decrease in normalized magnitude of polar vector ($\vec{p}$): for a perfect JP this value is equal to 1 and for a completely random arrangement of positive and negative surface charges it will become zero. As shown in Fig. 2.10, upon introduction of about 20 and 27% defects (corresponding to normalized polar vector of 0.7 and 0.6 respectively), particles aggregates in a visibly less ordered structure, namely aspect ratio of aggregates approaches one and directionality of the assemblies is reduced. Also, at a fixed concentration the average number of JPs per cluster decreases. This behavior also manifests itself at higher volume fractions resulting in formation of spherical aggregates as depicted in Fig. 2.9. These findings underline the role of uniformity of surface charge distribution in the self-assembly process. Specifically, loss of directed assembly in presence of defects is observed. Although aggregation pathways and exact configuration of the structures depend on the precise location of the defects, repeating the above procedure with different seeds, particle size (7.5 nm vs. 5.5 nm) and electrolyte concentration (0
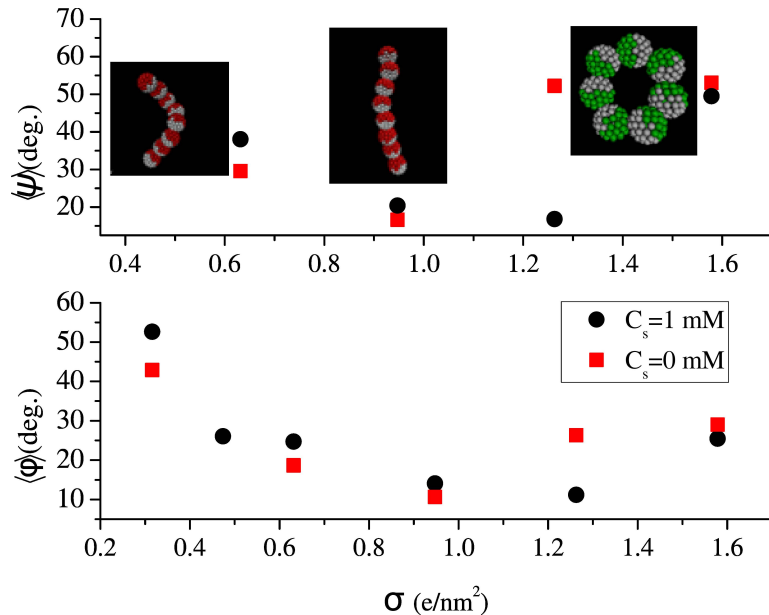
Figure 2.7: 7 Ensemble averaged equilibrium connector vector angles, $\langle\psi\rangle$ and $\langle\phi\rangle$, decrease with increasing surface charge density until a transition point after which rings are formed, $a = 5.5$ nm.

or 3 mM vs. 1 mM) confirms the aforementioned conclusion. Finally, in order to underline the significance of long range interaction in development of long chains and ring type structures, a series of simulations at 0 and 1 mM electrolyte concentration at various surface charge densities for 5.5 nm JPs were performed where the electrostatic interaction was cut off at $2a$, a and , $a/2$, i.e. range of electrostatic interaction between pair of charges is explicitly bounded by the above cut off values. For $C_s = 1$ mM where $\kappa^{-1} \approx 10$ nm, the system with a cutoff radius of $2a \approx 11$ nm produced similar structures as that of the control runs (full long range Coulombic interaction), while those with shorter interactions gave rise to very short chains and triangular trimers (see Table 2 second row). As expected, long range interactions become more important when screening is insignificant, $\kappa^{-1} > 2a$. As depicted in the first row of Fig. 2.11, when the interaction range is reduced to the order of particle radius, triangular trimers and tetrahedrons are formed, as opposed to double rings in the control run.

2.4 Conclusions

Structure formation in bipolar JPs and its correlation with single JP characteristics was studied via MD simulation with a realistic representation of the (bipolar) JP charge distribution and explicit treatment of long range interactions. It is shown that a plethora of self-assembled structures, namely rings, chains and aggregates can be achieved by judicious manipulation of κa and the surface charge density. Furthermore, a simple mechanism based on the thermodynamic driving forces for the assembly of the incipient chain and ring structures has been proposed and validated. The importance of electrostatic interactions in JPs self-assembly has been underscored by manipulating the interaction range. Specifically, when the electrostatic interactions are bounded below the particle diameter, string formation commensurate with experimental structures of micron size JPs is observed. It has also been demonstrated that at the higher JP concentration, rings and strings will

19

enact as building blocks by either joining into the same structure but with larger population of JPs or by hierarchical co-assembly into larger porous structures or spiral chains. Furthermore, the current model for JP provides a unique opportunity to investigate effect of defects on structure formation. To this end, presence of random defects has been shown to lead to the loss of directional growth of incipient structures and formation of aggregates. Overall, this study provides a qualitative relationship between characteristics of the individual particle and the final morphology of bipolar JPs, which in turn facilitates a bottom up approach towards directed self assembly of Janus nano-particles.
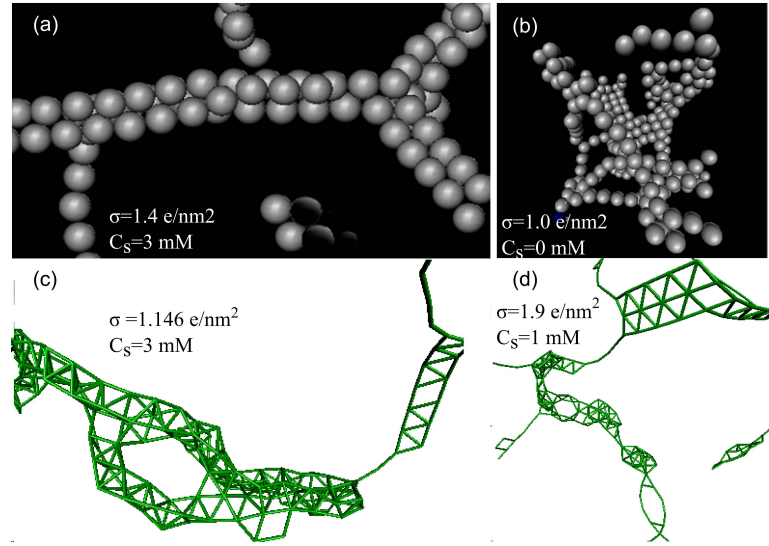
Figure 2.8: Formation of porous structures and elongated chain assemblies at higher concentrations (volume fraction is 0.1 for (b) and 0.01 for all other snapshots). $a = 6.2$ nm, $r_{sur.ch.} = 0.6$ nm for (b) and $a = 5.5$ nm, $r_{sur.ch} = 2.5\text{Å}$ for (a), (c) and (d).
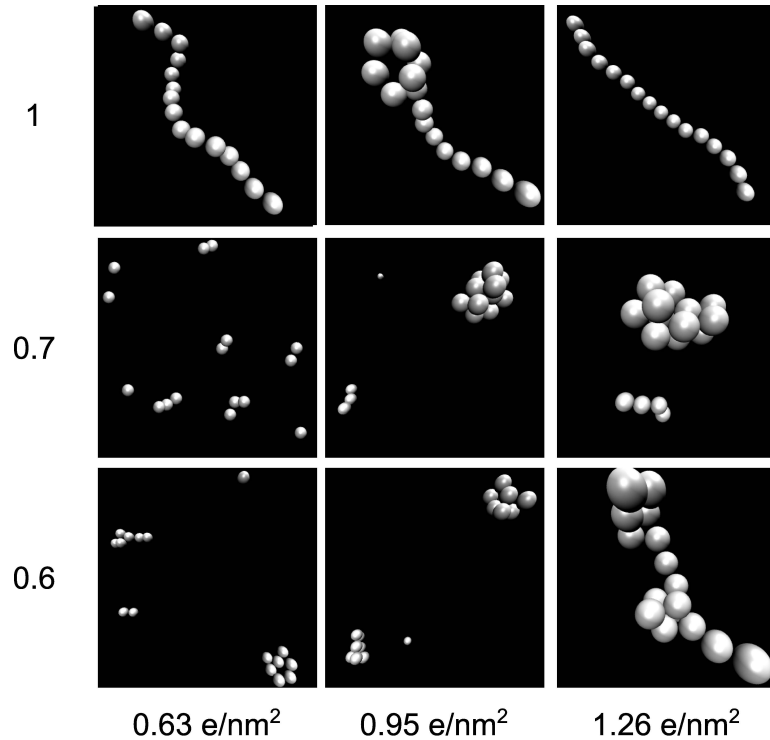
Figure 2.9: Effect of defects on assembly (aggregation) of JPs. $\sigma = 0.63$ e/nm^2, normalized $|\vec{p}|$=0.7 (20% random defect),1% volume fraction, $C_s = 1$ mM
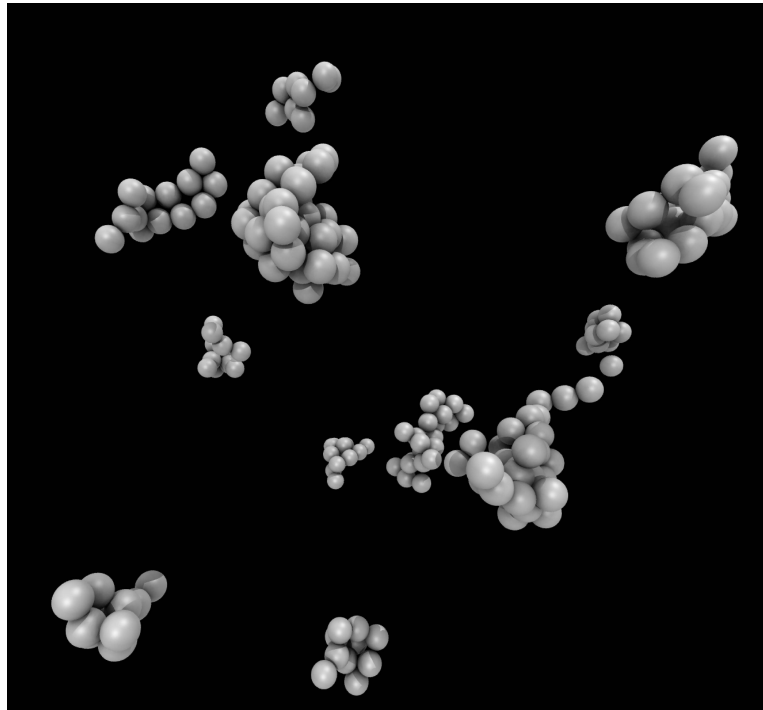
Figure 2.10: Loss of directionality upon introduction of random defects on structure formation for $a = 5.5$ nm and $C_s = 1$ mM. Values in the last row are surface charge density (e/nm²) and values in the first column are normalized magnitudes of polar vector.
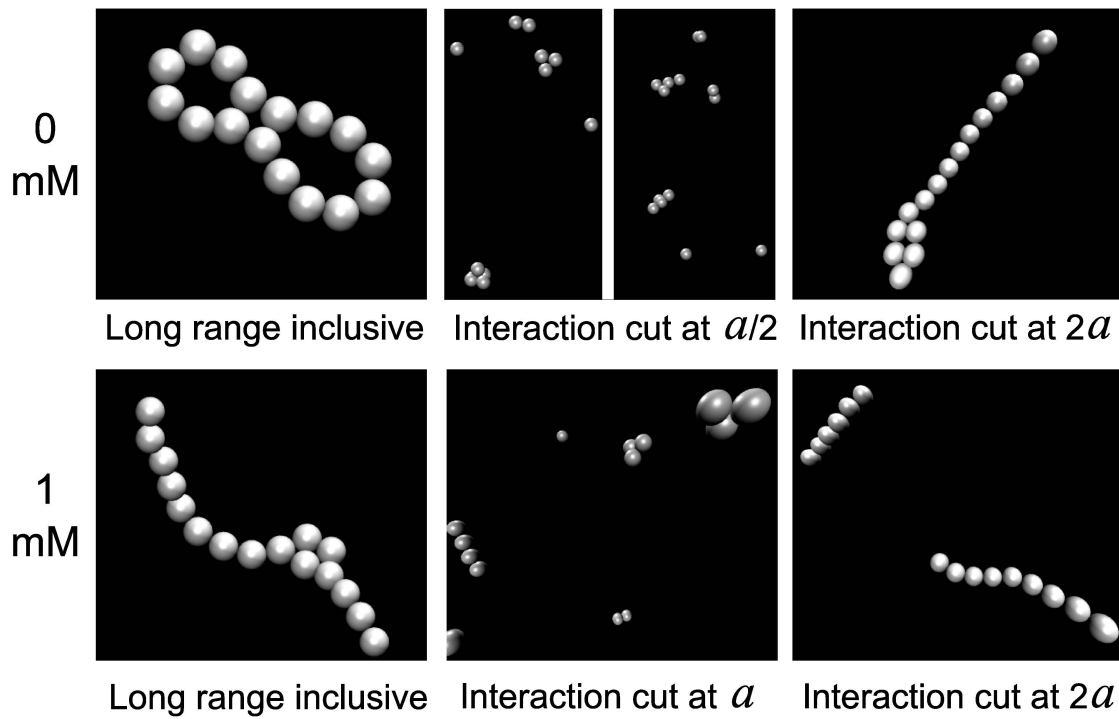
Figure 2.11: Importance of long range interaction on structure formation of bipolar JPs is shown through each row at different electrolyte concentration of 0 and 1 mM (shown on the left of the corresponding system).

Chapter 3

MESOSCOPIC SIMULATION OF DILUTE SOLUTIONS OF FLEXIBLE POLYELECTROLYTE CHAINS: EQUILIBRIUM PROPERTIES AND FORCE-EXTENSION BEHAVIOR

Macromolecules with ionizable groups are ubiquitous in biological and synthetic systems. Due to complex interaction between chain and electrostatic decorrelation lengths, both equilibrium properties and micro-mechanical response of polyelectrolyte (PE) dilute solutions are more complex than the neutral macromolecular dilute solutions. In this work, upon construction of conceptual diagrams of the relevant non-dimensional units, hi-fidelity Brownian Dynamics (BD) simulation utilizing the

bead-rod description of polyelectrolyte dilute solutions is performed in order to explore universal equilibrium behavior, scaling of the Kuhn step length (l_{ES}) with salt concentration c_s and the force-extension behavior of the PEs. Our results indicate that for a chain with n Kuhn segments $l_{ES} \sim c_s^{-0.5}$ as linear charge density approaches $1/n$, in agreement with the previous theoretical predictions. Moreover, the constant force ensemble modeling results accurately predict the initial non-linear region of PEs recently examined via single chain experiments. Finally, inspired by Cohan's extraction of Warner's force law from the Inverse Langevin force law, a new numerical scheme is developed in order to extract a new elastic force law for real chains from the discrete set of force-extension data similar to Padè expansion, which incorporates the initial non-linear region.

3.1 Introduction

Hi-Fidelity prediction of equilibrium and non-equilibrium responses of biological and synthetic macromolecules are essential in a wide array of biological processes as well as many emerging technologies, including DNA mechanics, cell locomotion and molecular motors (Bao and Suresh, 2003). To this end, acquiring insight into the complex micro-mechanical deformation of macromolecular systems has motivated single chain studies. These include experimental techniques such as single molecule force spectroscopy and complimentary meso- or nano-scale simulation. Beyond equilibrium properties, an indispensable step towards interpreting experimental results or making sound material property predictions requires an accurate force-extension (F-X) relationship, which predicts the deviation of the free energy due to the change in the conformation of the chain and vice e versa. If the macromolecule backbone consists of intermittent ionizable groups (polyelectrolyte), the interplay of repulsive electrostatic potential and entropy alters both the equilibrium properties and F-X relationships, depending on the salt concentration and solvent properties.

Properties of PE at equilibrium have been extensively explored theoretically in two distinct regions. First, when screening of the electrostatic interaction is negligible, mean field and scaling theories with non-uniform chain extension predict that the root mean squared end-to-end distance, r_e, scales with the number of bonds along with a logarithmic correction due to aspherical conformation, i.e. $r_e \sim n(1/l_q)^{2/3}[\ln(\alpha n)]^{1/3}$ (Katchalsky et al., 1950, 1953; Dobrynin, 2005). Here l_q is the distance between charged units in terms of the number of bounds along the chain contour and α is a function of l_q and bond length. In the second region, which has significantly higher practical implications, screening of the ionized groups of the polymer backbone due to free solvated ions reduces the electrostatic decorrelation length (κ^{-1}) when compared to the non-ionized bond decorrelation length of the macromolecule i.e., the polymer intrinsic Kuhn length (l_o). The screened electrostatic interaction at this limit perturbs the random Gaussian distribution and increases the decorrelation length of the polymeric chain to l_k. The exact scaling of this additional correlation, $l_E = l_k - l_o$, with κ^{-1} has been debated in literature: The theory pioneered by Odjik-Skolnick and Fixman (Skolnick and Fixman, 1977) estimated $l_E \sim \kappa^{-2}/A^2$ for long worm-like chains while Barrat and Joanny and Muthukumar (Muthukumar, 1987; Barrat and Joanny, 1993; Muthukumar, 1987; Everaers et al., 2002) estimated the scaling as $l_E \sim \kappa^{-1}$. Meanwhile, experimental observations in the second region have confirmed both scaling laws and have even provided an interim scaling exponent (≈ -1.6) (Chen et al., 2012). Nevertheless, the common underlying assumption in both methods is the fact that the electrostatic interaction at this limit can be approximated with a repulsive excluded volume interaction.

The schematic Fig. 3.1 depicts the six possible regimes of PE for the semi-flexible and the flexible polymeric chains in terms of the two nondimensional ratios: $A = l_q/l_o$ which is the relative distance of two ionized groups along the backbone to the intrinsic Kuhn step and $B = \kappa^{-1}/l_o$, which quantifies the ratio of the charge decorrelation to the chain decorrelation length. Parameter A represents the fraction of charged units and their relative distance along the contour, positioned at the center of the beads.

Parameter B relates the salt concentration to the excluded volume radius through κ^{-1} and ionic strength, i.e. $\kappa \sim c_s{}^{0.5}$ where c_s is the salt concentration. For small charge fractions (the upper limit of the diagram), fluctuation of r_e due to thermal energy is equal to that caused by the electrostatic energy of the chain, which can be described in terms of the electrostatic blob and the thermal blob concept (Dobrynin and Rubinstein, 2005); hence the electrostatic effects are minor at best. At high linear charge density along the backbone (the lower boundary of horizontal axis) the Manning condensation limit is reached, i.e., the Bjerrum length (l_B) is equal to the charge distance. Region (I) is mainly encountered for semi-flexible chains where charges along the backbone will practically increase the chain thickness along the contour.Due to strong repulsive force at distances less than the polymer Kuhn length (l_o), in region (II) the repulsive forces of the electrostatic interaction will first stretch the chain locally at the level of Kuhn length until it reaches region (I) with a new bare Kuhn length (l_o'), reducing the problem back to region (I). Region (III), which shows highly ionized chains with negligible screening along with region (VI) where $1 < A < B$ and incorporates mean field Flory type approaches, are not of interest of this research since the conclusive theoretical work on these regions already exists and these systems are rarely encountered in practice. In regions (IV) and (V) , $B < A$, l_E is added to intrinsic persistence length of the neutral polymer, which is the focus of this research.

As previously mentioned, not all of these six regions are commonly encountered in practice. For example, typical value of dsDNA Kuhn length is about 120nm and comparing this length to the screening length in the presence of 1 mM monovalent salt , $\kappa^{-1}_{C_s=1mM} = 9.6$ nm indicates ($B < 1$). Hence, for most flexible chains the right side of regions (I) and (IV), shaded as gray in Fig. 3.1a, is not accessible. For a semi-flexible chain such as ds-DNA, salt concentration below 1e-5mM is required for region (III), (V) and (VI) to be accessible. Similarly for ssDNA, a typical flexible chain with the Kuhn length of order 1 nm, and considering the Bjerrum length of water at room temperature (≈ 0.7 nm), the regions below the dashed line in Fig. 3.1b,
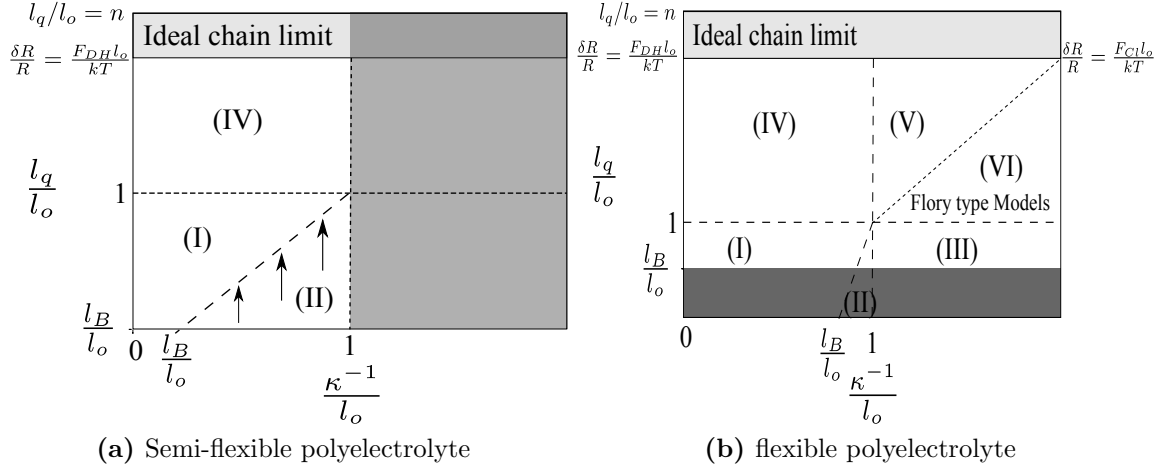
Figure 3.1: Different regimes separated based on the relative scaling of the characteristic length scales of the PE dilute solution. Based on the practical magnitude of the model rigid or flexible macromolecules, regions that are not accessible by the respective chain is shaded gray.

i.e. regions (I)-(III), are not of prime importance as compared to regions (IV, V). Therefore the focus of this research is mainly on the properties of PE in these two regions, i.e. (IV) and (V). In this study, not only the scaling of the equilibrium properties as a function of A and B is thoroughly investigated, but also the F-X response of single macromolecules and the dependance of the initial non-linear region on the salt concentration (B) and distance between charged groups (A) is studied. In turn, a new force law for the special case of $A = B = 1$ is developed, which incorporates the initial non-linear regime of the elastic response in the region where the nondimensional force is small, specifically $fl/kT < 1$.

The F-X response of flexible PEs has been recently investigated via single chain experiments (Dessinges et al., 2002; Saleh et al., 2009) with observation of a distinct nonlinear region at small extensions, which is in contrast to ideal chains. For neutral ideal polymeric chains, two classical force laws, one based on a freely jointed chain (FJC, flexible) and the other based on the worm-like chain (WLC, semi-flexible) model have been developed. FJC consists of two limiting F-X behavior: at low extensions, the elastic force results in the linear behavior (Hookian spring with

stiffness of $3kT/n$ where kT is the thermal energy and n is the number of Kuhn steps), while at high extension the limited extensibility of polymer chain causes the force to become tangential to the $1/(1-x)$ curve where x is the measure of extension. The WLC force law models semi-flexible polymeric chains such as ds-DNA with a continuous contour and an inherent stiffness. Similar to the FJC, F-X curve for the WLC also commences with a linear region; however at medium extensions, it predicts a stiffer chain and as the chain end-to-end distance approaches its contour length $(x \to 1)$, the retracting force approaches the $1/(1-x)^{0.5}$ curve. For flexible PEs at low salt concentration, a nonlinear region where $x \sim f^{\gamma=2/3}$ has been observed in line with the scaling prediction of Pincus for self-avoiding random walk chains (SAW) for $fl_o/kT < 1$. It has also been shown that the PE F-X gradually resumes to the linear behavior, $\gamma \to 1$, as the salt concentration increases. Moreover, at higher forces Saleh et al. (2009) observed a logarithmic scaling where $x \sim \ln(f)$. Hsu and Binder (2012) concluded that excluded volume interaction is essential for accurate prediction of F-X in two-dimensional systems regardless of stiffness. Furthermore, they have performed the first 3-dimensional modeling of sufficiently long macromolecules in order to investigate the F-X behavior of semi-flexible chains with EV. Their results indicate that in the presence of EV, the Kratky-Porod model only applies to the rigid and short chains. However, the on-lattice Monte-Carlo (MC) predictions of (Hsu and Binder, 2012) are affected by the lattice model at the high extension region $(x \to 1)$, as the bond radius is fixed at lattice spacing. Also their adopted MC method, unlike BD or molecular dynamic (MD), is unable to predict dynamical properties robustly. Stevens et al. (2012) attributed the logarithmic region of the F-X curve observed in ss-DNA single chain stretching to the unwrinkling of small crumpled segments of the chain, formed due to the condensation of the counterion along the backbone of the polymer in presence of the free ions via the MD simulation of short PE chains $(n = 200)$. Similarly, Toan and Thirumalai (2012) related the F-X logarithmic scaling to the same physical concept, although their model includes only the screened Coulomb potential and no explicit salt, they point to the long range

29

electrostatic interaction as the possible cause of the logarithmic scaling in F-X. In the Toan and Thirumalai (2012)'s MC model the postulated power law decay of bond correlation was reproduced via incorporation of a salt dependent Debye length. As demonstrated shortly, such logarithmic region can be captured without inducing any charge clusters along the polymer chain. Also MD simulation of PE with explicit solvent is costly, especially since the universal elastic behavior can only be obtained for chain with around 1000 Kuhn steps. This limit of Kuhn steps can be explored via BD simulation of the bead-rod model of polymeric chains via highly efficient and parallel algorithm. Cranford and Buehler (2012) utilized MD in order to investigate the relationship between the electroestatic contour length and intercharge distance, and provided a modified equation for the OSF formulation to encompass both flexible and rigid chains. The PE model in their MD model has finite length and the solution is in the salt-free condition. Both Pattanayek and Prakash (2008); Stoltz et al. (2007) modelled PE solutions as a chain of swollen blobs via the BD with FENE springs. The bead-spring model inherently cannot capture the effect of salt concentration on the Kuhn length nor can it capture the 2/3 non-linear region discussed above due to linear nature of FENE force law at small extension.

In this work, in order to construct the universal map for the fractal dimension of the polymeric chain in terms of fraction of charged units and salt concentration, hi-fidelity BD of macromolecules with the bead-rod micro-mechanical model with excluded volume constraints of varying range is utilized to model the flexible PE chains. Our results show that the scaling behavior of the chain correlation measure against the salt concentration is linear, in agreement with the Muthukumar, Barrat and Joanny prediction (Muthukumar, 1987; Barrat and Joanny, 1993), only when charge density is close to $1/l_o$ for regions (IV) and (V).

Finally, the F-X behavior of chain in various salt concentrations is explored, and the result is compared to the theoretical scaling laws and experimental curves found via the single chain experiments. In addition, in an important step towards coarse-graining PE chains, a new spring force law that correctly includes the repulsion effects

of screened ionized groups or the good solvent effect is established, similar in spirit to the Cohen methodical extraction of FENE force law from Inverse Langevin force law (Cohen, 1991). To this end, a new method for real function approximation is developed, verified and applied to the result of BD simulation in order to obtain the corresponding force law from of the discrete set of data points.

3.2   Simulation method and model parameters

In BD simulations of the bead-rod model (BDRD) of macromolecules, trajectories are evolved in time by stochastic integration of inertialess Langevin equation. Corresponding thermodynamic properties of this ergodic system at steady state can be found by averaging over all trajectories or over time. In the BDRD, forces act on the beads. Hence on each bead:

$$F^{(B)} + F^{(C)} + F^{(D)} + F^{(EV)} = 0 \tag{3.1}$$

where $F^{(EV)}$ is the exclude volume force, $F^{(B)}$ is the Brownian force, $F^{(C)}$ is the connector force applied along the connected rods and

$$F^{(D)} = \zeta \left(\dot{r}_i - u_i^s \right) \tag{3.2}$$

where ζ is the isotropic hydrodynamic drag, $\dot{r}_i$ velocity of bead i, u_i^s solvent velocity at bead i. These beads are connected by rods with constant length l_o :

$$\left(r_{i+1} - r_i \right)^2 = l_o{}^2 \tag{3.3}$$

where r_i is ith bead position in the Cartesian coordinates. The constant force ensemble is adopted in order to measure the F-X behavior. Specifically, on the first and last bead the applied tensile force (f) acting along the end-to-end (EtE) direction of the chain, is added to the Langevin equation. The Langevin equation subject to the

constraint in the equation (. 3.3) is solved via a predictor-corrector scheme (Liu, 1989; Öttinger, 1996; Somasi et al., 2002). At the first step, the unconstrained displacement of beads is due to the forces calculated at the last time step plus the random force:

$$r_i^* = r_i + \left[u_i^\infty + K.r_i + \zeta^{-1}.F_i^{EV} \right] \Delta t + \sqrt{2k_BT\zeta^{-1}}\Delta W_i \tag{3.4}$$

here K is velocity gradient tensor, ΔW_i is the Wiener process represented by a Gaussian random number with a mean of zero and variance equal to Δt and the screened electrostatic repulsion force, represented by the exclude volume potential, is calculated based on the positions of all beads at the beginning of the step from the WCA potential:

$$U(|r_i - r_j|) = \begin{cases} 4\epsilon \left[\left(\frac{\sigma}{|r_i-r_j|} \right)^{12} - \left(\frac{\sigma}{|r_i-r_j|} \right)^6 \right] + \varepsilon & |r_i - r_j| < 2^{\left(\frac{1}{6}\right)}\sigma \\ 0 & |r_i - r_j| \geq 2^{\left(\frac{1}{6}\right)}\sigma \end{cases}, \tag{3.5}$$

therefore the force cut-off is determined by $\kappa^{-1} \sim d_{bead} = 2^{\left(\frac{1}{6}\right)}\sigma$ and ε is related to the field strength.

At the corrector step, all the constraint must be satisfied. This includes finding the Lagrange multipliers from equation (3.3) and ensuring that any two beads closer than d_{bead} are moved away based on the WCA force.

$$\left[r_{i+1}^* - r_i^* + (F_{i+1}^{(C)} + F_{i+1}^{(EV)} - F_i^{(EV)} - F_i^{(C)})_\lambda \right]^2 = l_o^2 \tag{3.6}$$

Subscript $\lambda \in [0, 1]$ here indicates that the term in parentheses is evaluated at the configuration $(1 - \lambda)r_i + \lambda r_i^*$. Selection of $\lambda = 0$ and $\lambda = 1/2$ corresponds to Ito and Stratonovich integration, respectively; in the absence of HI, λ can be chosen arbitrarily. It was observed that $\lambda = 1$ will reduce the number of iteration, increases performance, and has no effect on the properties of the macromolecule presented in this paper when compared to Ito restoration of constraint, thus this value was set for λ. The aforementioned algorithm is implemented in a parallel

32

programming environment. Equations were nondimensoinalized as follows: l_o serves as the characteristic length scale, the characteristic time scale is bead diffusion time $\zeta l_o{}^2/k_B T$ and forces are made dimensionless with $k_B T/l_o$. To solve the nonlinear set of equations, an iterative method must to be adopted. The Newton-Raphson (NR) method generally converges faster than Picard method, provided the gradient of matrix of coefficient is found analytically and the initial guess is a good approximation of the solution. The weakly coupled set of constraints allow analytical calculation of the gradient of the nonlinear equations and construction of the matrix of coefficients. To overcome the later shortcoming and take advantage of the quadratic convergence of the NR method, both methods are combined in the code: specifically, if the NR solutions do not converge after a certain number of iterations, the solution algorithm at the corrector step automatically switches to Picard method. This usually happens in the few steps at the beginning of the run. Both methods must satisfy the convergence criterion: each rod length relative error must be less than 1e-7 and contour length variation must not exceed 1e-5. Results presented here are obtained with $\Delta t = 10^{-4} - 0.8 \times 10^{-3}$, n ranges from 50 to 1000 and number of trajectories is either 128 or 256. Bead diameter was set to 0.9 at the athermal limit and ε is set equal to $\sqrt{\Delta t}$. The relation between ε and dt is further discussed in the next section.

Padé approximants of a function, $f(x)$, is found by finding coefficients of the rational function of order (k, m) which preserves possible presence of poles in function comparing to a simple Taylor expansion. Normally this is done by a Maclaurin expansion of the analytical function and then finding the coefficient of polynomial $P_k(x)$ in numerator and $Q_m(x)$ in the denominator.

$$R_{(k,m)}(x) = \frac{P_k(x)}{Q_m(x)}. \tag{3.7}$$

Cohen applied this technique to find a more accurate approximation of the Inverse Langevin force law than the force law proposed by Warner (Cohen, 1991)and also

showed that Warner force law (FENE) is in fact a rounded form of Cohen's Padé approximation.

To construct a force law in the form of a rational function (Eq. 3.7) from BD or single molecule experimental results, a new method is developed. Our approach starts by taking $k + m + 1$ data point in order to find the $k + m + 1$ unknown coefficients of R. Afterwards, P and Q are divided by their common factors, and finally, coefficients of the new $P'_{k'}(x)$ and $Q'_{m'}(x)$ are normalized by the coefficient of the x zeroth order of the polynomial at the demoninator $(Q'_{m'}(x))$ to determine coefficient of the new force law $R'_{(k',m')}$. In order to show its accuracy, this method was first tested against Cohen's Padé expansion of IL function and successfully predicted the coefficients of the force law for $m' = 2$.

3.3 Results and discussion

In the following section, probability distribution function and EtE distance scaling with number of Kuhn steps obtained from simulation are compared with the theoretical values which confirms accuracy of modeling technique and parameters. Furthermore, fractal dimension of the chain in the A and B variable space is discussed in order to construct a universal map of the chain fractal dimension as a function these two dimensionless variables for large n. First, the equilibrium properties are discussed, followed by the discussion of the F-X properties and the effect of both A and B parameters as well as the chain length on the aforementioned properties. Finally, this section is concluded with introduction of the new discrete Padè expansion and force law at the limit of real chain.

3.3.1 Equilibrium properties

The Magnitude of the pre-factor of the WCA potential is chosen according to the magnitude of the time step in order to insure accurate incorporation of the excluded
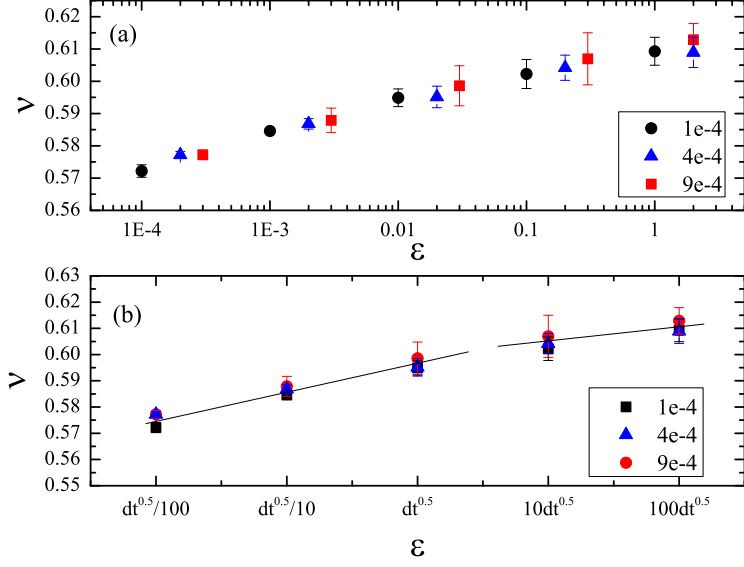
Figure 3.2: The scaling exponent of r_e for various magnitude of time steps vs. the WCA potential pre-factor. The bottom graph, (b), demonstrates the same data vs. rescaled values of ϵ with the corresponding magnitude of time step; for instance $10dt^{0.5}$ means $\epsilon = \sqrt{dt} \times 10$

volume around each bead. At equilibrium, the magnitude of the Flory exponent from various time steps and choices of ϵ (Fig. 3.2-a) collapsed on the same curve when plotted against $\epsilon/\Delta t$ (Fig. 3.2-b) and for $\sigma = 0.8$. The correct scaling is achieved when $\epsilon/\sqrt{\Delta t}$ is on the order of unity or $\epsilon \approx \sqrt{dt} \approx O(dx^{ran})$, where dx^{ran} is the displacement due to the random force.

The probability distribution of the mean squared end-to-end distance, $P(r_e)$ is known theoretically for both the neutral ideal chain and SAW chains, which is the limit of the PE chain when $A = B = 1$, i.e. the crossing point of the axis in Fig. 3.1a and Fig. 3.1b. Fig. 3.3 depicts the result obtained from the BDRD as well as the theoretical limits, which verifies the accuracy of the BDRD in both cases. It also demonstrates the higher accuracy at small r_e compared the Gaussian EV potential (Rey et al., 1992). The observed Higher accuracy at low r_e in this work is expected since, unlike the Gaussian potential which reaches a finite value (i.e. zero force) at very small bead distances, the WCA potential repulsive force increases monotonically. Furthermore, scaling arguments state that at equilibrium, r_e scales with $n^{0.5}$ for
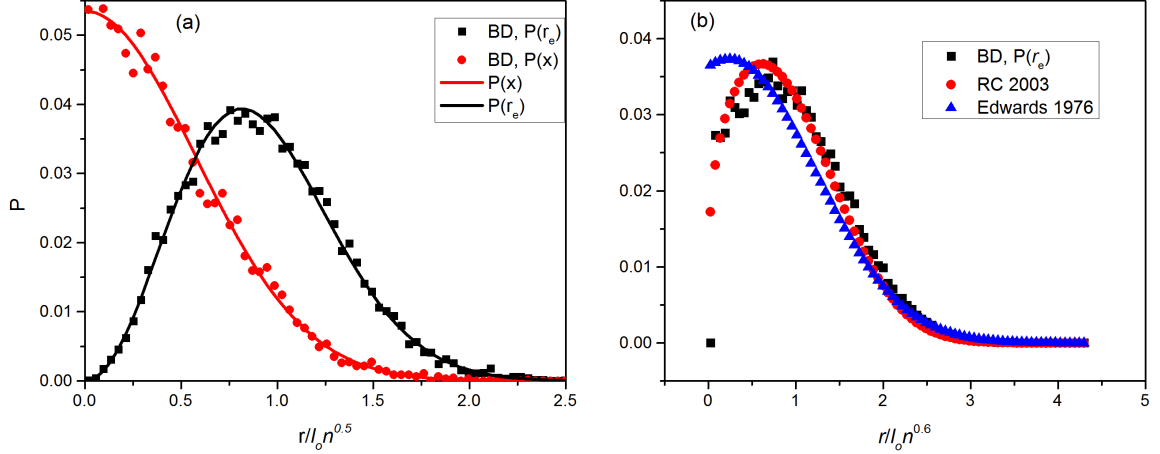
Figure 3.3: Probability distribution function of the ideal chain (a) and real chain (b) obtained from simulation is compared to the theoretical curves (solid lines calculated from Rubinstein and Colby (2003)).

a chain with no excluded volume constraint (Ideal chain) and $n^{0.6}$ for chains with excluded volume (Real chain or good solvent condition). The excellent agreement of the current BDRD with the theoretical prediction of r_e scaling vs. number of Kuhn segments is further demonstrated in Fig. 3.4, for both ideal and real chains with various time steps.

Next, the possibility of creating a universal plot for the set of fractal chain dimensions (Flory exponent) is investigated as a function of both A and B. Blob theory suggests that PE chain can also be considered as Gaussian chain of electrostatic blobs, where the blob diameter is increased due to the electrostatic repulsion between the ionized groups in the blob. The translation of this assumption to the present model, suggests renormalization of the bead electrostatically induced excluded volume diameter with the number of bonds between the consecutive ionized units. The universal curve obtained with the aforementioned renormalization is depicted in Fig. 3.5-b. There are three distinct regions in this plot: for very small diameters chains do not swell, while in the second region the fractal dimension changes almost linearly, as B exceeds unity, a nonlinear thirds region with smaller slope is found. The two later regions are highlighted by the observed jump in the scaling exponent
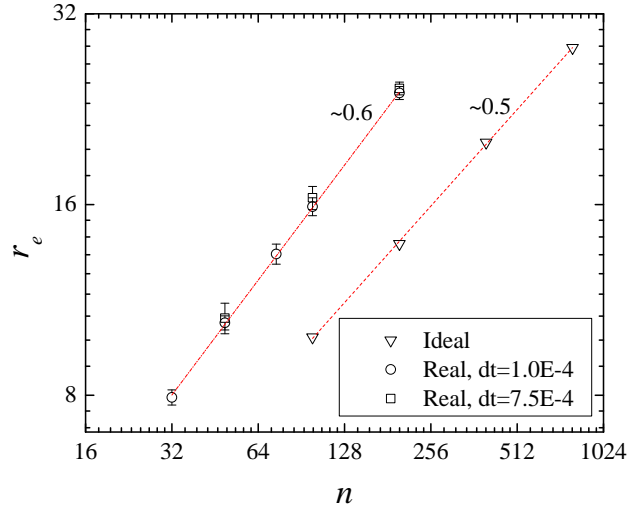
Figure 3.4: Magnitude of r_e for different chain sizes in a log-log plot. Scaling exponents agree with the theoretical values of 0.5 for ideal chain (theta solvent condition) and 0.6 for a real chain (good solvent condition).

of the expansion factor $(r_g/r_{g,\theta})$ vs. the B parameter (Fig. 3.6). As depicted in Fig. 3.6-b, at intermediate salt concentration the relative magnitude of the radius of gyration linearly varies with κ^{-1} with slope less than one. The comparison between $A = 3$ vs. $A = 1$ in Fig. 3.6-b reveals that the effect of salt concentration on the equilibrium expansion factor drops rapidly as the distance of ionized unit along the contour increases. These findings are in qualitative agreement with the experimental data for K-PolyStyren Sulfonate ($l_o \approx 2.4$ nm) (Hara, 1993).

As shown previously for WLC chains via MC simulation (Schäfer and Elsner, 2004; Hsu et al., 2013), the bond auto correlation of the chains with excluded volume potential does not follow the single exponential decay and the resulting decorrelation length. Hence, in order to investigate the dependency of l_{ES} on salt concentration, first it is necessary to introduce the measure of decorrelation length for chains with EV interaction. The linear or quadratic relationship between the Kuhn step and the salt concentration is then investigated through the relationship between the introduced measure of decorrelation and parameters A and B. A measure of decorrelation length

37
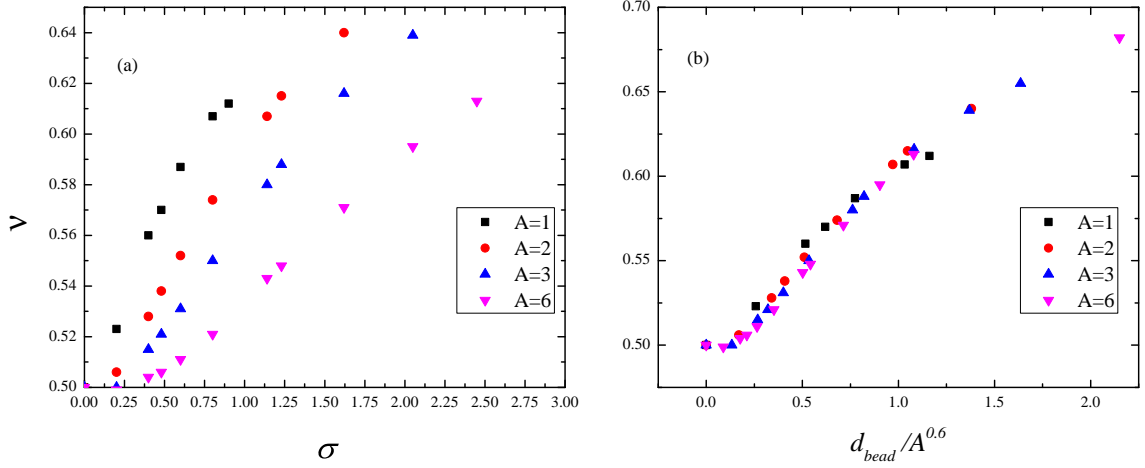
Figure 3.5: The fractal dimension of the PE chain for a wide range of salt concentration and A values. In both plots the repulsion effect of ionized groups are presented via the excluded volume σ (a) or via the excluded volume diameter of the bead rescaled with $A^{0.6}$ (b). In the later case all the data collapses on a single curve.
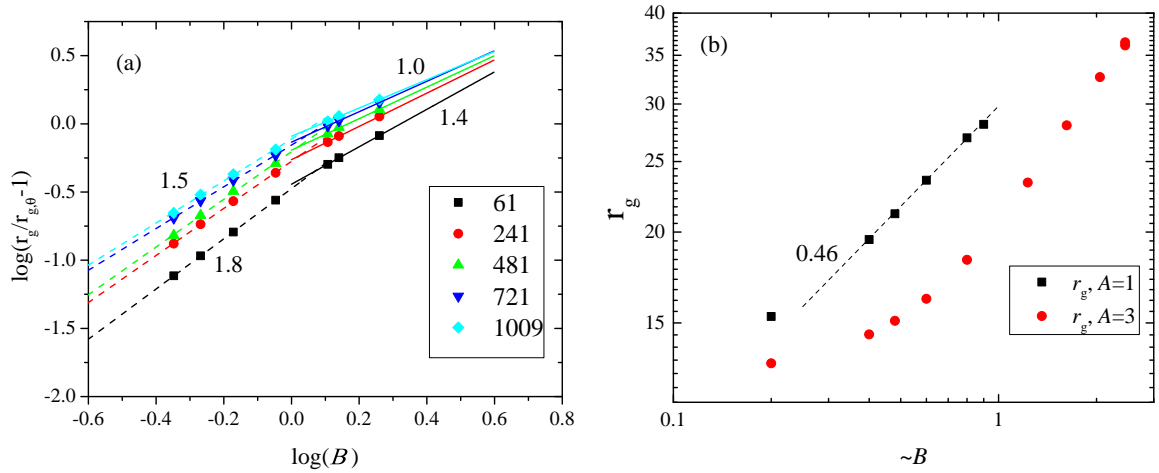
Figure 3.6: The logarithmic plot of the expansion factor illustrates two distinct regions as parameter B increases for various chain sizes for $A = 2$. The slopes are highlighted by the two linear fit (dashed line for $B < 1$ and solid line for $B > 1$). Plot on the right compares radius of gyration of $A = 1$ with $A = 3$

for these chains can be found through the bond auto correlation function defined as $\cos \theta(s) = r_i.r_{i+s}/{l_o}^2$, which characterizes the projection of bonds s link down the contour length on the direction of ith bond. As correlation dies out along the chain, bonds orientation becomes independent at distance s' measured along the chain, this value $(\cos \theta(s'))$ approaches zero. The ensemble average of these single bond projections is considered as the measure of the l_{ES} in this research; as expected l_{ES} is zero for the neutral chain in Θ-solvent. Three power law scaling regions are observed in Fig. 3.7, which depicts $\cos^2\theta(s)$ for PE chain for $A = B = 1$, suggesting that the β exponent of $\cos \theta(s) = s^{-\beta}$ is respectively equal to 0.84, 0.95 and 1.03. The first exponent is in good agreement with that of the WLC chain models in good solvent, while the last region is characteristic of the FJC and characterizes the decorrelation of EV in a bonded chain. As shown in Fig. 3.8 the intermediate scaling region is not observed for small chains ($n = 60$); meanwhile as n increases, the bond correlation function approaches a universal behavior with all three regions of the power law scaling.

In the case of $A = 1$, Fig. 3.9-a clearly demonstrates the linear effect of salt concentration, represented by bead radius, on the electrostatic Kuhn length in both regions (IV) and (V) confirming results of (Barrat and Joanny, 1993). Similar scaling was also found utilizing the alternative measures of maximum Kuhn length defined elsewhere ($l_{o,\max} \sim (n/2)^{2\nu-1}$) (Schäfer and Elsner, 2004) as depicted in Fig. 3.10. However, as the distance between ionic groups along the contour increases (Fig. 3.9-b through d), the electrostatic Kuhn length across both regions demonstrates quadratic behavior. This observation suggests that the transition from the linear scaling into the quadratic scaling, proposed by the OSF theory, depends on the fraction of ionized groups relative to the Kuhn length, and as this value approaches unity the linear salt concentration dependence of the l_{ES} is recovered. In order to obtain the universal mapping of l_{ES}, its dependency on the chain length should be investigated. For $A = 1$, power law function in the form of $b(n - 2)^{\alpha}$ with $\alpha = 0.41$ fits the data for all n values, and the constant b is equal to $\cos \theta(1)$ which is independent of n for any
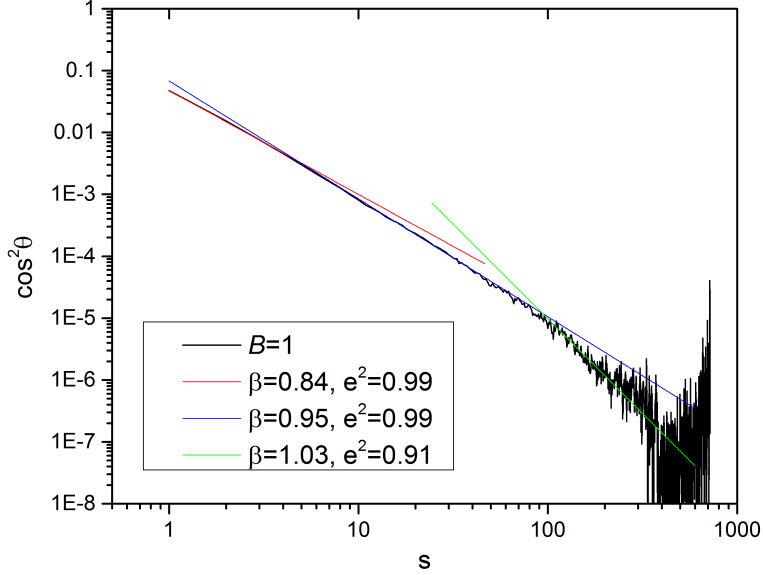
Figure 3.7: The power law decorrelation of squared bond auto-correlation function for the chain in the athermal solvent. Three different slopes (in the log-log plot of $cos(\theta(s)) = s^{\beta}$ shown as β with the r-squared value (e^2) in the legend) can be identified via linear fit of the autocorrelation function.

given κ^{-1} (Fig. 3.11). Although not explored here, a similar approach can be used to resolve the variation of l_{ES} for $1 < A$.

3.3.2 F-X response

Salt concentration dependence of F-X scaling of PE with various ionized unit fraction is investigated via constant force ensemble for various numbers of Kuhn steps. In order to establish the universal limit, the special case of $A = B = 1$ is considered first. Next, the influence of salt concentration in the context of our model of PE is investigated. In turn, the excellent agreement between modeling predictions with the recent single molecule experiments is discussed.

In Fig. 3.12, FE curve for a real chain ($A = B = 1, n = 500$) is compared with an Ideal chain ($n = 500$). Ideal chain data fit perfectly on the Langevin function, which is the theoretical limit as $n \to \infty$. Real chains deviate from this behavior and show a nonlinear region; also, their response to the constant tensile force depends
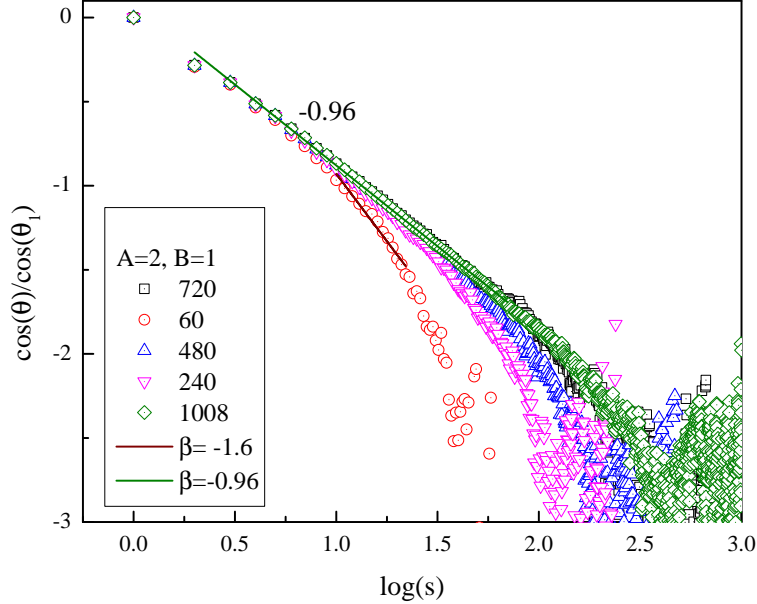
Figure 3.8: Normalized bond autocorrelation function along the chain in Athermal solvent. Note that for the small chain ($n = 61$) the intermediate scaling region is absent and for large n curves reach a universal behavior.

on the number of Kuhn steps. The later fact is further investigated by varying n ranging from 100 to 1000. As Fig. 3.14 depicts, for chain with limited number of Kuhn segments, FE curve hardly deviates from the linear response at forces less than unity and its behavior is close to a FENE force law, whereas chain reaches a universal behavior for n larger than about 500.

This gradual shift from a FENE force law to the excluded volume limit is investigated on a logarithmic plot of extension versus force. The logarithmic plot (Fig. 3.14) clearly divides a real chain response into 4 regions for long chains, i.e $n > 500$. At the first region (Reg.I), close to equilibrium, the chain response in slightly sub linear, which means that chain resists against extension a bit more in comparison with the theoretical 2/3 limit. Although linear response close to equilibrium is expected, the slight variation is due to the virial pressure that arises from the excluded volume potential. The order of force due to internal pressure can be found by assuming that the polymer is bounded inside a sphere with radius equal to the chain radius of gyration. This force in Reg.I is almost comparable to the applied

41
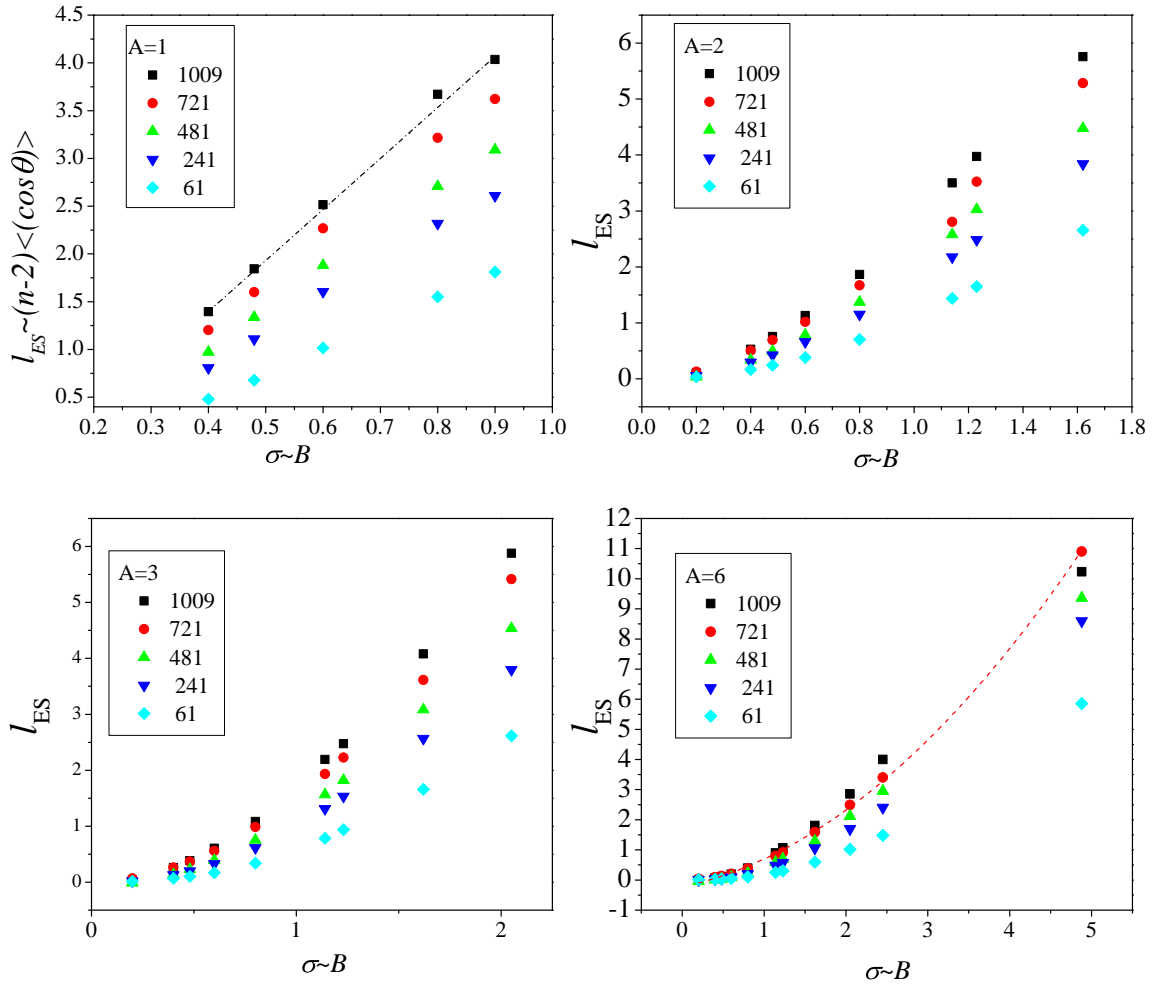
Figure 3.9: The electrostatic Kuhn length for four different values of A over the range of B parameters encompassing regions (IV) and (V) of 3.1. While for small A, l_{ES} tends to grow linearly, as A increases a quadratic function fits the data in both regions (IV) and (V).
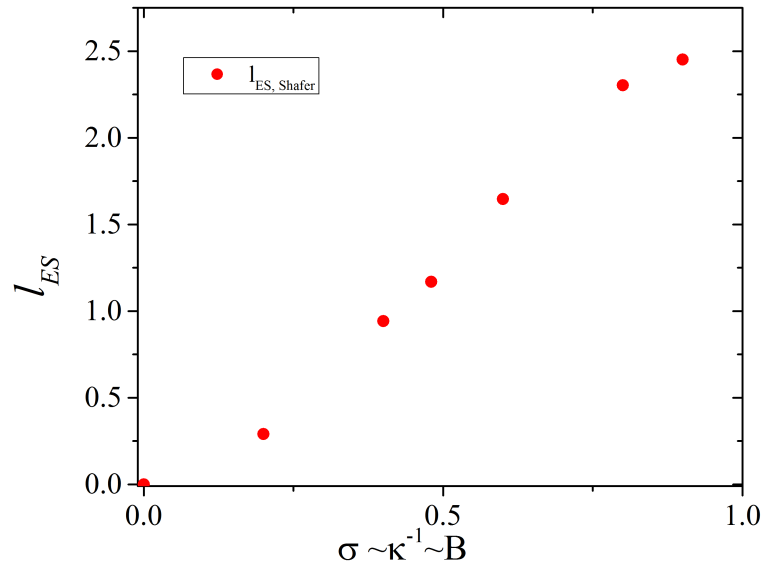
Figure 3.10: Application of alternative measures of Kuhn length, confirms the findings of Fig.3.9 and demonstrates that the total Kuhn length depends linearly on parameter B.
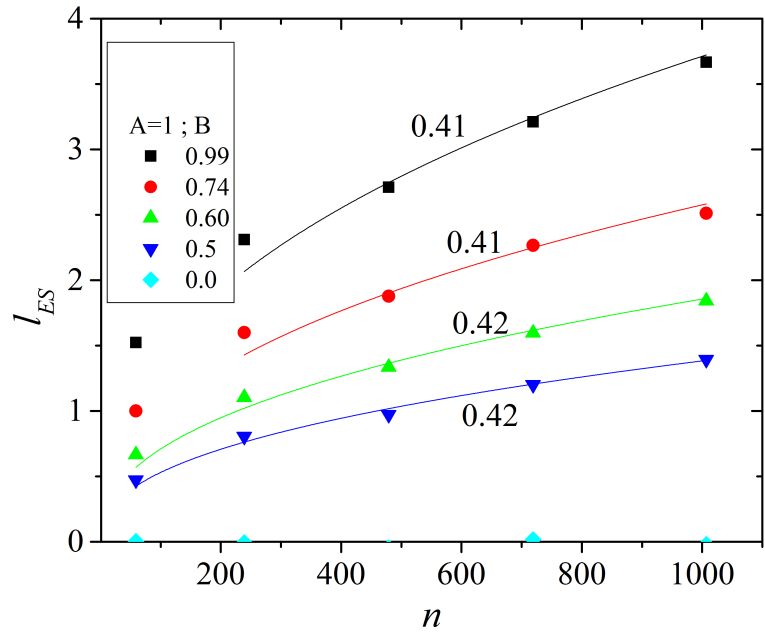
Figure 3.11: The n dependence of the Kuhn length follows a power-law function with a fixed universal exponent (0.41) and a known coefficient, $\cos\theta(1)$, which depends on the salt concentration.

tensile force; however, as end-to-end distance increases, pressure drops rapidly. In other words the additional force acting towards swelling of the polymer coil goes to zero, and therefore the net force assisting the extension decreases and this creates an effective resistance to chain extension. At the second region (Reg.II), the slope for large n is about 0.66, which perfectly agrees with the scaling, arguments discussed before. The third region (Reg.III) slope gradually changes from 0.6 for $n = 50$ (same value can be obtained from a FENE force law) to 0.5 for a real chain at the universal limit. The third region is a prelude to the finite extensibility region (4th region), and sometimes is not regarded as a separate response region. (Scaling exponents extracted from this plot are tabulated in Table 3.1.)

The experimental result for the F-X of ssDNA concludes that γ increases from $2/3$ to 1 as the salt concentration increases for $fl_o/kT < 1$, however all the F-X curves for various salt concentration collapse for large values of force. Fig. 3.15 demonstrate similar behavior in the BDRD as κ^{-1} decreases. This finding is in perfect agreement with the aforementioned single chain experiments (Saleh et al., 2009). Decreasing parameter A, at a fixed κ^{-1}, can also increases the nonlinear F-X behavior, i.e. increasing the charge fraction or closer distance of charged unit along the backbone increases the nonlinear response up to the limit observed in Fig. 3.15 for $A = 1$.

Due to the importance of excluded volume interaction, weather it originates from the good solvent effect or electrostatic repulsion, an explicit F-X law, that accurately captures all the non-linear regions, is established in the form of a real function for these limits via the discrete Padé expansion. Fig. 3.17 shows the accuracy of the proposed method for the Inverse Langevin function. The rational function has accurately captured finite extensibility and linear initial region of the original curve, even with limited number of data points. $R'(3, 2)$ approximation to the IL force law exactly fits on the Cohan's Padé expansion, using only 8 data points in the mid extension region. The higher order approximation shows even better agreement with the IL force law. Inset plot compares the accuracy at high extension region.

Fig. 3.18 shows the approximated F-X curve for a Real chain ($n = 700$). If points are merely chosen from the 2/3 scaling regions force law is generally more concise however region (I) slope would not be greater than 0.7. Note that even in this case, the difference in the magnitude of force in the whole region is negligibly small. A more precise force law is obtained by involving data points from all four regions (Table 3.2); this new force law is shown in Eq. 3.8 and captures forces in all extensions accurately.

In summary, it is shown that incorporation of EV divides the flexible chain F-X curve into four distinct regions. The curve always starts with a close to linear region and then goes to the theoretical limit where extension is scaled with $f^{2/3}$ for chain with enough statistical segments. Finally, the results were transformed into a real function:

$$f(x) = \frac{1.5674x^3 - 0.669x^2 + 1.237x}{-1.92x^3 + 3.25x^2 - 2.285x + 1.0} \tag{3.8}$$

the polynomial nature of this form of force law enables accelerated study of polymeric chains using the established methods for bead-spring methods

3.4 Summary

In summary, equilibrium properties and F-X behavior of PE chain were explored via BDRD model of polymeric chain in three important regions, namely (I), (IV) and (V) ($B < A$), and results were closely compared to available experimental data. The proposed model captured several regions of the postulated phase diagram based on non-dimensional parameters A and B, and the Flory exponent universal curve was established for various linear charge densities. In addition, at equilibrium we confirm the theoretical work of MBJ that $l_{ES} \sim \kappa^{-1} \sim c_s^{-0.5}$. Furthermore, l_{ES} scaling was mapped into the two parameter (A and B) space for a wide range of salt concentration.

F-X curve was explored utilizing this model and our results indicate good agreement with the available single chain experimental data obtained for ssDNA. Effect of salt concentration and fraction of ionized groups where explored in regions
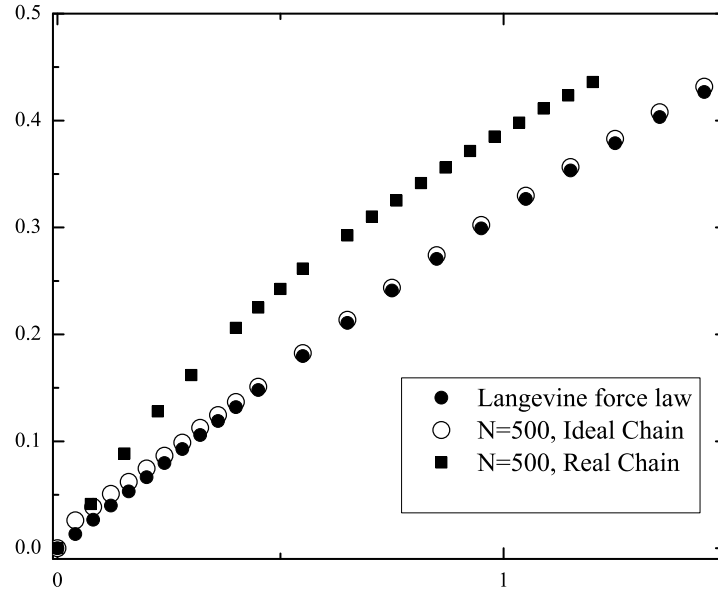
Figure 3.12: Comparison with theoretical force law shows that constant force ensemble and the proposed method predict the Ideal chain elasticity with great accuracy even for very small forces. Standard deviation is less than 5% for any $f > 0.1$ and for the sake of clarity error bars are not included in the graphs.

(IV) and (V). In addition, for the important case of $A = B = 1$, which correspond also to athermal solvent, a novel force law capable of capturing all the different regions of F-X curve was extracted via a new method, i.e. discrete Padè expansion.
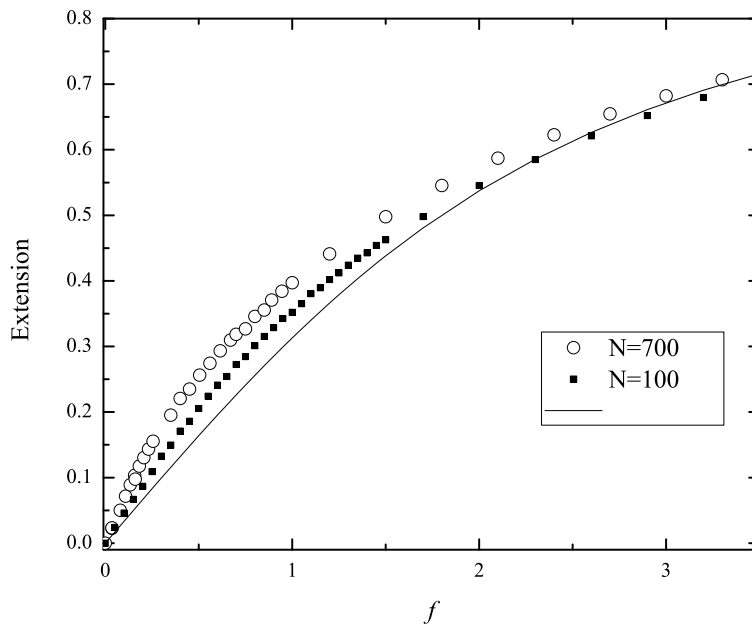
Figure 3.13: Normal plot of force extension. Notice that extensional behavior does not collapse on the Ideal chain F-X curve immediately after 1 but rather until about 60% extension it still shows a significant difference. This difference completely disappears at higher extensions (see Fig.3.14)
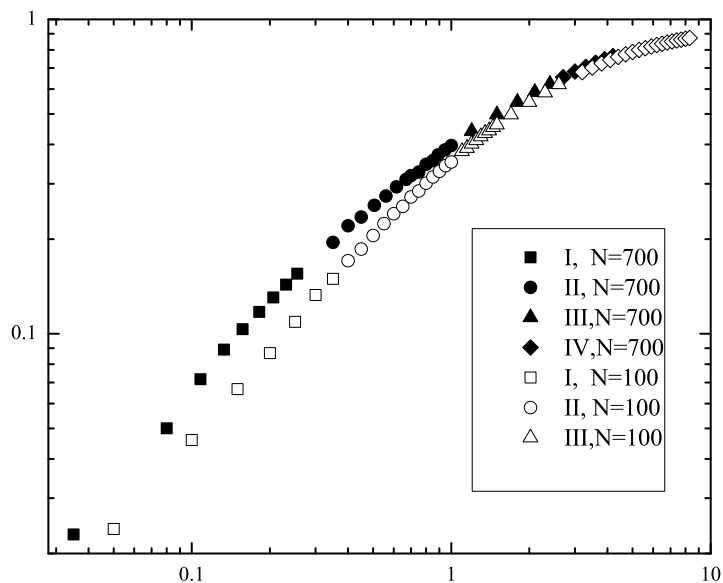
Figure 3.14: Logarithmic plot shows different regions of FE curve. Distinction between these regions obscures as n decreases. The universal limit can be reached for a chain with large number of Kuhn steps as shown in Table 3.1.
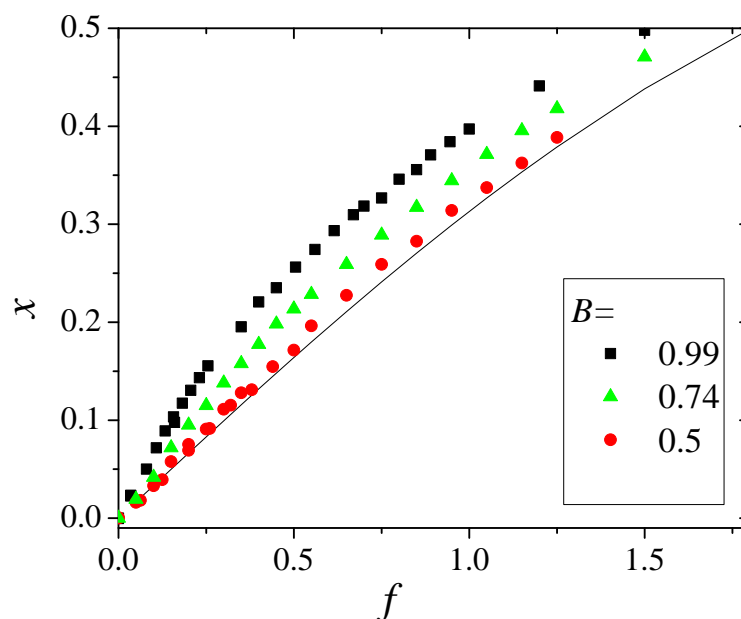
Figure 3.15: Effect of salt concentration on the F-X curve of sufficiently long chains ($n = 720$). Data shows agreement with the experimental measurement Saleh et al. (2009). As the salt concentration increases, F-X behavior approaches the ideal F-X curve and the non-linear region disappears.
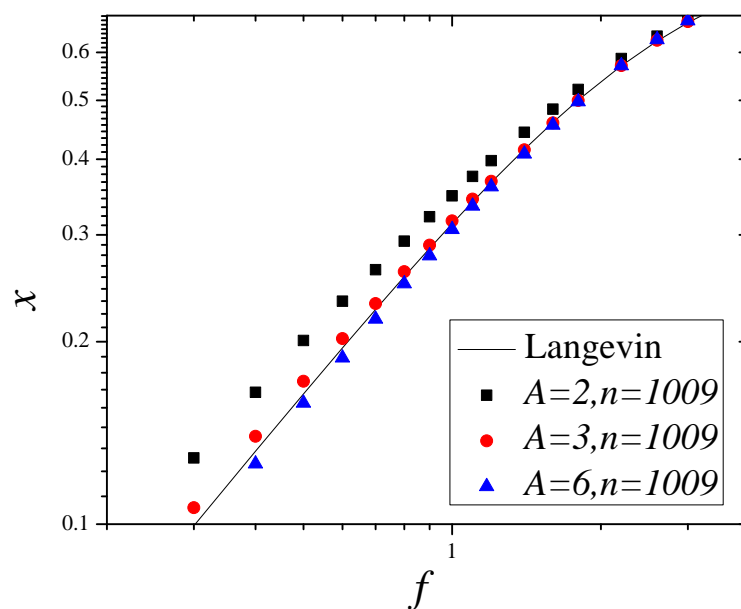
Figure 3.16: Effect of fraction of ionized group, represented by parameter A, on the first non-linear region of F-X curve.
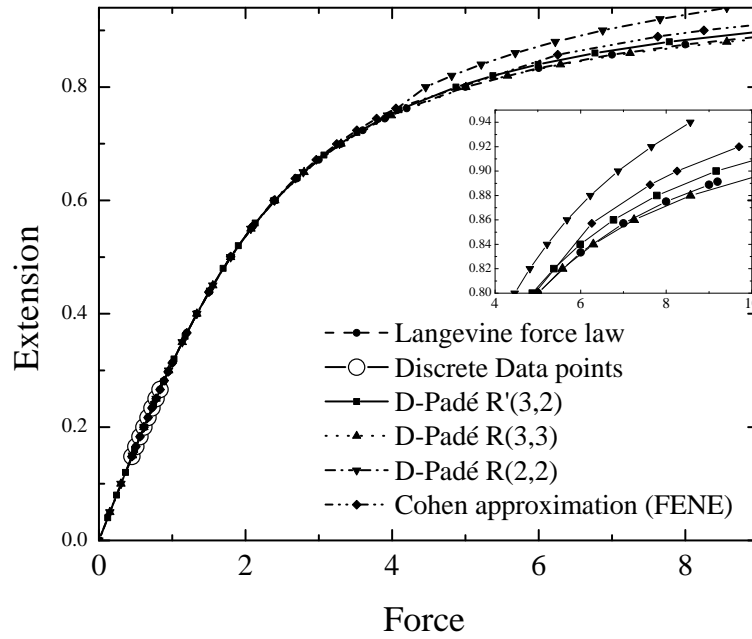
Figure 3.17: Validating the D-Padé approximation method with known functions. Inset shows relative accuracy at the finite extensibility region.
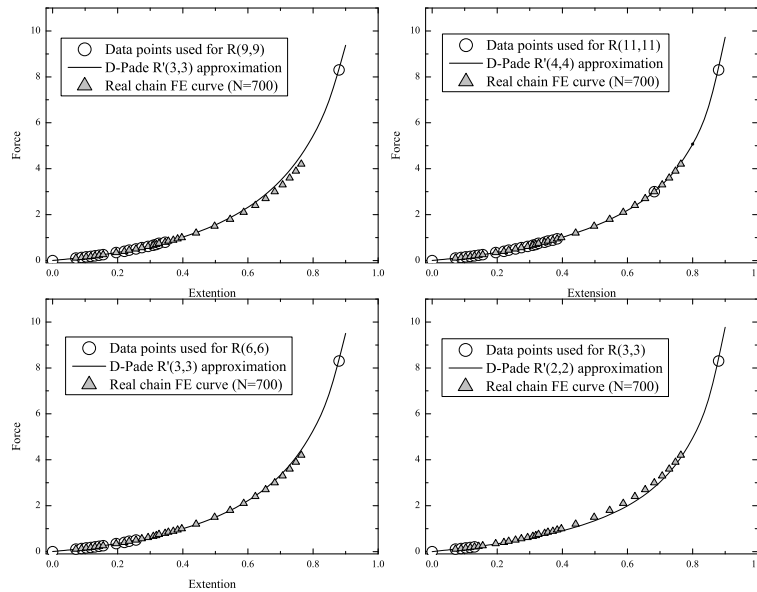
Figure 3.18: Various D-Padé approximations. In general, accuracy increases with increasing initial polynomial order and sampling data points from all regions. The coefficient of each approximation is shown in Table 3.2.

Table 3.1: Exponent γ of $x \propto f^{\gamma}$, where x is extension, for real chain on different regions extracted from linear curve fitting of log-log plot. In order to make comparison more objective, region III were assumed to end at 0.6 extension for all n. Fitting goodness (the R^2 value) for all fittings is greater than 0.990.

n	I (near equil.)	II ($I < f < 1$)	III ($1 < f < IV$)	IV (entropic limit)
50	0.98	0.832	0.606	
100	0.95	0.800	0.590	non linear
150	0.99	0.742	0.534	$0 < \gamma << 1$
250	0.92	0.706	0.526	
500	0.94	0.684	0.528	
700	0.93	0.661	0.495	
Ideal chain		1		non linear

Table 3.2: Coefficients of Discrete Padé approximation are shown here. Fig.3.18 shows accuracy of each force law along with the point that was used to extract the force law.

$R_{n',m'}(x)$	term order of polynomial	0	1	2	3
(2,2) from (3,3)	P coefficients	-0.0007	1.3942	–	–
	Q coefficients	1.000	-0.9685	–	–
(3,3) from (6,6)	P coefficients	0.0032	1.1467	7.0553	–
	Q coefficients	1.000	2.9255	-3.6081	–
(3,3) from (9,9)	P coefficients	0.0015	1.2145	2.5658	–
	Q coefficients	1.000	0.0395	-0.8606	–
(4,4) from (11,11)	P coefficients	0.001	1.2371	-0.6689	1.5674
	Q coefficients	1.000	-2.2853	3.250	-1.9198

Chapter 4

HI-FIDELITY BROWNIAN DYNAMICS SIMULATION OF NON-EQUILIBRIUM PROPERTIES OF MACROMOLECULES IN GOOD SOLVENTS: A BOTTOM-UP APPROACH

Recently, through the Hi-Fidelity Brownian Dynamics (BD) of the bead-rod model of the polymeric chain, a new force law in the form of a real function was developed, which accurately represents force-extension behavior of a single macromolecule in good solvents. Here, both analytical and BD methods are employed in order to explore the effect of solvent quality on both equilibrium properties and dynamical behavior, through this bottom-up approach. Results indicate that the new force law captures

features such as higher shear-thinning at mid range of Weissenberg number (Wi) and decreasing the slope of the coil to stretch transition, which is absent in models constructed by simply superimposing the excluded volume on the purely entropic force laws.

4.1 Introduction

In the previous chapter, a novel force law with accurate incorporation of both the entropic and the excluded-volume effects on the force extension behavior was developed based on a bead-rod macromolecular model. The high computational cost of bead-rod models makes the coarse-grained bead-spring model the preferred method in applications such as multi-scale modeling where coarse-graining certain features of the internal chain dynamics in favour of performance does not jeopardize the validity of the final result. In the bead-spring model, the elastic response of the chain is represented through the spring force law. Theoretical treatment of these models for simple linear force law, i.e., n_s connected linear Hookian springs, leads to the well-known freedraining Rouse model or alternatively the Zimm model in presence of pre-averaged hydrodynamic interaction (HI). The integral form of the constitutive equation and scaling laws of these models are extensively discussed in the literature (Bird et al., 1987; Öttinger, 1996; Rubinstein and Colby, 2003). In the case of nonlinear force laws such as finitely extensible non-linear (FENE) spring, for the elastic dumbbell model, equilibrium properties and rheological quantities at the limiting flow strengths ($Wi << 1$ or $1 << Wi$) are found analytically, while closed form constitutive equations are developed through the closure approximations (Du et al., 2005). Therefore, BD simulation of bead-spring model (BDSP) provides an accurate description of the polymeric chain unaccessible via theoretical treatments when nonlinear effects and configuration dependent potential are significant. BDSP have been used in various flow kinematics (Fetsko and Cummings, 1995; Doyle et al., 1997; Lyulin et al., 1999; Hur et al., 2000; Jendrejack et al., 2002; Somasi et al., 2002;

Hsieh and Larson, 2004; Pamies et al., 2005) to analyze phenomena such as coil-stretch transition (C-S)(Schroeder et al., 2004; Somani et al., 2010; Radhakrishnan and Underhill, 2012, 2013), polymer adsorption (Panwar and Kumar, 2005; Hoda and Kumar, 2008) and even behavior under confinement(Jendrejack et al., 2004; Trahan and Doyle, 2010).

Nevertheless, the underlying assumption of Gaussian chain model at equilibrium and the resulting linear elastic behavior at low extension, which is the common feature of the entropic force laws used in BDSP, is inaccurate for real chains and the Gaussian distribution is perturbed, for instance, in a good solvent (Pincus, 1976), under confinement, close to solid boundaries (Woo et al., 2004), and as it was shown in the previous chapters for polyelectrolytes. Therefore, either through detailed theoretical approaches (Woo et al., 2004) or ad-hoc force laws (Radhakrishnan and Underhill, 2012), there have been several efforts to incorporate the non-linear effects at low and medium extension regions into the spring force law. The process introduced in chapter 3 combines hi-fidelity efficient BDRD and discrete Padè expansion in order to provide an invaluable tool in development of new spring force laws that accurately represent the various scaling regimes of the macromolecules elastic response. In this chapter, the R44 force law, $A = B = 1$, i.e., at the limit of athermal solvent, is investigated both theoretically and via BDSP. Furthermore, the rheological properties of the new force law are compared to the standard FENE dumbbell model in the presence or absence of HI. In the remainder of this chapter, after a brief discussion of the kinetic theory of the elastic dumbbell model and BD of bead-spring model with HI, the equilibrium end-to-end distance and its dependence to the nondimensoinalized maximum extensibility of the chain ($\sqrt{b} = q_m^* k_B T / h$ where h is the spring constant and q_m^* is the contour length) is found theoretically and through BDSP. Next, rheological properties and C-S transition of the polymeric chain subject to shear and extensional flow is studied respectively, followed by comparison with the well-established results of the FENE chain.

4.2 Theory and method

In the absence of an external field, the Hamiltonian of the individual macromolecule is $H(R, P) = \phi(R) + k_{KIN}(P)$ where $\phi(R)$ is the potential as a function of beads position vector and k_{KIN} is the momenta dependent kinetic energy. If the pair potential energy is only a function of the subsequent beads linked in the chain, and with the assumption of Maxwellian distribution of momenta, the equilibrium distribution function will become (Bird et al., 1996):

$$\psi_{eq}(Q) = \frac{e^{-\phi/kT}}{\int e^{-\phi/kT}dQ} \tag{4.1}$$

The time evolution of distribution function is found from the Liouville equation: $\dfrac{\partial \psi}{\partial t} = \dfrac{\partial \psi}{\partial R} \cdot \dot{R}$ where $\dot{R}$ can be found from the Langevin equation. In the Langevin equation, the random force acts effectively as a diffusion mechanism of the probability distribution function in the phase space while other forces drive the convection mechanism:

$$\zeta \dot{R} = V_o + (\nabla V_s)^\dagger \cdot R + F + kT \frac{\partial}{\partial R} \ln \psi \tag{4.2}$$

The corresponding stochastic differential equation can be written in terms of a random Gaussian force via the fluctuation-dissipation theorem:

$$dR = (V_o + K \cdot R + F/\zeta)\, dt + \sqrt{2k_B T/\zeta}W, \tag{4.3}$$

where R is the vector of structureless bead positions, V_o is uniform solvent velocity, K is the block diagonal matrix with $K_{i,i} = (\nabla V)^\dagger$, scalar ζ is the single bead Stokes friction coefficient, F is the sum of all forces acting on the bead, except the Brownian force which is represented by the independent Wiener process in the W vector and dt is the time step. In presence of HI, the random forces on beads become correlated through mobility tensor (Y), which at the first level of perturbation is approximated via the regularized Oseen tensor, i.e, the Rotne-Prager-Yamakawa (RPY) tensor, and

eq. 4.3 becomes:

$$R_i^{t+dt} = R_i^t + dt\,(V_o + \mathrm{K}.R_i + \mathrm{Y}.F_i) + W_i, \qquad (4.4)$$

with $\langle W_i(t+dt)W_j(t)\rangle = 2kT\mathrm{Y}\delta(dt)$ and zero mean value. Details of the formulation in terms of connector vector (Q) and numerical evolution algorithm is given in (Somasi et al., 2002) and Appendix B. While the corrector step in the aforementioned algorithm is a semi-implicit, i.e. the unknown force coefficients on the left hand side of the corrector step equation for segment s are calculated at time t:

$$Q_s^{**} + \mathrm{M}_{ss}\cdot F_s^{**} = Q_s^n + \frac{1}{2}\left(\mathrm{K}_{ss}\cdot Q_s^* + \mathrm{K}_{ss}\cdot Q_s^n\right) + \mathrm{M}_{s,1:s-1}\cdot F_{1:s-1}^{**} + \mathrm{M}_{s,s+1:n_s}\cdot F_{s+1:n_s}^* + F^{(random)}$$

it is possible to perform the second step fully implicitly for force laws in the from of a real function (See Appendix B for definition of all terms in the above equation and detailed resolution of the all implicit left hand side). The following section investigates equilibrium and rheological properties of the new force law through a mixture of analytical and computational techniques.

4.3   Result and discussion

The elastic response of the FENE dumbbell model with the maximum contour length of q_m is given as:

$$F^{*s} = \frac{h_{FENE}Q^*}{1 - \left(q^*\big/q_m^*\right)^2}.$$

Here $Q^* = q^*\vec{e}_{Q^*}$ is the connector vector, and h_{FENE} is the spring constant. There are two ways to nondimensionalize the spring force law. The first set of reduced units, which is suitable for further analytical investigation, consists of the extension $(x = q^*/q_m^*)$ and the force scaled with the linear factor of the force law. For this set of reduced units the FENE force law is given as:

$$f = \left(\frac{1}{1 - x^2}\right)x$$

Similarly, the most accurate force law from the d-Padé expansion, R44, will become:

$$f = \left(\frac{1.267x^2 - 0.54x + 1}{-1.92x^3 + 3.25x^2 - 2.285x + 1} \right) x.$$

Alternatively for numerical simulation, the equilibrium length of the corresponding linear elastic spring, $\sqrt{\lim_{x \to 0} (f(x)/x)/k_B T}$, is used to non-dimensionalize the length scale which is equal to $3k_B T/r_e^2$ (Hsu and Binder, 2012) for both ideal and real chains. Therefore unlike the ideal chain (the FENE force-law) for which the pre-factor of modulus is universal, i.e. $h_{FENE}/r_e^2 = h_{FENE}/q_m = 3$, in case of the chain with excluded volume interaction $h_{R44}/r_e^2 \sim n^{-0.176}$, and hence the equilibrium length scale will be n-dependent. Although this conclusion does not affect quantities rescaled with q_m or stress values, it is especially important in the coarse-graining process of the real chain into arbitrary number of springs. In case of the FENE force law, the length is non-dimensionalized with the equilibrium length of one dimensional Hookian oscillator: $\sqrt{k_B T/h_{FENE}}$ and force is non-dimensionalized with $\sqrt{h_{FENE}kT}$, the magnitude of the FENE force law can be rewritten as (the subscript * is dropped for the non-dimensional quantities):

$$F^s = \frac{Q}{1 - q^2 \frac{kT}{h_{FENE} q_m^2}} = \left(\frac{1}{1 - q^2/b} \right) q \vec{e}_Q$$

which introduces the dimensionless extensibility parameter ($b \equiv q_m^{*2} h_{FENE}/kT$). The corresponding nondimensional format of the R44 force law, obtained using $\sqrt{kT/h_{R44}}$ as the length scale in the BDSP simulation, is:

$$F^s = \left[\frac{1.267\left(\frac{q}{\sqrt{b}}\right)^2 - 0.54\left(\frac{q}{\sqrt{b}}\right) + 1}{-1.92\left(\frac{q}{\sqrt{b}}\right)^3 + 3.25\left(\frac{q}{\sqrt{b}}\right)^2 - 2.285\left(\frac{q}{\sqrt{b}}\right) + 1} \right] q \vec{e}_Q$$

Fig. 4.1 compares the R44, FENE force law and the worm-like chain (WLC) force law(Marko and Siggia, 1995). The R44 F-X curve follows closely the FENE force law

curve at the initial linear region and at the high extension limit; since the initial region encompasses very small perturbation from the equilibrium chain end-to-end distance ($x << 1$), higher powers of x are negligible and since both forces are normalized with their equilibrium values near r_e the agreement is expected. At the high extension limit ($x > 0.8$) the EV effects are screened by the chain tension, and hence again F-X behavior is reduced to that of an ideal chin. Meanwhile for the intermediate extensions, R44 force law briefly approaches the WLC F-X curve. This is likely due to the induced bending rigidity imposed by the EV constraint, i.e., hindered rotation due to the finite bead size, and it highlights another unique feature of R44: the over-prediction of extension from Langevin force law compared to the experimental F-X curves does not exist in the proposed new force law.

The equilibrium properties of flexible dumbbell are found from the equilibrium normalized partition function: $\psi(Q) = e^{-\phi/kT}/J_{eq}$, where ϕ is the potential of the spring and J_{eq} is the total partition function at equilibrium (see Table 1). Due to the complexity of the spring potential for both Cohen-Padé force laws and R44 we have opted for numerical integration of the moments of the partition function. The result of this numerical integration accurately matches those obtained from the BDSP. The equilibrium end-to-end distance of R44 demonstrates strong dependency the on maximum extensibility parameter (Fig. 4.2). In order to illustrate that the aforementioned dependency is a characteristic of the non-linear F-X region of the R44 real chain force law, a new F-X function is introduced and due to its resemblance to the linear-locked (Tanner-locked) dumbbell model (Tanner and Stehrenberger, 1971), it is named the *Pincus-locked* model. While the Tanner-locked model enforces a linear force extension behavior, the Pincus-locked model assumes a power-law relation with the exponent equal to 2/3. In both models the extensibility is limited ($0 \leq x < 1$) and the potential is identically zero anywhere outside this range (see Table 2). Since the linear region of R44 is small, at equilibrium this force law is expected to behave similar to the Pincus-locked model. The Pincus-locked r_e^2 is significantly lower compared to that of the linear models, while relatively close to the R44 value (see Table 4.3),
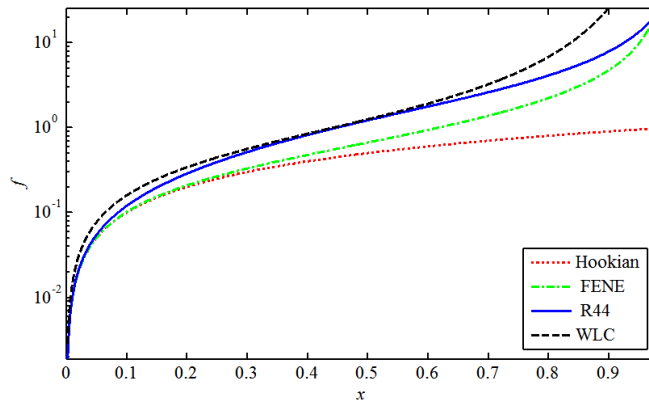
Figure 4.1: Comparison between various force laws with R44 spring

which confirms the increased influence of the extensibility parameter for polymeric chains in athermal (good) solvents.

These findings facilitate the interpretation of the BDSP results; for instance, at equal b, for the R44 force law due to the steeper free energy gradient around equilibrium configuration as seen in the Pincus-locked model, lower equilibrium non-dimensionalized RMS end-to-end distance is expected as confirmed by Fig 4.2. Due to the $n^{-0.176}$ scaling of linear modules and the additional 2/3 force law regime inherent in the R44 force law, the equilibrium results of the FENE force law for $(b^{0.824})^{4/5}$ or $b^{0.66}$ should be comparable to the equilibrium results of the R44 force law. The rescaling exponent determined from the simulation results reported in Fig. 4.2 is ≈ 0.55.

4.3.1   Bead-Spring BD simulation

Next, the non-equilibrium properties of R44 dumbbell are compared with the FENE elastic dumbbell both for shear and planar extension in a range of Pe or Wi. This treatment is further extended to the bead-spring model with $n_s = 20$ for a range of b. Unlike the dumbbell model in dilute solution, HI plays an important role in the dynamics of multi-spring model and therefore it is implemented in the code via the
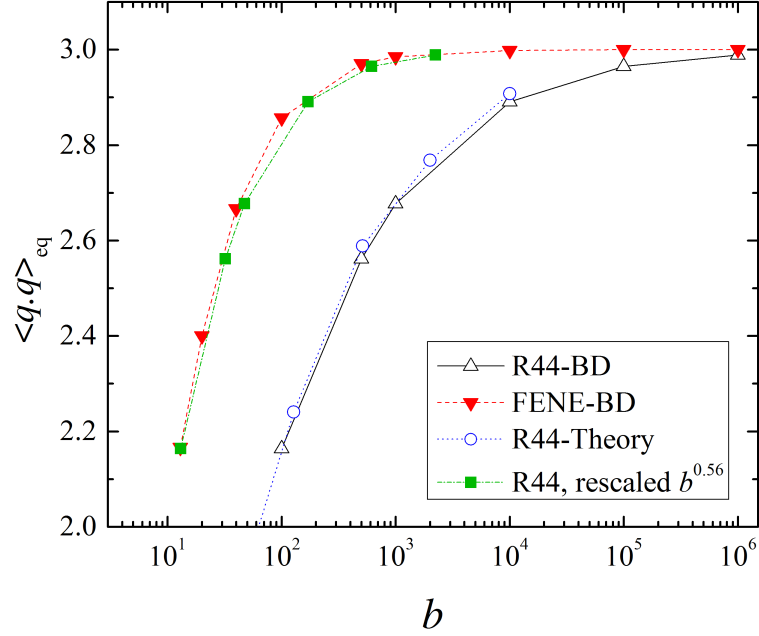
Figure 4.2: Equilibrium end-to-end distance from the BD simulation of the dumbbell model shows strong dependency of Real chain on maximum extensibility factor compared to the FENE force law

Table 4.1: Two entropic springs are compared with the R44 spring in terms of force, potential and the equilibrium end-to-end distance.

	FENE	Cohen	R44
$F(x)$, $x = q/q_m$	$\dfrac{x}{-x^2 + 1}$	$\dfrac{-0.3375x^3 + x}{-0.9428x^2 + 1}$	$\dfrac{1.267x^3 - 0.54x^2 + x}{-1.92x^2 + 3.25x^2 - 2.285x + 1}$
$\begin{aligned}\phi(x)/b &= \\ \int F(x)dx\end{aligned}$	$-\dfrac{1}{2}\ln(1 - x^2)$	$0.1818x^2 - 0.3375\ln(1 - 0.971x) - 0.3375\ln(1 + 0.971x)$	$-0.66x + 0.1952[\arctan(0.5344 - 1.5857x) - \arctan(0.5344)] - 1.085\ln(1 - 0.98x) + 0.125\ln(1 - 1.32x + 1.95x^2)$
$\begin{aligned}\langle q^2\rangle_{eq} &= \\ \dfrac{4\pi q_m^3 q_m^2 \int_0^1 \psi_{eq}(x)x^4 dx}{J_{eq}}\end{aligned}$	$\dfrac{3}{2}q_m^2 \dfrac{\Gamma\left(\frac{b}{2} + \frac{5}{2}\right)}{\Gamma\left(\frac{b}{2} + \frac{7}{2}\right)}$	See Fig.4.2	

Table 4.2: Pincus-locked model. Here $[h_{LL}] = [F][L]^{-1}$; $[h_{PL}] = [F][L]^{-3/2}$; $c = (\frac{h_{PL}}{h_{LL}}) * b^{5/4} = (\frac{h_{PL}}{h_{LL}}) \, b\sqrt{q_m} \sim b\sqrt{q_m}[L]^{-0.5}$

Model	$f(x)$ $(x \leq 1)$	$\phi = q_m \int_0^1 f(x)dx$	$\psi_{eq} = e^{\phi(x)/kT}$
Linear-locked	$h_{LL}Q$ $=$ $h_{LL}q_m x$	$\dfrac{h_{LL}q_m^{\,2}}{2}x^2$	$\begin{cases} \exp(\dfrac{-h_{LL}q_m^{\,2}}{2kT}x^2) = e^{-bx^2/2} & x \leq 1 \\[2mm] 0 & x \notin [0,1] \end{cases}$
Pincus-locked	$h_{PL}Q^{\frac{2}{3}}$ $=$ $h_{PL}(q_m x)^{\frac{2}{3}}$	$\dfrac{2h_{PL}q_m^{\,5/2}}{5}x^{5/2}$	$\begin{cases} \exp(\dfrac{-2h_{PL}q_m^{\,5/2}}{5kT}x^{5/2}) = e^{-2cx^{5/2}/5} & x \leq 1 \\[2mm] 0 & x \notin [0,1] \end{cases}$

Table 4.3: Theoretical prodiction of the r_e for Real chain vs. Ideal chain. Pincus-locked model value is close to that of the R44, which demonstrates the importance of the non-linear initial region on the q_m dependence of the equilibrium properties.

Model	FENE	R44	Linear-locked	Pincus-locked
$\dfrac{h}{kT}\dfrac{q_m^2 \int_0^1 \psi_{eq}(x)x^4 dx}{J_{eq}/(4\pi q_m^3)}$	$\dfrac{3}{2}q_m^2\dfrac{\Gamma\left(\frac{b}{2}+\frac{5}{2}\right)}{\Gamma\left(\frac{b}{2}+\frac{7}{2}\right)}$	Num.	$b\left(\dfrac{3}{b} - \dfrac{\sqrt{2b}}{\sqrt{\pi}e^{b/2}\operatorname{erf}\left(\sqrt{b/2}\right)-\sqrt{2b}}\right)$	$b\dfrac{-5ce^{-c}+5\left(1-e^{-c}\right)}{c^{4/5}\left(-5\sqrt[5]{c}e^{-c}-\Gamma\left(\frac{1}{5},c\right)+\Gamma\left(\frac{1}{5}\right)\right)}$
$\dfrac{h}{kT}\langle Q.Q\rangle_{b=500}$	2.97	2.55	3.00 for any $b \geq 18$	2.27 using $c = b^{5/4}$

RPY tensor, and the effect of variation of the HI strength is studied by adjusting the non-dimensionlized hydrodynamic radius (a_h).

The extrapolation of both η_1 and ψ_1 to zero shear rates, for the FENE force law, agrees perfectly with the theoretical prediction for the FENE elastic dumbbells (Fig. 4.3a and 4.3b). Similarly in case of R44, when b is rescaled with $b^{0.55}$ similar relationships relate b with extrapolated zero-shear rate properties. Furthermore, in agreement with the bead-rod model, R44 demonstrates a slower shear thinning region at small shear rates, irrespective of the b value for both n_s. However both FENE and R44 reach an asymptotic shear thinning exponent at higher shear rates, shown with the solid line in Fig. 4.3d and collapse of data points at $Pe > 10$ in Fig. 4.3a and 4.3b, which corresponds to the screening of the EV interactions. The weak shear-thinning behavior observed at small Pe for the FENE force law is the consequence of small finite extensibility (b) and disappears rapidly as b is increased to 5000 when

compared to the second shear-thinning regime. However, for the R44 force law, shear thinning remains pronounced even at higher b values compared to the second regime of shear thinning (Fig. 4.5). Comparing Fig. 4.4b with Fig. 4.3b also demonstrates that the shear thinning exponent for ψ_{11} of FENE force law (≈ -1) drops rapidly by increasing b (-0.16 for $b = 5000$), i.e., the shear-thinning behavior is primarily due to finite extensibility, while for the R44 force law the drop with increasing b (from ≈ -0.66 to -0.37 for $Pe < 10$) is drastically lower, hinting to the fact that the nonlinear F-X behavior has a greater contribution to the shear-thinning behavior and thus this behavior is preserved for low Pe even at higher b values.

Pincus (1976) analysis of flexible chains with $f \sim x^{2/3}$ F-X regime under high velocity gradients, concludes that the nonlinear stress-strain relationship forces the transition into stretched state to higher shear rates and suppresses the separation between first-order and second-order transition. Neither of these phenomena is observed for FENE models that incorporate the EV interaction (Cifre and de la Torre, 1999) or predicted slight decrease in the transition Pe in extensional flows (Pham et al., 2008).In fact, the linear Hookian F-X relationship at the small extension region ($x < 0.35$) embedded within the spring force law of the FENE chain ensembles, dominates the elastic behavior of the polymer model even after incorporation of the EV. Therefore, the inability of the FENE based BDSP to accurately capture the behavior of flexile chain with excluded volume is expected. On the other hand, the R44 force law carries over the non-linear region to the next coarse-grained model and therefore, it is expected to show reasonable agreement with Pincus's predictions. The reduction of the slope of transition between coil states and stretched state is demonstrated in Fig. 4.6 for uniaxial elongation flow, and Fig. 4.7a in case of the shear flow. In both cases, uniaxial elongation and shear flows, the slope of transition decreases in the case of R44 force law, i.e., the fist order transition is dampened and approaches a smooth second order transition. The probability distribution of the mean square end-to-end distance (Fig. 4.5) reveals formation of a stronger peak
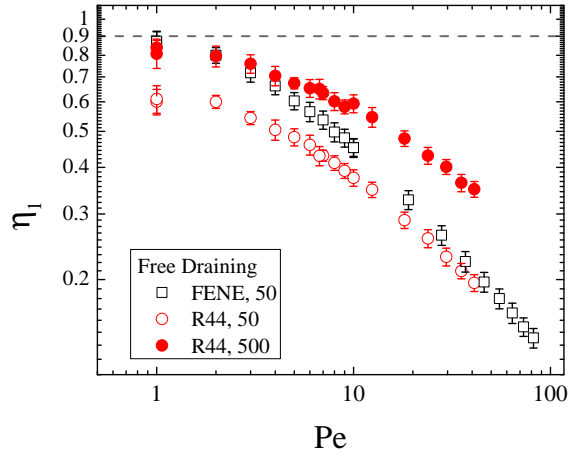
(a) Dumbbell
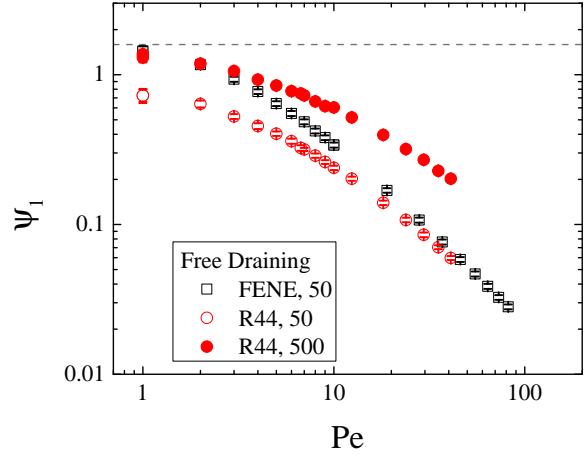
(b) Dumbbell
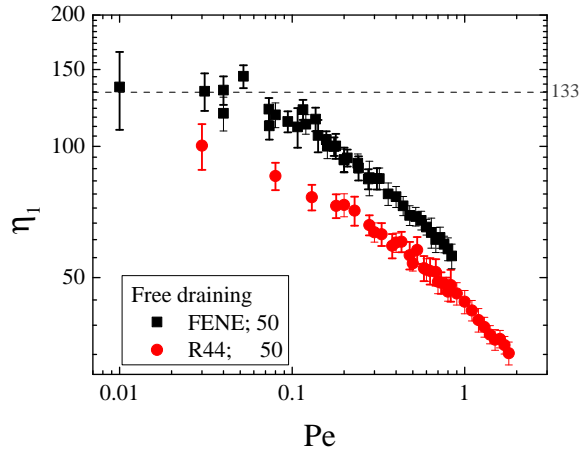
(c) $n_s = 20$
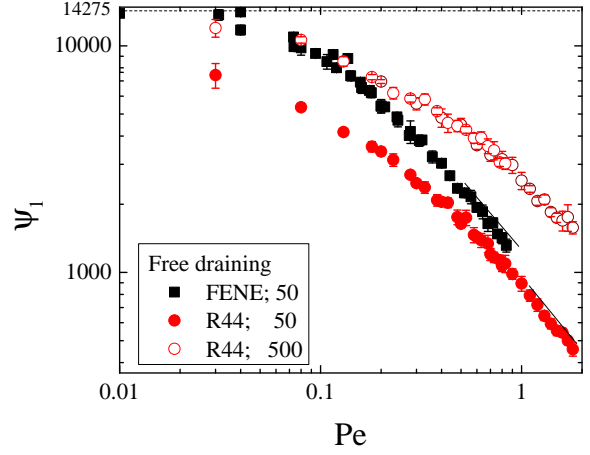
(d) $n_s = 20$

Figure 4.3: Comparison of shear viscosity and first normal stress coefficient. The dashed line on all graphs is the theoretical value obtained for the corresponding Rouse chain (for FENE dumbbell $\eta = \frac{b}{b+5}$ and $\psi = \frac{2b^2}{(b+5)(b+7)}$)
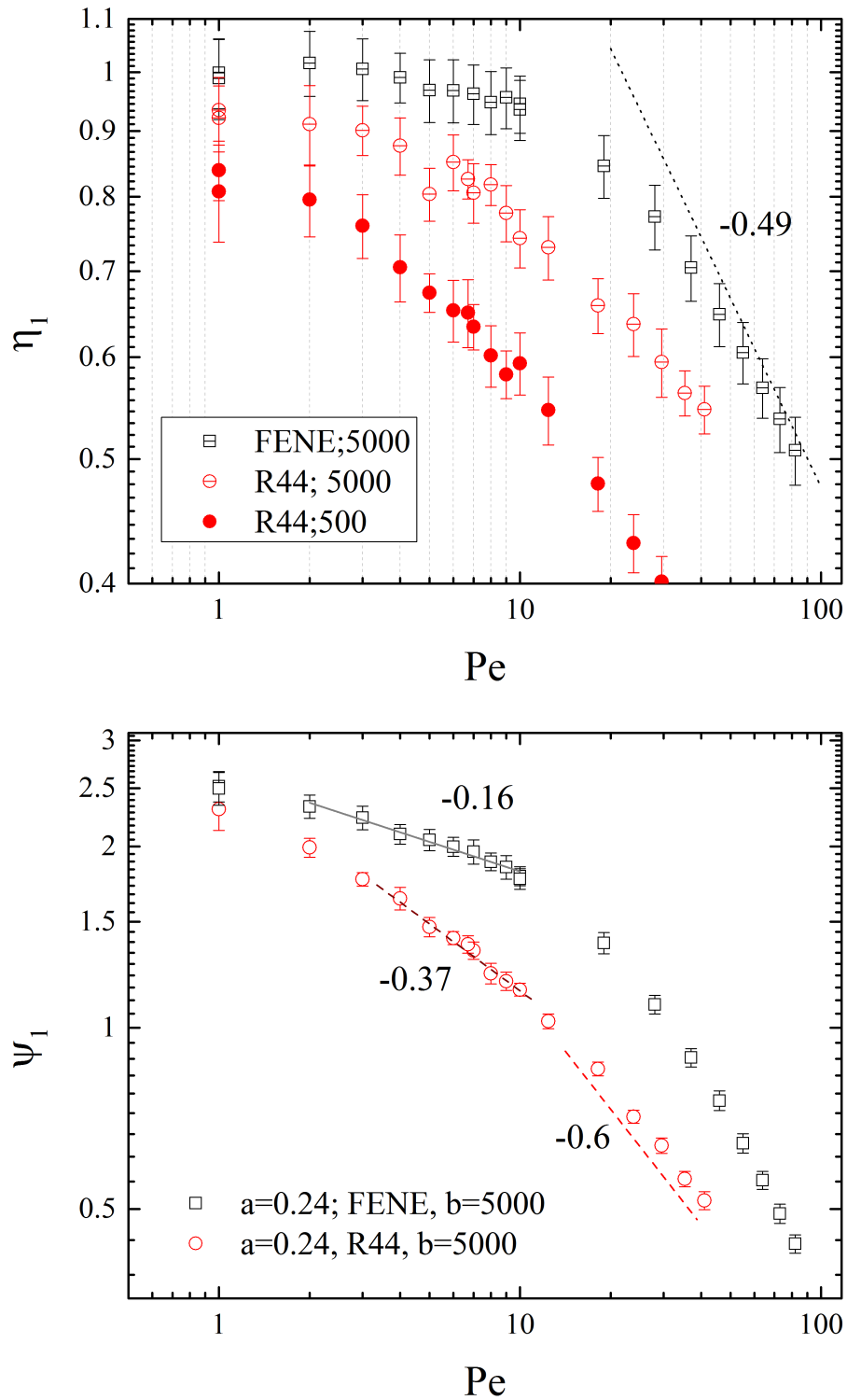
Figure 4.4: Comparison of the shear viscosity (top) and the first normal stress coefficient (bottom) for long chains modeled as dumbbells.
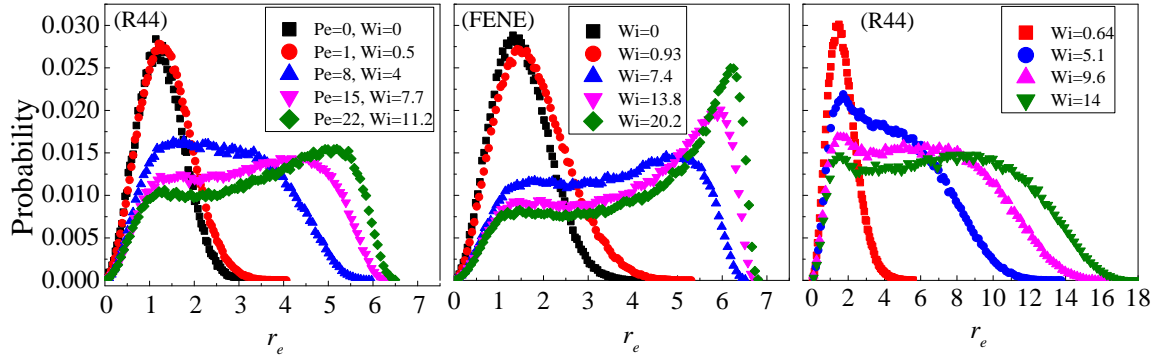
(a) Dumbbell
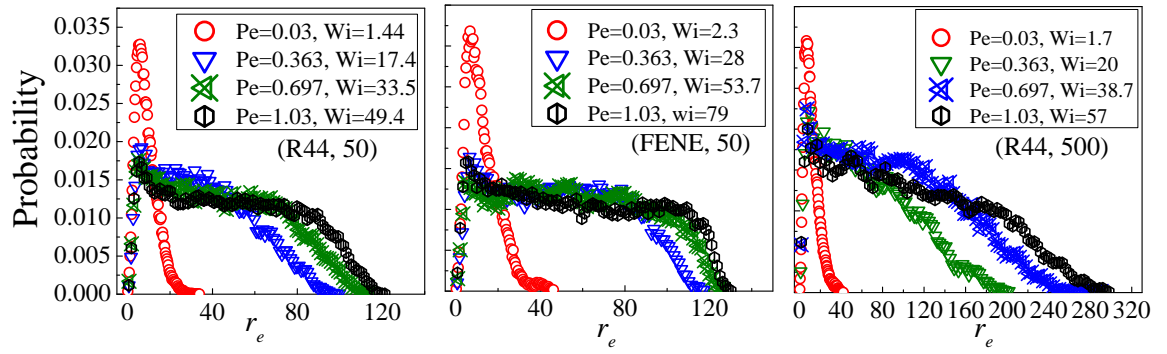
(b) Bead-spring $n = 21$

Figure 4.5: Comparison of the probability distribution of the end-to-end distance of dumbbells (top) and bead-spring chain with $n = 21$ in shear flow. The middle plots correspond to the FENE with $b = 50$ model, while the left and right are based on the R44 force law with $b = 50$ and $b = 500$, respectively.
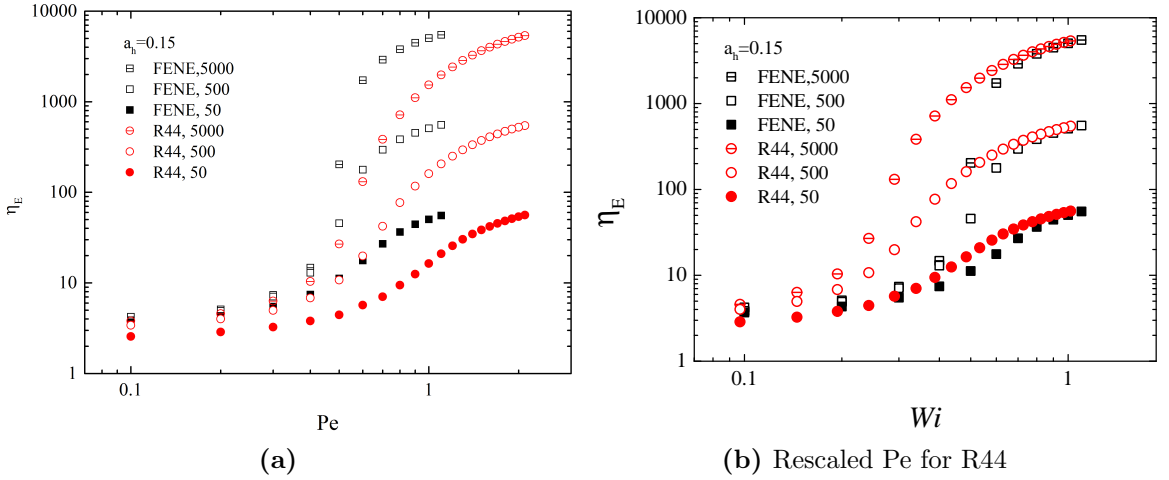
Figure 4.6: Polymer contribution to the elongational viscosity obtained from dumbbell subjected to the uniaxial flow. a_h has minimal effects in case of dumbbells and can be ignored. In the limit of large elongation $\eta_E \sim 2b$ for both force laws and near equilibrium $\eta_E \approx 3$ for the FENE force law in agreement with the theoretical predictions. a_h is the hydrodynamic radius of the bead.

at low extension for the R44 force law, and slower diffusion of the phase-space into highly extended chains.

The effect of HI on the C-S transition is investigated for $n_s = 20$. Increasing the hydrodynamic radius in both types of springs decreases the C-S transition pace with increasing Pe and slightly increases the onset of transition, which is expected since HI decreases the longest relaxation time of the chain if critical Wi is supposed to remain at 0.5, as observed in the BDRD simulation of chapter 5. However, HI affects the R44 chain less in comparison with the FENE chains as shown in Fig. 4.8.

4.4   Summary

In summary, the R44 force law for real chain, which was developed from the fine-grained bead-rod model, was compared with the FENE force law both for the elastic dumbbell model and the bead-spring model. In order to isolate the effect of initial non-linear region where $f \sim x^{2/3}$ the Pincus-locked model was introduced and compared
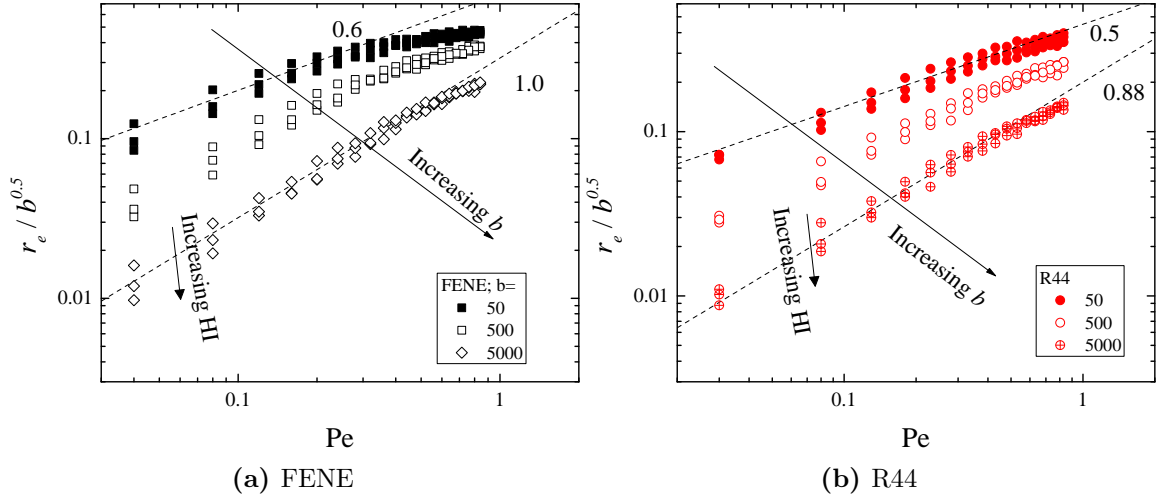
Figure 4.7: Comparison of steady state chain extension in shear flow between FENE and R44 dumbbell. The HI for each b HI parameter increases from the free draining case (no HI) to $a_h = 0.15$ and $a_h = 0.24$.

with the linear-locked model via analytical calculation of probability distribution function. Moreover, the BDSP analysis revealed that the nonlinear F-X of the R44 force law induces higher shear thinning at mid range of Wi. Furthermore, in agreement with Pincus's theory, the implicit EV incorporation via the R44 force law tends to decrease the slope of coil to stretch transition in uniaxial and shear flow, which was not observed in models with the FENE springs with EV potential between beads.
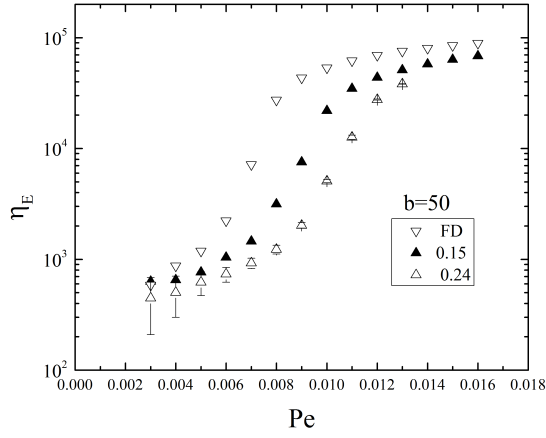
(a) FENE, $b = 50$
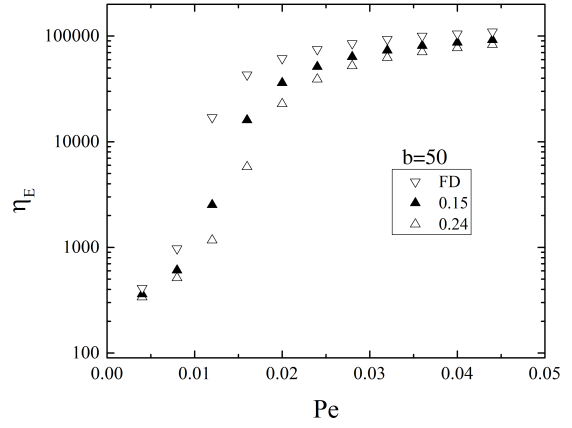
(b) R44, $b = 50$
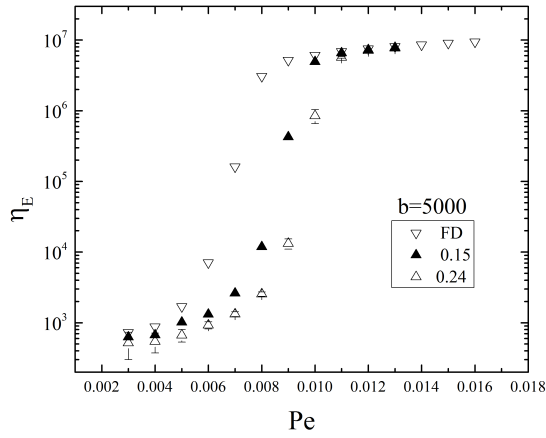
(c) FENE, $b = 5000$
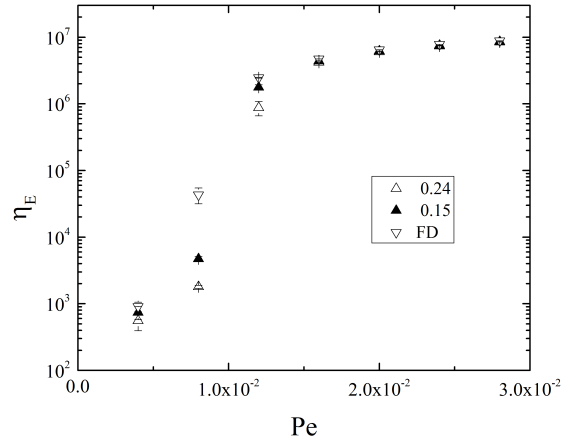
(d) R44, $b = 5000$
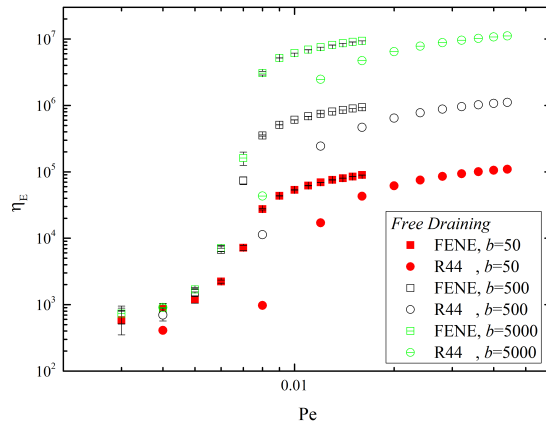
(e) FENE and R44, all bs, FD
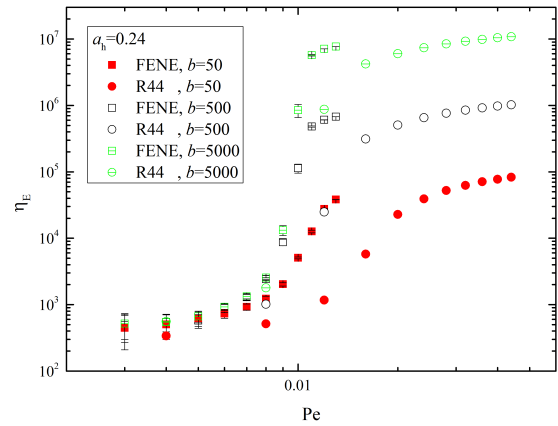
(f) FENE and R44, all bs, with HI and EV

Figure 4.8: HI effect on the C-S transition for $n = 20$. The error bars are shown only for $a_h = 0.24$ for the sake of clarity, other data points have similar error bars at same Pe.

67

Chapter 5

A NOVEL ALGORITHM FOR BROWNIAN DYNAMICS SIMULATION OF LONG FLEXIBLE MACROMOLECULES MODELED AS BEAD-ROD CHAINS

The computational efficiency of Brownian Dynamics (BD) of the constrained model of the polymeric chain (bead-rod) with n beads is reduced to the order of n^2. Moreover, the Barnes and Hut multipole method is employed to calculate the HI effect in order to further reduce the computational scaling, and its feasibility in BD of polymeric solutions is discussed. Furthermore, a new stress algorithm is developed which accurately captures the transient stress growth in the start-up of the flow for the bead-rod model with HI and excluded volume for the first time. Rheological properties of the chains up to $n = 350$ in the presence of excluded volume and

hydrodynamic interaction is discussed, utilizing the former algorithm which depicts qualitative difference in shear thinning behavior compared to ideal chains with HI in the mid range of the Weissenburg number (Wi).

5.1   Introduction

Molecular models with constraints are the backbone of various computational efforts aimed to investigate the dynamics of the individual or assembly of macromolecules, therefore any improvement in simulation techniques will consequently impact closely related problems with holonomic constraints in classical molecular dynamic (Ryckaert et al., 1977; Miyamoto and Kollman, 1992), quantum chemistry (Echenique et al., 2006) and econophysics (Schulz, 2003; Janovà, 2011). Since consideration of macromolecules as a chain of uncorrelated segments by Kuhn, several constrained models of polymeric chain such as freely jointed and freely rotating chains have been introduced, which successfully predict equilibrium and non-equilibrium properties of macromolecules via retarded motion expansion and variational methods. These findings have in turn facilitated development of coarse-grained bead-spring models and eventually connect the continuum constitutive equations of polymeric fluids to the underlying micromechanical model via kinetic theory (Bird et al., 1996).

While theoretical treatment of dynamics of constrained macromolecular models, mainly in generalized coordinates, is limited to a few rigid segments ($n < 4$) or small Peclet numbers(Pe) (Kramers, 1946; Kirkwood and Riseman, 1948; Hassager, 1974), development of robust integration techniques (Öttinger, 1994) for stochastic differential equations along with the steady improvement of computational resources allow dynamic simulation of constrained models of longer, or equivalently more flexible, chains with hydrodynamic interaction (HI) and excluded volume (EV) via BD simulation. Meanwhile, single polymer techniques have provided tools to investigate and perturb semi-flexible chain (e.g. Smith et al., 1992b) , and recently flexible chain (Saleh et al., 2009; Marciel and Schroeder, 2013), at the molecular level, which further

motivates development of efficient computational methods, in order to extend current algorithm capable of modeling of about 150-200 statistical segments suitable for semi-flexible chains (e.g λ-DNA), into models with about a thousand beads for flexible macromolecules such as single stranded DNA.

Temporal evolution of bead-spring chains can be performed via the well-known sweeping or semi-implicit algorithms; however, in bead-rod model, in order to impose the constraint equations, the set of Lagrangian multipliers must be found via solution of a non-linear set of equations. For free draining chains, no HI, this is typically done via well known Picard or Newton-Raphson methods (Somasi et al., 2002), through formation of a tri-diagonal coefficient matrix. Since the computational cost scales with $O(n)$, for n beads, the only obstacle is the inherent longest relaxation time of the polymeric chain which scales with $O(n^{\approx 2})$ and this translate to a $O(n^3)$ scaling in computational cost as degree of polymerization increases. The combination of various parallelization techniques in order to reach the limit of 1000 beads, similar to the path taken in Chapter 3, alleviates this high computational demand. However, in the presence of HI the aforementioned coefficient matrix is dense , and in order to take advantage of the multipole or Conjugate-gradient (CG) methods, it has to be rewritten as an operation between a set of known vectors rather than matrix-vector products, which immediately rules out any second order method such as Newton-Raphson. In order to remove this obstacle, an iterative conjugate gradient method based on Krylov subspace is embedded within the Picard method iteration in the algorithm presented below; this combination significantly improves performance of BD simulation of bear-rod model and reduces the scaling exponent from 3 to about the scaling of estimation of the matrix-vector product, i.e, 2.

Irrespective of the computational platform (GPU, CPU, shared or distributed memory paradigms), the inherent $O(n^3)$ cost of Cholesky decomposition required in the BD simulation to find the correct weighting matrix of the random forces from diffusion tensor, is the major obstacle to reducing the computational scaling exponent in the presence of HI. Several techniques have been introduced, in order

to effectively reduce the computational cost to $O(n^{2.25})$ for long chains (Jendrejack et al., 2000; Schmidt et al., 2011; Ando et al., 2012) which acts as the new bottleneck for systems with no constraints, along with $O(n(n-1)/2)$ operations of formation of the HI tensor. Recently using fast multipole method , FMM, (Liang et al., 2013) developed an algorithm to drop the cost of this former step to $O(n \log n)$. Here we have introduced $O(n \log n)$ operation using the Barnes and Hut (B&H) method (Barnes and Hut, 1986) for mobility matrix formation. The B&H method is preferred to the FMM in this case since it can be modified to ensure fulfillment of Newton's third law of motion (Dehnen, 2000), which ensures accurate scaling of diffusion and other dynamic properties. The correlation tensor is then constructed via Krylov subspace method Ando et al. (2012), which removes the second bottleneck.

The first major contribution of this work is the development of an algorithm that reduces the computational cost of BD. Specifically, as far as non-zero elements of the normal contra-variant tensor remain near diagonal and count as order of $n \log n$, a criterion imposed by metric force calculation, dynamics of the polymeric chain with long range hydrodynamic interaction is effectively evolved as $O(n^{2.125})$ or $O(n^{1.25})$ scheme with the algorithm developed in this research. The former, which is significantly faster than the direct method of matrix inversion, is achieved by combining the Picard method with the Conjugate Gradient (CG) method. The near linear scaling utilizes the Barnes and Hut multipole method for the HI calculation bottleneck. The second contribution of this work is the implementation of a new algorithm capable of dividing the stress into contribution from each force, with accurate prediction of the transient region within the framework set up by Morse (2004). Moreover, the above techniques are utilized in order to examine the non-equilibrium behavior (diffusion ,shear and extensional flow) of polymeric solutions with HI and EV. Considering the importance of the number of segments on F-X behavior in presence of the EV interaction, the results from the present work are compared with the previous attempts, which as discussed below were conducted with fewer segments and discussion on the transient stress behavior for the system with HI

71

is absent. (Details of accurate incorporation of EV and the effect of n on the chain F-X in presence of EV are already discussed in chapter 3.)

It has been shown that translational diffusivity scales as $\sim n^{-0.579}$ (Rey et al., 1992) in good agreement with other simulation and the experimental observations, $D \sim n_b^{-0.55 < \gamma < -0.68}$, as discussed in the next section. Petera and Muthukumar (1999) have explored the steady state material functions of BDRD model with HI and EV for small chains ($n < 20$) under shear flow. Their results depict that HI has three effects on the shear properties. First, shear thinning disappears at smaller Wi in presence of the HI. Second, HI lowers the viscosity at small shear rates. Third, the first normal stress coefficient (ψ_1) of systems with HI and EV is smaller than the FD chain at low shear rate and larger after a transition shear rates, i.e., the power law scaling exponent with shear rate is smaller. Utilizing the same BDRD method, Liu et al. (2004) studied the chain in elongation flow and found that at the coil-stretch transition $\dot{e}_c \sim n^{-\alpha}$, for $n \leq 60$ and $\alpha = 1.4$ compared to the experimental prediction, i.e., 1.5, irrespective of the solvent quality. Neelov et al. (2002) found the scaling exponent as $\alpha = 1.96$ with HI ($n < 100$) and 1.55 for the FD case. Sim et al. (2007) employed BDRD model to investigate scission due to segmental tensions ($n < 150$) and showed that $\dot{e}_c \sim n^{-2}$ with no HI and $\dot{e}_c \sim n^{-1.7}$ with HI. HI effectively shields the inner beads from bulk flow and increases the time required for coil-stretch transition at $\dot{e}_c$ (Agarwal et al., 1998). In the result and discussion section, both shear thinning and coil stretch transition are discussed for the chain with HI and EV for $n = 350$.

Dalal et al. (2012) investigated tumbling dynamics utilizing bead-spring with the stiff Frankeal springs in Θ-solvent. Via comparison between the stiff Frankel springs with united atom polystyrene chains, Dalal et al. (2012) concluded that explicit solvent molecules and side chains are required to capture the single mode relaxation behavior of short polymeric chains. It is known that stiff spring does not produce the same probability distribution as that of the constrained chains, and away from equilibrium, the spring modulus should be adjusted based on the Peclet number Pe

(Dalal et al., 2012). Moreover, stress tensor of stiff chain cannot be found accurately since the contribution of bond spring to the momentum transfer arbitrarily changes with the highly stiff spring modulus.

5.2 Theory of constrained Brownian motion

5.2.1 Problem formulation

The contour length of the polymeric chain (l) is divided into n_s segments with fixed length (l_o) representing the equilibrium Kuhn length of free rotating chains with no intramolecular interactions. Mathematically, the fixed Kuhn length can be shown as a set of n_s constraints: $C(\{R\}) = |R_{\nu,\nu+1}| - 1 = 0$ where $R_{\mu,\nu} \equiv R_\mu - R_\nu$ and R_i is the position vector of bead i. The phase-space trajectory evolution of $2n_s - 1$ degrees of freedom of such chain can be expressed via a stochastic differential equation subject to a set of constraints for the Kuhn length:

$$\Delta R/dt = \mathrm{P} \cdot (V^s + \kappa \cdot R + \mathrm{Y} \cdot F) + kT \frac{\partial}{\partial R} \cdot (\mathrm{P} \cdot \mathrm{Y} \cdot \mathrm{P}) \tag{5.1}$$

where P is the dynamical projection tensor and Y is the Rotne-Prager-Yamakawa (RPY) hydrodynamic interaction tensor. R is the vector of $3n_b$ bead positions subjected to the solvent flow field with the velocity gradient (3×3 block diagonal) tensor of rank $3n_s$, $\bar{\bar{\kappa}}$, and uniform velocity V^s at the bead center. Vector F in Eq. 5.1 is the sum of the random force, metric force and the conservative force resulting from the inter-bead potential.

Random force is constructed as $F^{(r)} = \sqrt{2/dt}\zeta \cdot \mathrm{B} \cdot W$, where ζ is the Cartesian friction tensor, W is the vector of random numbers with variance of one and mean of zero, and B is found via Krylov subspace method (Ando et al., 2012) such that Y=B·B. The metric force is defined as $F^{(m)} = \frac{kT}{2} \frac{\partial}{\partial R} \ln \left[\det \left(\hat{\mathrm{G}} \right) \right]$, where $\hat{\mathrm{G}} = \frac{1}{m} \mathrm{N} \cdot \mathrm{N}^\dagger$ and $\mathrm{N}_\mu^i = \frac{\partial c^i}{\partial R^\mu}$ is the vector normal to the constraint surface. Calculation of the

metric force is facilitated using the following identity: $F^{(m)} = \frac{kT}{2} \frac{\partial}{\partial R} \ln \left[\det \left(\hat{G} \right) \right] = \frac{kT}{2} \hat{G}^{-1} : \frac{\partial \hat{G}}{\partial R}$ and which allows utilization of the bidiagonal format of N(See Appendix A). Finally, the inter-bead potential is limited to the hard sphere potential, hence the conservative force will be $F^{(hs)} = \frac{\partial}{\partial R} \phi(R_{\nu\mu})$ where $\phi(r) = 4\epsilon \left[\left(\frac{\sigma}{r} \right)^{12} - \left(\frac{\sigma}{r} \right)^{6} \right]$ for $r < 2^{(1/6)}\sigma$ and zero otherwise.

5.2.2   Numerical evolution algorithm

It is not necessary to form the projection matrix in Eq.5.1 explicitly; instead, a two step algorithm with an Ito unconstrained move followed by a Stratonovich corrector step will reproduce the SDE in Eq.5.1. The Predictor step evolves the bead position vector $(R(t))$ to $\tilde{R}$, with the velocity equal to that of the terms inside the parenthesis in the first term of the right hand side of Eq.5.1, with all the configurationally dependent terms calculated at time t. The costly part is the determination of the Lagrange multipliers from the following set of non-linear coupled equations:

$$\left[R^*_{\mu+1} + Y_{\mu+1} \cdot F^{(c)} \delta t - R^*_\mu - Y_\mu \cdot F^{(c)} \delta t \right]^2 = 1 \quad (0 < i < n) \tag{5.2}$$

which keep the trajectory path in the space bounded by the constraints. Both Y and N terms are calculated at $R^* = \left(R(t) + \tilde{R} \right) / 2$, so that $R(t + dt) = \tilde{R} + Y \cdot N \cdot \Lambda = \tilde{R} + F^{(c)} dt$, where Λ is the vector of the $n_s = n - 1$ Lagrange multipliers, and in the right hand side expression $F^{(c)}$ is interpreted as the constrained force. The new numerical iteration scheme reduces the computational cost of this step to the order of calculation the RPY kernel (see 5.4) on the force vector, instead of the typical $O(n^3)$ scaling required to solve the dense n_s non-linear system of equation that arises from the constraint enforcement at the corrector step. While utilizing the straight forward diffusion matrix formation and performing the $Y \cdot F$ matrix-vector multiplication will result in an $O(n_s^{\approx 2})$ algorithm, flexibility of the new numerical algorithm allows for incorporation of multipole methods. Specifically, the B&H tree

method can be exploited as described in the next section to achieve the theoretical $n \log(n)$ scaling. However, it is demonstrated that this approach reduces the bead-rod simulation algorithm to $O(n^{\approx 1.25})$ as opposed to $n \log(n)$.

Definition of the following vectors and matrices will facilitate the discussion:

$$U_i = R_{\mu+1} - R_\mu$$

$$\tilde{U}_i = \tilde{R}_{\mu+1} - \tilde{R}_\mu$$

$$\mathrm{U} \equiv \begin{bmatrix} U_1 & o & o & o \\ -U_1 & U_2 & o & o \\ o & -U_2 & \dots & U_{n_b-1} \\ o & o & o & -U_{n_b-1} \end{bmatrix} \text{, bidiagonal matrix } (3n \times n_s)$$

$$\tilde{\mathrm{U}} \equiv \begin{bmatrix} \tilde{U}_1^\dagger & & \\ & \ddots & \\ & & \tilde{U}_{n_k}^\dagger \end{bmatrix} \text{, diagonal matrix } (3n \times n_s)$$

$$
\text{S: Grand Rouse matrix } (3n_s \times 3n_b) =
\begin{bmatrix}
-\iota & \iota & o & o & o \\
o & -\iota & \iota & o & o \\
o & o & \ddots & \ddots & o \\
o & o & o & -\iota & \iota
\end{bmatrix}
, \; \iota \equiv
\begin{bmatrix}
1 & 0 & 0 \\
0 & 1 & 0 \\
0 & 0 & 1
\end{bmatrix}
$$

So the coupled system of equations to determine Λ vector for the segment i is found from the following:

$$
\left[\left(\tilde{U} + S \cdot Y \cdot S^\dagger \cdot U \cdot \Lambda \right)_{i,i} \right]^2 = 1
$$

$$
2 \left(\tilde{U} \cdot S \cdot Y \cdot S^\dagger \cdot U \cdot \Lambda \right)_{i,i} = 1 - \left(S \cdot Y \cdot S^\dagger \cdot U \cdot \Lambda \right)_{i,i} \left(S \cdot Y \cdot S^\dagger \cdot U \cdot \Lambda \right)_{i,i} - \tilde{U}_{i,i} \tilde{U}_{i,i} \quad (5.3)
$$

The solution algorithm is summarized in algorithm 1.

Algorithm 1 Picard+CG corrector step algorithm -Part 1

1: $ite \leftarrow 0$
2: **repeat**
3:      $ite \leftarrow ite + 1$
4:      $V \leftarrow Y \cdot \left(S^\dagger \cdot U \cdot \Lambda^{(t)} \right)$ % can be performed via B&H or direct method
5:      $W \leftarrow S \cdot V$
6:      **for** $0 < i < n$ **do**
7:          $V_i^{(2)} \leftarrow W_i . W_i$
8:      **end for**
9:      **for** $0 < i < n$ **do**
10:         $E_i \leftarrow \left(1 - V_i^{(2)} - \tilde{U}_i^2 \right) / 2$ % Calculating the RHS of Eq. 5.3
11:      **end for**

Next part is mainly the CG solution of the linear system $\left(\tilde{U} \cdot S \cdot Y \cdot S^{\dagger} \cdot U \right)$, which allows utilization of the suitable routine (direct or B&H) method for matrix-vector multiplications.

Algorithm 2 Part 2: Solution of $A \cdot X^{(ite)} = E$ trough CG

12: $\quad X^{(0)} \leftarrow \Lambda^{(t)}$

13: $\quad i \leftarrow 0$

14: $\quad$**repeat**

15: $\qquad J \leftarrow E - A \cdot X^{(0)}$

16: $\qquad E^{(0)} \leftarrow J$

17: $\qquad Z \leftarrow A \cdot V \qquad\qquad$ % B&H or direct

18: $\qquad \alpha \leftarrow \dfrac{V^{\dagger} \cdot V}{V^{\dagger} \cdot Z}$

19: $\qquad E^{(i+1)} \leftarrow E^{(i)} - \alpha Z$

20: $\qquad \beta \leftarrow \dfrac{E^{(i+1)} \cdot E^{(i+1)}}{E^{(i)} \cdot E^{(i)}}$

21: $\qquad V = E^{(i+1)-\beta V}$

22: $\qquad X^{(i+1)} \leftarrow X^{(i)} + \alpha V$

23: $\qquad i \leftarrow i + 1$

24: $\quad$**until** $alpha|V| < tolerance$

25: $\quad \Lambda^{(t)} \leftarrow X^{(i)}$

26: **until** $\left| \Lambda^{(t)} - \Lambda^{(ref)} \right| > tolerance_{picard}$

27: $R^{t+dt} \leftarrow \tilde{R} + Y \cdot U \cdot \Lambda$

5.2.3 Application of the Barnes and Hut method in constrained BD

For the bead-rod model of linear chain, the 3×3 blocks of the RPY HI tensor, nondimensionalized with kT/ζ, can be written as (a is the hydrodynamic radius in

this chapter):

$$\Omega_{ij} = \begin{cases} \frac{3a}{4|R_{ij}|} \left[\left(1 + \frac{2a^2}{3|R_{ij}|^2}\right) \iota + \left(1 - \frac{2a^2}{|R_{ij}|^2}\right) \frac{R_{ij}R_{ij}}{|R_{ij}|^2} \right] & |R_{ij}| \geq 2a \\ \\ \left[\left(1 - \frac{9|R_{ij}|}{32a}\right) \iota + \left(\frac{3}{32a|R_{ij}|}\right) R_{ij}R_{ij} \right] & |R_{ij}| < 2a \end{cases} \quad (5.4)$$

The matrix-vector kernel is then:

$$V = \Omega \cdot F$$

In the above V is the perturbation velocity due to HI, Ω is hydrodynamic tensor and F is the force vector on the particles creating the velocity perturbation (source particles). The above equation can be rewritten for the RPY matrix at distances greater than the bead diameter ($\alpha \in \{x, y, z\}$ and $\mathrm{r}_{ij} \equiv |R_{ij}|$):

$$V_{\alpha,i} = \sum_{j \neq i} \left(c_1 \frac{1}{\mathrm{r}_{ij}} F_{j,\alpha} + c_2 \frac{1}{\mathrm{r}_{ij}^3} F_{j,\alpha} + c_1 \frac{R_{ij,\alpha}(R_{ij} \cdot F_j)}{\mathrm{r}_{ij}^3} - c_2 \frac{3R_{ij,\alpha}(R_{ij} \cdot F_j)}{\mathrm{r}_{ij}^5} \right)$$

with $c_1 \equiv 3a/4$ and $c_2 \equiv a^3/2$ .Substituting R_{ij} in the above equation:

$$V_{\alpha,i} = \sum_{j \neq i} \left(c_1 \frac{1}{\mathrm{r}_{ij}} F_{j,\alpha} + c_2 \frac{1}{\mathrm{r}_{ij}^3} F_{j,\alpha} + c_1 \frac{(R_i - R_j)_\gamma R_{ij,\alpha} F_{j,\gamma}}{\mathrm{r}_{ij}^3} - c_2 \frac{3(R_i - R_j)_\gamma R_{ij,\alpha} F_{j,\gamma}}{\mathrm{r}_{ij}^5} \right)$$

$$V_{\alpha,i} = c_1 \sum_j \frac{1}{\mathrm{r}_{ij}} F_{j,\alpha} + c_2 \sum_j \frac{1}{\mathrm{r}_{ij}^3} F_{j,\alpha} - c_1 r_{i,\gamma} \sum_j \frac{d}{dr_\alpha} \left(\frac{F_{j,\gamma}}{\mathrm{r}_{ij}} \right) + c_2 r_{i,\gamma} \sum_j \frac{d}{dr_\alpha} \left(\frac{F_{j,\gamma}}{\mathrm{r}_{ij}^3} \right)$$
$$+ c_1 \sum_j \frac{d}{dr_\alpha} \left(\frac{r_{j,\gamma} F_{j,\gamma}}{\mathrm{r}_{ij}} \right) - c_2 \sum_j \frac{d}{dr_\alpha} \left(\frac{r_{j,\gamma} F_{j,\gamma}}{\mathrm{r}_{ij}^3} \right)$$

$$V_{\alpha,i} = c_1 \phi_{1/r,\alpha,i} + c_2 \phi_{1/r^3,\alpha,i} - c_1 \psi_{1/r,\alpha,i} + c_2 \psi_{1/r^3,\alpha,i} + c_1 \chi_{1/r,\alpha,i} - c_2 \chi_{1/r^3,\alpha,i} \quad (5.5)$$

The above equation defines $\phi(F, R)$, $\psi(F, R)$ and $\chi(F, R)$. Both ϕ and ψ can be constructed from the same multipole moments and sources, therefore reducing the overhead significantly as demonstrated below. The χ terms also share the same

multipole moments, so they are efficiently merged into a united tree formation (built up) and force calculation routine.

Consider the above potential at $R_{ij} = R_i - R_j = R_i - R_{c,m} + (R_{c,m} - R_j)$, where $R_{c,m}$ is center of force of m particles:

$$R_{ij} = R_{i,c} + \delta R_{c,m}$$

$$R = \bar{R}_{i,c} \equiv R_i - R_{c,m}$$

$$\delta R = \delta R_{c,j} \equiv (R_{c,m} - R_j)$$

Note R is only function of the jth particle position and not each individual source particle hence it can be factored out of the sum. From the Taylor expansion of the kernel,

$$f_{\alpha,i}(R + \delta R) = \sum_j^N \left[f_{\alpha,i}(R) + \frac{\partial f_{\alpha,i}(r_i)}{\partial r_i}\Big|_R \cdot \delta R_{c,j} + \frac{1}{2}\delta R \cdot \frac{\partial^2 f_{\alpha,i}(r_i)}{\partial r_i \partial r_i}\Big|_R \cdot \delta R_{c,j} \right]$$

, each term on the RHS of Eq. 5.5 is found (Appendix A.II).

Barnes and Hut method in BDRD: summary of implementation

The classical implementation of the B&H method starts by hierarchical division of the simulation box space (tree) into sub-spaces (tree branches) until every source point is assigned to one and only one sub-space (leaf). In 2-dimension for instance, the first division of the two dimensional box-square leads to four squares with sides half the size of the original square (quad-trees), which each in turn is divided into 4 smaller squares. Each branch has a center of force and the center of force of the leaves is indeed the position vector of the bead. If certain condition is met, the HI between the cluster of charges in a sub-space will not sum over every individual particle in the sub-space, but through indirectly through the multipole components of that specific box. The aforementioned condition is determined by a preset value θ: for each particle i

and box with center of force r_{cm} and side size of l_{box} if $\theta < \dfrac{l_{box}}{r_{i,cm}}$ then the multipole effects are considered, otherwise one should move one level down the tree and consider the branches (children) of the original box. In the case of HI in BDRD, consideration of four unique observations in the code results in significant enhancement in the computational efficiency. One since in the corrector step bead positions are not changed, subsequent Picard iterations are not required to update the tree. Two, considering the number of flops required to estimate RHS of Eq 5.5 for any branch with less than 3 beads regardless of whether θ HI effect is calculated directly from each bead. Three, the direct interactions amongst all bead pairs can be summarized in the grand sparse mobility tensor of rank $3n$, which is also unchanged during the corrector step. Four the indirect multipole interactions are also summarized in a tensorial format, which should be recalculated in each iteration. This is the most time consuming sub-algorithm of the B&H method for HI in BDRD simulation; future efforts should especially target higher efficiency of this section.

5.2.4 Stress calculation

While formulation of stress tensor in terms of force vector and conformation tensor is readily available for both free draining and polymer solution with HI (Bird et al., 1996; Öttinger, 1994, 1996), the existing algorithms for estimation of the transient stress tensor in polymeric systems with constrains from stochastic modeling is limited to the case with no HI (Sim et al., 2007). These algorithms discuss the various methods of noise reduction either via Stratonovich, with separation of Brownian and viscous contribution, (Doyle et al., 1997) or Ito formulations (Schieber and Obasanjo, 2005). The exception are the works discussed in the previous section that have successfully applied the formulation due to Öttinger to approximate the steady state stresses, but does not include the transient data or implement a noise reduction technique. There are no established algorithms that provides transient stress tensor for BDRD (Sim et al., 2007) due to relatively large error caused by the stochastic force, especially in

small Wi. Consequently, transient stress for the bead-rod micro-mechanical model is not reported in the literature for any flow kinematics. A summary of stress algorithms can be found in the excellent review by Morse (2004). It should be noted that while small statistical error for limited number of trajectory (accuracy) and capturing all characteristics of transient stress evolution (fidelity) are major concerns in any stress calculation algorithm, computational cost is generally an unrelated concern since the cost of stress calculation is insignificant compared to the time integration cost, and therefore, will not be discussed here.

Our proposed algorithm decomposes the stress into deterministic and stochastic portions using the projection matrix; this also determines the contribution of each deterministic force such as metric force or potentials individually. Hence, in the transient regime, due to noise reduction, this method produces accurate results with limited number of trajectories.

Stress calculation: summary of implementation

In order to find the noise reduced stress, it is necessary to decompose the tensions (constraint forces) into the stochastic and deterministic parts. In the Öttinger algorithm the total drift velocity in terms of all forces is determined as:

$$dR/dt = \mathrm{Y} \cdot \left(F^{(r)} + F^{(f)} + F^{(\phi)} + F^{(e)} \right) + \tilde{\mathrm{Y}} \cdot \tilde{\mathrm{N}} \cdot \Lambda \qquad (5.6)$$

In the above equation $F^{(r)} = \sqrt{2/dt}\zeta \cdot \mathrm{B} \cdot W$, where ζ is the Cartesian friction tensor, $\mathrm{N} \equiv \nabla_r \mathrm{C}$ and W is the vector of random number with Gaussian distribution and standard deviation of dt, averaged at zero. All star (*) superscripted quantities refer to the values calculated at mid-step, consistent with the Stratonovich integration. The total drift velocity must occur adjacent to the hyper surface defined by the constraints:

$$\mathrm{N} \cdot \Delta R = 0 = \mathrm{N} \cdot \left[\mathrm{Y} \cdot \left(F^{(r)} + F^{(f)} + F^{(\phi)} + F^{(e)} \right) + \mathrm{Y}^* \cdot \mathrm{N}^{*\dagger} \cdot \Lambda \right] \qquad (5.7)$$

For a linear chain this condition clearly can be rewritten as $-2U_i \cdot dR_{i-1} + 2U_i . dR_i = 0$ with $U_i = R_i - R_{i-1}$. This in turn can be rewritten as $2U_i \cdot dU_i = dU_i^2 = 0$ or constant bond length if N is calculated at the end of time step. The tension values then will be

$$[\text{N} \cdot \text{Y}^* \cdot \text{N}^{*\dagger}]^{-1} \cdot \text{N} \cdot \text{Y} \cdot \left(F^{(r)} + F^{(f)} + F^{(\phi)} + F^{(e)}\right) = \Lambda = \Lambda^{(r)} + \Lambda^{(f)} + \Lambda^{(\phi)} + \Lambda^{(e)} \quad (5.8)$$

Each tension term on the RHS is defined corresponding to the decomposition of total force on the LHS, respectively. The stochastic and deterministic portion of the constraint forces are then easily defined via the following expressions, $F^{(c,r)} = n^{*\dagger} \cdot \Lambda^{(r)}$ and $F^{(c,d)} = n^{*\dagger} \cdot \left(\Lambda^{(f)} + \Lambda^{(\phi)} + \Lambda^{(e)}\right)$. The deterministic drift velocity due to each of the forces is simply found from: $\text{H} \cdot F$, where H is the projection tensor. Therefore for RPY HI tensor with no external force, the polymer contribution to stress tensor will be:

$$\bar{\bar{\tau}} = \sum R_\mu \tilde{\zeta} \cdot (\tilde{V}_\mu - V_o) + kT \left(tr(\text{P}) - \iota\right) \quad (5.9)$$

where $\tilde{\zeta}$ is the modified effective friction tensor as defined in equation (5.4) of Öttinger (1996) and $\text{P} = \text{I-}[\text{N} \cdot \text{H}^* \cdot \text{N}^{*\dagger}]^{-1} \cdot \text{H}^*$ is the projection tensor corresponding to the numerical midpoint algorithm.

5.3   Result and discussion

In this section, first the computational efficiency of various models is discussed, in order to determine the relative computational efficiency of each method in terms of the number of beads in a chain for dilute solutions. Our focus will be on the relative performance, computational cost and accuracy of the Barnes and Hut method vs. the direct formation of the mobility tensor. The subsequent estimation of the correlation tensor of the stochastic force is performed through the Krylov subspace method; however for the sake of comparison, Cholesky decomposition of the mobility tensor

is also discussed. The proposed Picard-CG method increases the performance in the final modeling bottleneck, namely, the corrector step in which the constraint forces are calculated. Although the naïve matrix inversion is not explicitly tested, an optimistic value for the naïve method is obtained through the estimation of n^3 operation on the targeted CPU for a general matrix inversion.

In order to determine the accuracy of the B&H method, the single chain trajectory obtained via the B&H method is compared with the trajectory obtained from the direct formation of the RPY HI tensor. As shown in Fig. 5.1-a, two trajectories almost exactly follow the same path and there is no error accumulation for a chain with 25 beads. Moreover, the random error falls within a few percentage of the observable value. The Decomposition times, compared for a wide range of n, reveals that the direct formation of mobility tensor with Krylov subspace method is the most efficient method for a wide range of practical chain sizes, and the B&H method becomes more efficient at about $n^* \approx 12000$. The Corrector time (Fig. 5.1-c) illustrates similar trend; it also shows that the parameter θ , which determines the threshold of substitution of the multipole effect of the source instead of the direct effect, reduces the n^* value as expected. The theoretical computational cost of the code using the naïve method is $O(n^3)$ for large n, however the scaling exponent of the elapsed time vs. the number of beads is about 1.25 for the B&H method, compared to the value of 2.25 for the direct method.

In interpreting the aforementioned results, it is important to consider three important facts. First, the bottleneck of calculation within both decomposition and corrector steps is the matrix-vector multiplication. In case of direct method, all multiplications are performed via the highly optimized Intel MKL library, while the B&H method relies on the inferior optimization offered by the authors. It is highly likely that a tailor-made code targeted for an optimized B&H method reduces the n^* value. Next, the timings reported here are estimated from a single chain at equilibrium. The equilibrium condition in which the chain bead-to-bead distance distribution follows the Gaussian distribution constitutes an unfavorable condition
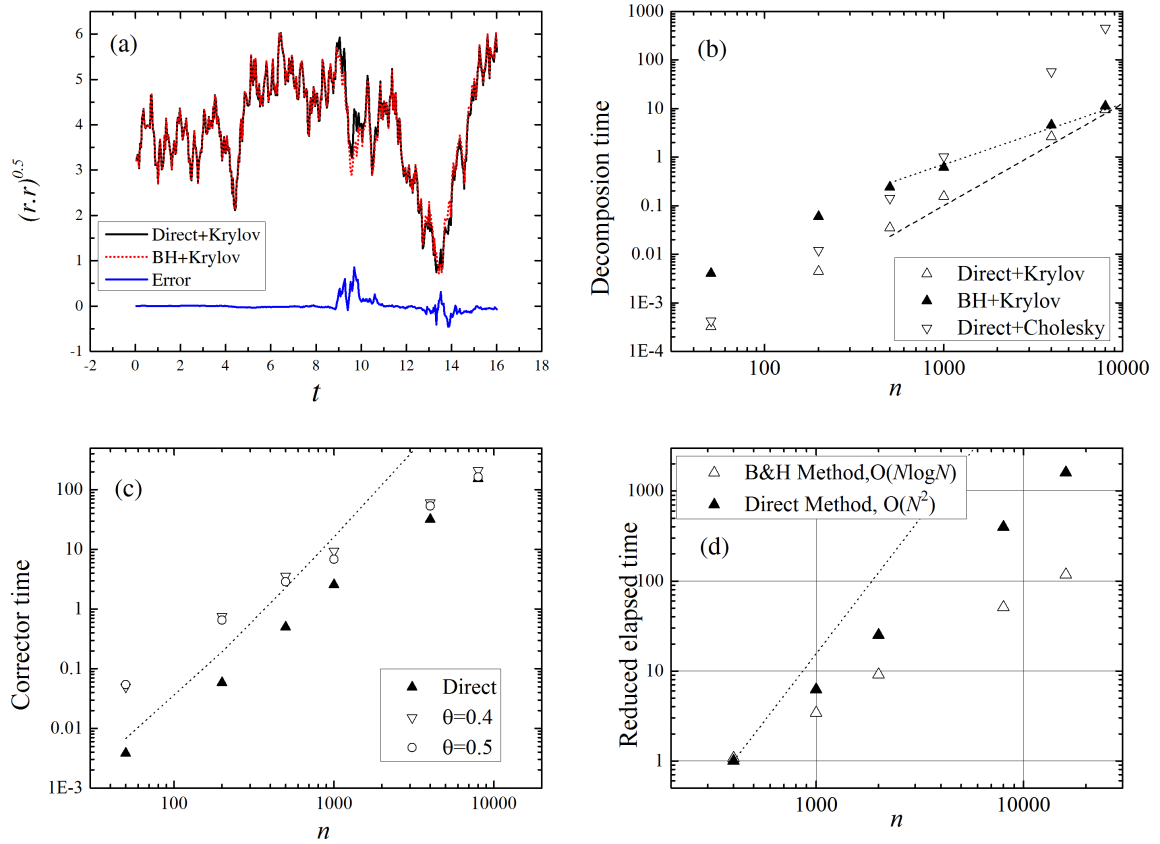
Figure 5.1: Single chain trajectory of the chain is followed with high accuracy by the B&H method (a). The Krylov decomposition algorithm can utilize both B&H and direct formation of the diffusion tensor. Plot (b) demonstrates the relative performance of each method and compares them to the Cholesky method in terms of user-time (sec.) per one step. The corrector time and the scaling factor in the B&H method both are reduced by increasing the θ criterion (c), terms until the first dipole are considered in obtaining the above results. Finally the scaling of the computational cost of each method is shown in (d), the dotted line is the n^3 scaling.

for the B&H method compared to uniform distribution or the chain stretched due to flow kinematics. Moreover, for the semi-dilute regime where several chains are present in the simulation box and their center of mass distances are far apart, which corresponds to favorable θ values, and multipole effect of the whole neighboring chain replaces the contribution of the individual beads, the B&H method gains a significant advantage.

The long-time limit $(t > \lambda)$ of the translational diffusion coefficient of the center of mass of the chain (D) follows theoretically determined power law scaling with the size of the chain. For the free-draining Gaussian chain $D \sim n^{-1.0}$, while for a Zimm model, HI enhances the diffusion so that $D \sim n^{-3/5}$. The corresponding value from the simulation:

$$D \sim \frac{1}{nt} \lim_{t \to \infty} \left(\left\langle \sum r_{ij}(t) \right\rangle - \left\langle \sum r_{ij}(0) \right\rangle \right)$$

of each chain type, is shown in Fig.5.2. The ideal and real free-draining chains scaling coefficient agrees well with the theoretical predictions of the Rouse model. For the chain with HI, both in Θ- and good-solvent, the scaling exponent is in good agreement with theory and experiment (Smith et al., 1996).

The longest relaxation time of the polymer chain was found via Birefringence value as described by Doyle et al. (1997). Similar values obtained via an exponential fit to the last 10% of the conformational relaxation of the fully-extended chains are also shown in Table 5.1; however, in order to rescale the Pe to Wi, the former values where utilized $(\lambda = \lambda_\Delta)$. Closer examination of the relaxation plot of r_e reveals the two regimes of relaxation spectrum: at high extension $(x < 0.6)$ the relaxation is influenced by the HI effects; therefore, irrespective of the excluded volume interactions, chains with HI demonstrate similar relaxation behavior. On the other hand, below $x = 0.5$, Fig.5.3 clearly illustrates by the equal slope of the curves for the {Ideal free draining, HI in Θ-solvent} and {Real free draining, HI in good-solvent} pairs, that the relaxation process is greatly influenced by the excluded

85
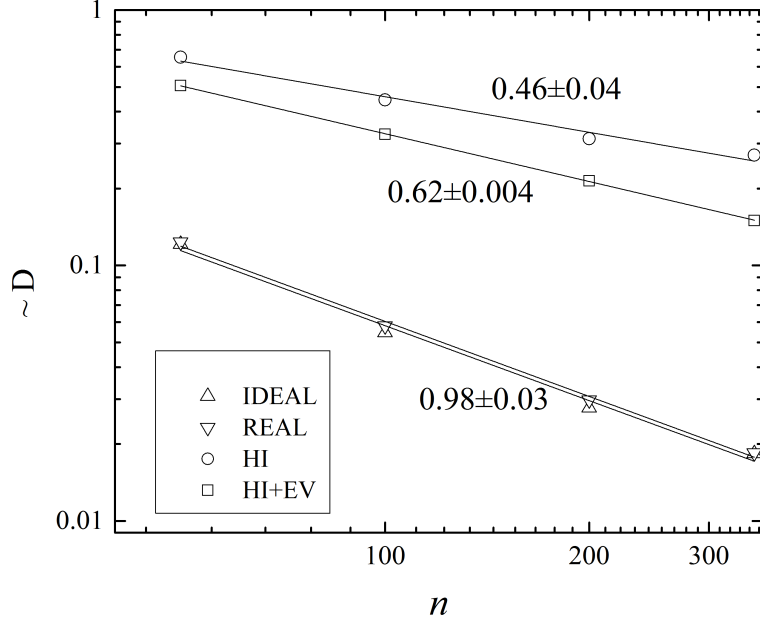
Figure 5.2: Scaling of the translational diffusion coefficient of the chain center of mass. HI significantly increases the diffusion coefficient and excluded volume effect on the scaling is only significant in presence of HI.

volume effects. Notice that the extension at which the transition between regimes happens is roughly equal to the extension at which Langevin and R44 force laws intercept (see chapter 3).

In order to test the proposed stress estimation algorithm, in the remainder of this chapter rheological properties of the chain with HI in good solvent are examined. The contribution of the polymer chain to the stress tensor is calculated for both shear flow and uniaxial extension flow kinematics and examined over a broad range of Wi values for chains with $n = 100$ and $n = 350$. The latter chain is at least twice the larger chain considered in the literature, and based on the result of chapter 3, should provide a better estimate of the effect of EV close to the universal behavior.

The transient viscosity (η^+) and first normal stress coefficient (ψ^+) for shear start-up flow is shown in Fig. 5.4 and Fig. 5.5. The overshoot of first normal stress coefficient, for $Wi > 10$, occurs at about 10-30 strain units (Fig. 5.4a and Fig. 5.5a). The magnitude of the overshoot $\psi^+_{max} \sim Wi^{-0.635}$. In the case of transient viscosity, the

Table 5.1: Longest relaxation time of BDRD chains obtained via birefringence and r_e relaxation of fully extended chains.

	Ideal FD		Real FD		HI Θ-solvent		HI Good-solvent	
n	Δ	r_e	Δ	r_e	Δ	r_e	Δ	r_e
49	43	38	51	43	15	22	19	32
99	162	198	189	260	43.8	66	60	114
199	595	904	751	1007	119	197	172	265
349	1783	2600	2037	5891	230	-	420	-

(a) Longest relaxation time scaling

(b) Relaxation of the end-to-end distance
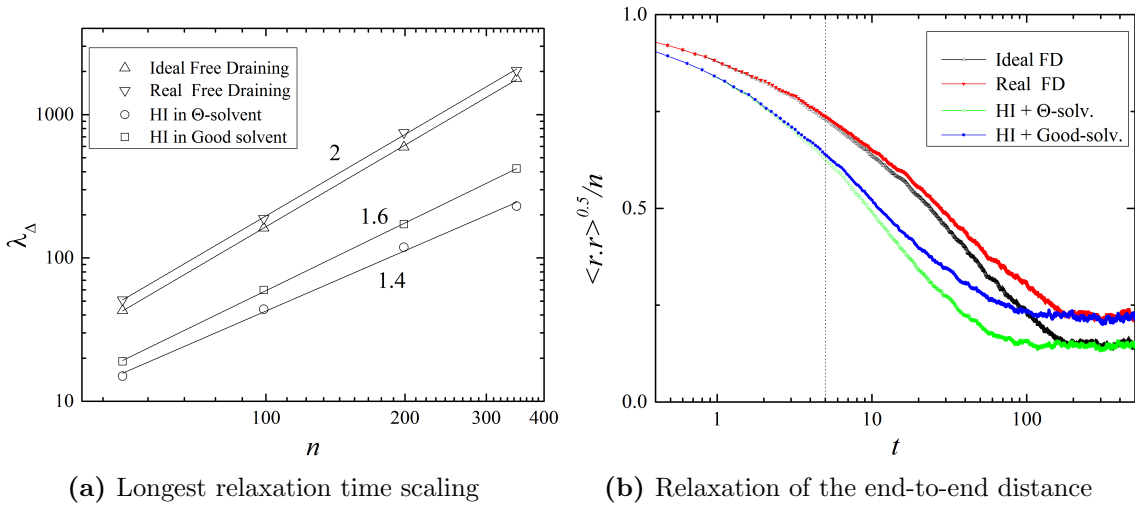
Figure 5.3: Scaling of the longest relaxation time (a). HI significantly decreases relaxation time and excluded volume effect on the scaling is only significant in presence of HI. Relaxation plot of r_e for $n = 50$ with $\lambda \leq 50$ (b). The dotted line qualitatively separates the two regions.
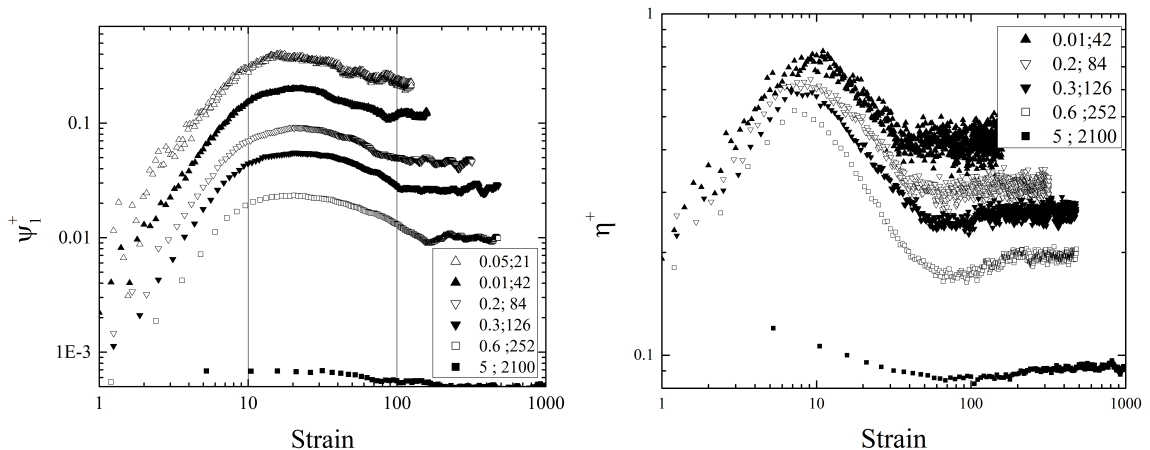
Figure 5.4: Transient rheological properties of chain with HI in good solvent ($n = 350$) at the start-up the shear flow. The legend is the $(Pe; Wi)$ pair.

maximum occurs at slightly smaller Henky strain, and more importantly, at large Wi it is followed by a minima before it plateaus at the steady state level. Although the maxima is well characterized by the Henky strain and it is in exact agreement with experimental observation of start-up of DNA solutions(Hur et al., 2001), the minima in the shear viscosity shifts to higher Henky stresses as Wi increases. The magnitude of the maximum shear viscosity contribution of the polymer in the range shown in Fig. 5.4b follows $\eta_{max}^+ \sim Wi^{0.266}$, for ideal free draining chain this exponent is 0.4-0.45. The overshoot and oscillatory behavior of the shear stress components also appears in the conformational relaxation of the polymeric chain (Hur et al., 2002). However as shown in Fig. 5.6a, the overshoot in r_e as a measure of chain conformation is out of phase compared to the overshoot of the stress tensor, which consistently occurs around 10-30 strain units ($10 < \gamma_{max} < 30$). This *self-inconsistency* between conformation and stress results in an oscillator behavior that extends beyond the longest relaxation time, and the frequency of the oscillation increases with Wi as shown in Fig. 5.6b.

EV and HI also affect the shear-thinning behavior of the rheological properties. In general, our results indicate that the shear-thinning behavior for both shear viscosity (η) and first normal stress coefficient (ψ_1) is close to the estimation of (Doyle et al., 1997) ($\psi \sim Wi^{-14/11}$) only at higher Wi, while for mid-range Wi the absolute value
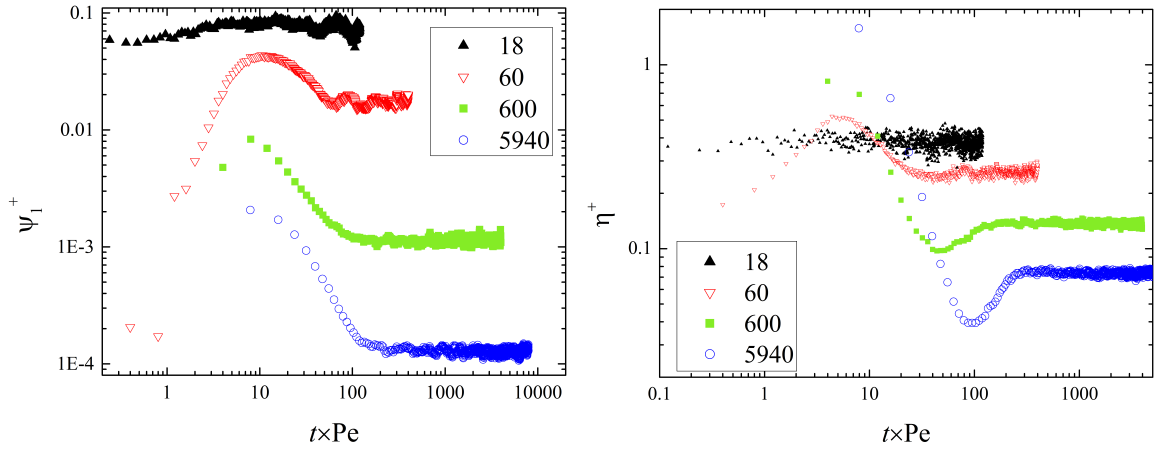
Figure 5.5: Transient rheological properties of chain with HI in good solvent ($n = 100$) at the start-up the shear flow. The Wi for each data set is shown in the legend.
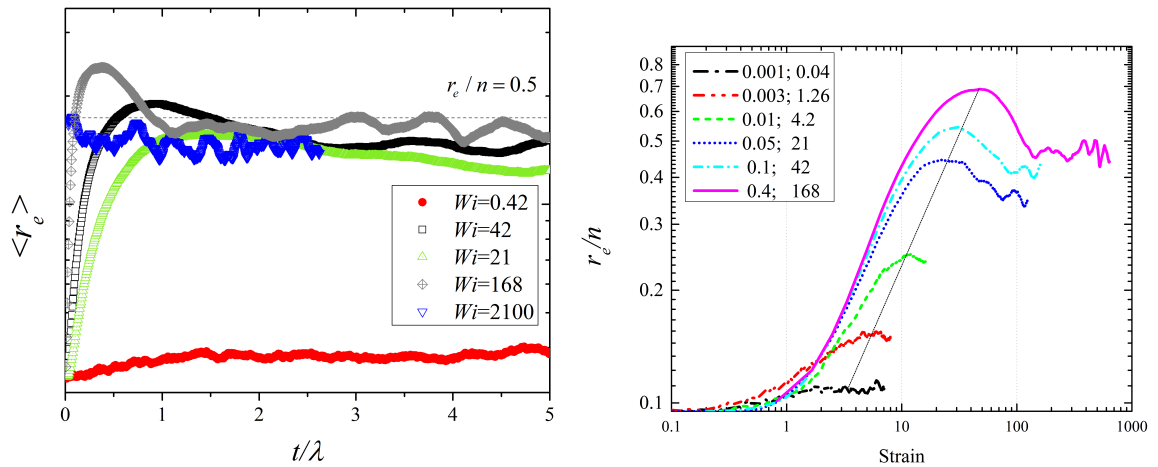
Figure 5.6: Transient conformational properties of chain with HI in good-solvent ($n = 350$) at the start-up the shear flow. The Wi for each data set is shown in the legend. The left figure illustrates the oscillatory behavior which continues over couple of relaxation time and the on the right, wide variation of the the strain of overshoot $\gamma_m ax$ with flow strength is depicted.

89

of the power law exponent is less, and the exponent is not fixed at $-4/3$ ($\psi \sim Wi^{-4/3}$), irrespective of HI and EV as it was concluded earlier for $n < 150$ (Lyulin et al., 1999). In the case of shear viscosity, Petera and Muthukumar (1999) roughly attained a power-law exponent of -0.5 ($\eta \sim Wi^{-0.5}$) in the presence of HI and EV, which is similar to the exponent of free-draining chain ((Liu, 1989; Doyle et al., 1997)), while Hur et al. (2000) found a scaling of -0.257 (Shaqfeh, 2005) from bead-spring simulations. Fig. 5.7 demonstrates the shear thinning properties of chains in good solvent calculated in this work for both $n = 100$ and $n = 350$. Both chains demonstrate a power-low behavior as expected for $10 < Wi$ for $n = 100$ and $30 < Wi < 1000$ in case of the longer chain ($n = 350$), and the shear thinning exponents are -0.281 and -0.4315, respectively. In the case of $n = 350$ the pronounced non-linear region in the log-log plot $0.8 < Wi < 4$ corresponded to the non-linear F-X regime of the initial linear extension of polymeric chain due to the shear flow. This initial regime for small Wi also appears in the scaling of the first normal stress coefficient (ψ_1) with a smaller absolute power-law exponent. While in this first shear-thinning regime (as depicted in Fig. 5.7b) $\psi \sim Wi^{-1.13}$, in the second regime $\psi \sim Wi^{-1.4}$. Although similar trend exists for $n = 100$, the difference between two exponents is smaller (-1.09 and -1.14 for the second regime), in agreement with the smaller non-linear effects of EV for $n = 100$(see Fig. 3.14).

Recent investigation of conformational properties of polymeric chain subject to HI and EV modelled as stiff Franckeal springs by Sendner and Netz (2009) followed by Dalal et al. (2012) have revealed the second region in the extension of the chain due to the flow in which the chain extension decreases as Wi increases. This effect is captured in the BDRD presented in this research as well(Fig.5.8). It has been demonstrated that the shear plateau at $x \approx 0.5$ is due to the tumbling effect.Larson has recently argued that *partial fumbling* of chain segments is the mechanism of shrinkage at very high Wi. The partial fumbling argument does not describe the qualitatively different behavior of r_e observed for chains without HI or excluded volume interaction at high Wi (See Fig. 5.8b and Dalal et al. (2014)).

(a) Shear viscosity **(b)** First normal stress coefficient
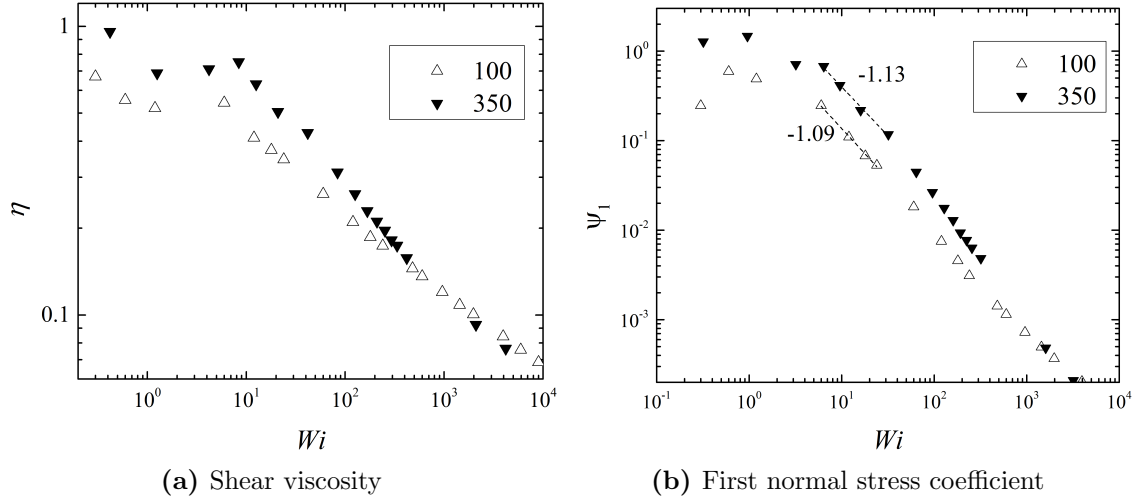
Figure 5.7: Steady-state scaling of the shear rheometry for the single chain in good solvent as obtained from the BDRD simulation. Left graph, illustrates the shear shear viscosity and at right, first normal stress coefficient. After the initial near plateau behavior, longer chain visits at last two regimes of shear thinning as discussed in the text.

An alternative explanation for the shrinkage observed in the aforementioned region is the existence of meta-stable folded conformations. The meta-stable folded conformations occur at high shear rates when the small portion of the chain folded on itself is frozen due to the strong aligning shear flow. For instance, in a chain with 100 segments a small *dynamic existence* of a folded region with length 2 (total of 5 beads) can decrease r_e by 10%. If ideal free draining chain is considered as the reference, interactions that increase the possibility of such folds will result in a more significant shrinkage regime. For instance, HI as a overall cohesive potential will significantly enhance shrinkage. HI with no EV will results in beads that are unrealistically close together; the velocity of these two beads with small distance is strongly correlated due to large coefficient of the HI tensor and other forces are relatively small, their translational degrees of freedom will be highly correlated forming a permanent folded region. When excluded volume is present (no HI), formation of meta-stable folds are not permitted since the strong velocity gradient in the second direction will convect the beads away from each other. When both HI and EV are present, adjacent beads

91
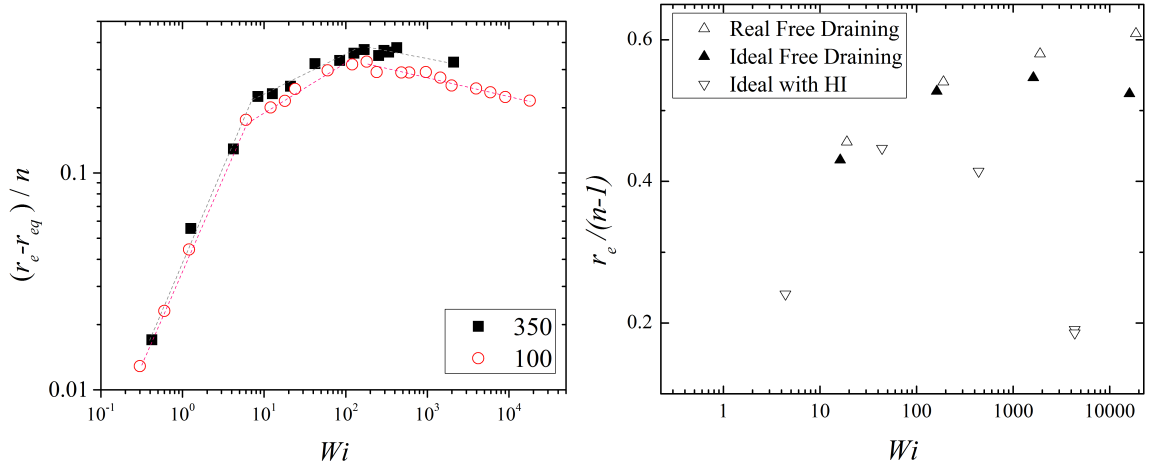
Figure 5.8: Variation of the root mean squared end-to-end distance with Wi in shear flow. The plot on left demonstrates three distinct regions in the log-log plot of $r_e(Wi) - r_e(0)$. On the left r_e is shown for ideal and real free draining chain and also chain only with HI and no excluded volume interaction.

in a folded configuration can move into the neutral direction ($\vec{z}$) and create two folds in xz-plane. Detailed inspection of diagonal components of the radius of gyration reveals that when $r_{g,y} \to 1 \; r_{g,z} \to 2$, which is about thickness of two beads, and stays constant as Wi increases (Fig. 5.9). Meanwhile, the τ_{zz} component of stress tensor increases, although the second normal stress coefficient stays close to zero, as demonstrated in Fig. 5.9c.

The uniaxial flow kinematics, such as the flow in filament stretching rheometer, include the interesting coil to stretch transition feature. Indeed, such effect is also observed in our BDRD flow simulation; as shown in Fig. 5.10a the transition approaches the first order transition as the number of segments increases. However, the critical Wi remains constant at ≈ 0.5, which suggests that the critical strain rate scales as $n^{1.6}$ for the chain in the athermal solvent. This result is in good agreement with the experimental observation and Sim et al. (2007) and corrects the findings of Neelov et al. (2002).
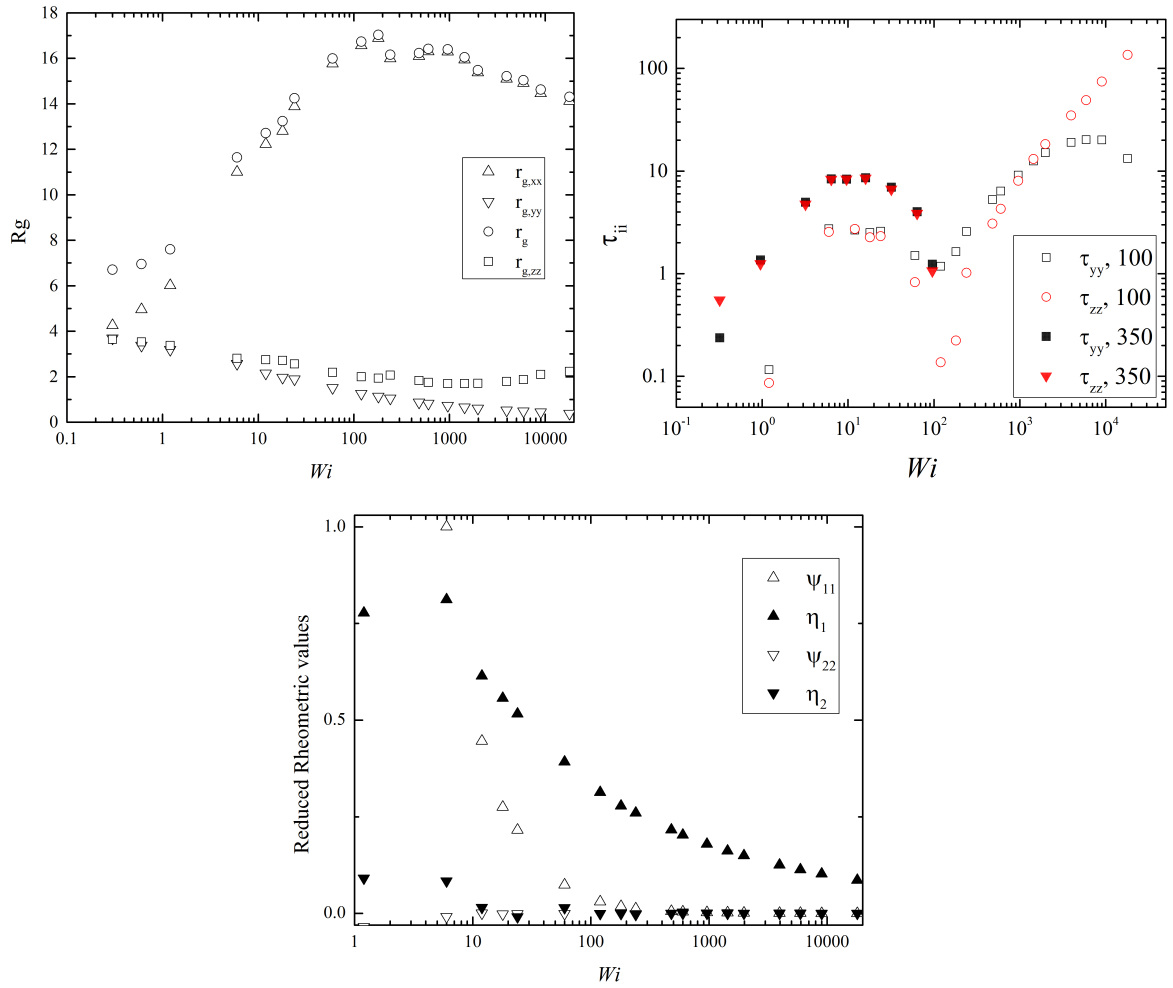
Figure 5.9: Diagonal components of the radius of gyration tensor (a) and the corresponding stress tensor components(b). Despite the growth of stress diagonal components in gradient and neutral direction, the second normal stress coefficient remains about zero.
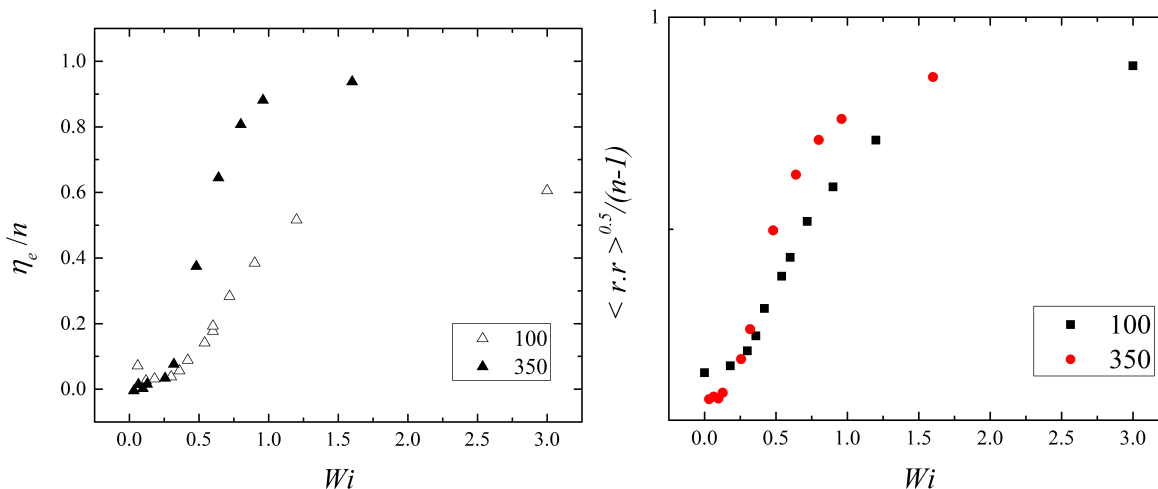
Figure 5.10: The elongational viscosity (right) and coil to stretch transition for dilute solution subject to uniaxial flow kinematics

5.4 Summary

In summary, a new method for BD simulation of bead-rod model of macromolecules is developed, which reduces the computational cost scaling to $n^{\approx 2}$. The efficiency of the B&H based method in BDRD model with HI was discussed and concluded that although B&H method decreased the computational cost scaling exponent further (to about 1.2), it is not most suited for dilute solutions and near equilibrium in the current elaboration and efficiency level of the underlying code. A new algorithm for estimation of the stress tensor has been deployed to study the polymer dynamics and transient rheological properties both in the shear and uniaxial flows. In the shear flow, consistent with the result of chapter 3, at least two shear thinning regimes for shear rheological properties were observed.

Chapter 6

CONCLUSION AND FUTURE WORK

This research has focused on efficient incorporation of long range interactions and analysis of their effects on equilibrium properties and dynamic behavior of colloids and polymeric solutions through computational methods such as MD and BD.

Investigation of the self-assembly of the Janus particles with oppositely charged hemisphere via molecular dynamic concluded that the long range effect, incorporated via Ewald-mesh summation, introduces ordered growth and inaccurate estimation of these effects will significantly perturb the final structure from ordered-growth to spherical packed aggregates. Two distinct building blocks were spotted in self-assembly of JPs, and it has also been demonstrated that at the higher JP concentration, the building blocks, i.e., rings and strings, enact as building blocks by either joining into the same structure but with larger population of JPs or by hierarchical co-assembly into larger porous structures or spiral chains. Moreover, the crucial effect of random defects in synthesis of spherical JP was exposed through allocation of random surface defects on the model JP and inspection of their self-assembly deviation compared to perfect JPs. In order to obtain further insight into the dynamics of JPs, it is constructive to look into the correlation between rotational and

translational diffusion. Addition of a more fine-grained surface functional groups and explicit water molecules will enable prediction of realistic values for both rotational and translational diffusion for future analysis.

Next, the equilibrium properties and the elastic response of polyelectrolyte were discussed within the framework of Brownian Dynamics. Specifically, the electrostatic Kuhn length in the two regimes, in which electrostatic interaction can be effectively replaced by excluded volume interaction, demonstrated linear dependency with salt concentration which was represented through the ratio of excluded volume radius to the intrinsic Kuhn length. However, the slope of this linear dependency in each regime was distinct and as the relative magnitude of the distance between charged groups along the contour length increases with respect to the intrinsic Kuhn length, a parabolic function fairly fits both regimes. The analysis was extended to the F-X behavior which manifested good agreement with the single chain F-X experiments on ssDNA published elsewhere. Finally, similar to the treatment of the Inverse Langevin force-law via Padé expansion, at the limit of athermal solvent a novel force-law in form of a real function was extracted from the discrete set of data points utilizing a newly developed discrete Padé expansion.

The aforementioned force law (R44) was then implemented in the Bead-Spring model. It was demonstrated that the transition from coil state to the stretched state in case of R44 elastic dumbbell or chain is dampened compared to the FENE force law for both shear and uniaxial flow kinematics when plotted against the Pe. The shear-thinning behavior of dilute polymeric solution of R44 chains is reduced at intermediate Pe compared to the FENE chains. However when the finite extensibility of the chain increases, at small Pes FENE chain demonstrated no shear-thinning while the R44 chain preserved the shear-thinning properties. Therefore, the shear-thinning behavior of R44 chains at small Pe is inherent to the elastic response of the chain with EV.

Brownian dynamics of Bead-rod (BDRD) model of polymer chain with good solvent confirms the above observations and provides the scaling exponents of the shear-thinning, relaxation time and the onset and slope of coil-stretch transition. The

effective n^5 scaling of number of operation (2 from relaxation time scaling and 3 for solution of the constraints equation) renders such simulation inefficient for $n > 150$,which is the limit previously accomplished in literature. A new BDRD algorithm based on a mixed Picard-CG (conjugate gradient) method was developed to drop the exponent as much as one unit. Moreover, this exponent can further drop by the new method for the estimation of the HI and diffusion matrix decomposition based on the multipole tree algorithm (B&H) method. Complementary to aforementioned effort, a new method for stress calculation of bead-rod model with EV and HI was developed with accurate predictions even in the transient regime. For chain lengths up to $n = 350$ computed rheological properties are in general agreement with the R44 force law; specifically, there will be an additional shear-thinning region for both η and ψ_1 at low Wi corresponding to the small affine extension. The exponent of the second shear-thinning regime with increasing Wi is smaller for chains, with excluded volume and HI compared to the free-draining Kramer's chains. At large Wi chain with EV and HI reaches asymptotic regime predicted for the free-draining chains which corresponds to the screening of EV and small influence of HI at large extensions.

The framework and algorithm developed in this research lays the foundation for future investigation of flexible macromolecules. Specifically, efficiency of the Bead-rod model can be employed to study the intra-molecular knot dynamics in single chains. The stress algorithm is potentially able to separate contribution of each individual force to the polymer stress tensor and predict their relative prevalence at various flow kinematics and Wi similar in order to extend the previous effort which was limited only to the viscous and brownian contribution in Kramers chains. From the computational perspective, although B&H method threshold of efficiency is large for dilute solutions, efficient version of the multipole methods developed here can be effective in dealing with semi-dilute solutions dynamics, especially when such efforts are combined with CPU/GPU implementation of the code.

Bibliography

Agarwal, U. S., Bhargava, R., and Mashelkar, R. A. (1998). Brownian dynamics simulation of a polymer molecule in solution under elongational flow. *The Journal of Chemical Physics*, 108(4):1610–1617. 72

Ando, T., Chow, E., Saad, Y., and Skolnick, J. (2012). Krylov subspace methods for computing hydrodynamic interactions in brownian dynamics simulations. *The Journal of Chemical Physics*, 137(6):064106–14. 71, 73

Bao, G. and Suresh, S. (2003). Cell and molecular mechanics of biological materials. *Nature materials*, 2(11):715–725. 25

Barnes, J. and Hut, P. (1986). A hierarchical o (n log n) force-calculation algorithm. *Nature*, 324:446–449. 71

Barrat, J.-L. and Joanny, J.-F. (1993). Persistence length of polyelectrolyte chains. *EPL (Europhysics Letters)*, 24(5):333. 26, 30, 39

Bird, R., Curtiss, C., Armstrong, R., and Hassager, O. (1987). Dynamics of polymeric liquids. vol. 2: Kinetic theory. *Wiley-Interscience, 1987*, page 450. 52

Bird, R. B., Curtiss, C., Armstrong, R., and Hassager, O. (1996). *Dynamics of Polymeric Liquids, 2 Volume Set*. Wiley-Interscience. 54, 69, 80

Brockman, C., Kim, S. J., and Schroeder, C. M. (2011). Direct observation of single flexible polymers using single stranded dna. *Soft Matter*, 7(18):8005–8012. 3

Bucaro, M., Kolodner, P., Taylor, J., Sidorenko, A., Aizenberg, J., and Krupenkin, T. (2008). Tunable liquid optics: electrowetting-controlled liquid mirrors based on self-assembled janus tiles. *Langmuir*, 25(6):3876–3879. 7

Bustamante, C., Smith, S., Liphardt, J., and Smith, D. (2000). Single-molecule studies of dna mechanics. *Current Opinion in Structural Biology*, 10(3):279–285. 3

Chen, H., Meisburger, S. P., Pabit, S. A., Sutton, J. L., Webb, W. W., and Pollack, L. (2012). Ionic strength-dependent persistence lengths of single-stranded rna and dna. *Proceedings of the National Academy of Sciences*, 109(3):799–804. 26

Chen, Q., Whitmer, J., Jiang, S., Bae, S., Luijten, E., and Granick, S. (2011). Supracolloidal reaction kinetics of janus spheres. *Science*, 331(6014):199. 7

Cifre, J. H. and de la Torre, J. G. (1999). Steady-state behavior of dilute polymers in elongational flow. dependence of the critical elongational rate on chain length, hydrodynamic interaction, and excluded volume. *Journal of Rheology*, 43(2):339–358. 61

Cohen, A. (1991). A padè approximant to the inverse langevin function. *Rheologica Acta*, 30(3):270–273. 31, 33

Cranford, S. W. and Buehler, M. J. (2012). Variation of weak polyelectrolyte persistence length through an electrostatic contour length. *Macromolecules*, 45(19):8067–8082. 30

Dalal, I., Hoda, N., and Larson, R. (2012). Multiple regimes of deformation in shearing flow of isolated polymers. *Journal of Rheology*, 56(2):305–332. 72, 73, 90

Dalal, I. S., Hsieh, C.-C., Albaugh, A., and Larson, R. G. (2014). Effects of excluded volume and hydrodynamic interactions on the behavior of isolated bead-rod polymer chains in shearing flow. *AIChE Journal*, 60(4):1400–1412. 90

Dehnen, W. (2000). A very fast and momentum-conserving tree code. *The Astrophysical Journal Letters*, 536(1). 71

Dessinges, M. N., Maier, B., Zhang, Y., Peliti, M., Bensimon, D., and Croquette, V. (2002). Stretching single stranded dna, a model polyelectrolyte. *Physical Review Letters*, 89(24):248102. PRL. 28

Dobrynin, A. V. (2005). Electrostatic persistence length of semiflexible and flexible polyelectrolytes. *Macromolecules*, 38(22):9304–9314. 26

Dobrynin, A. V. and Rubinstein, M. (2005). Theory of polyelectrolytes in solutions and at surfaces. *Progress in Polymer Science*, 30(11):1049–1118. 27

Doyle, P., Shaqfeh, E., and Gast, A. (1997). Dynamic simulation of freely draining flexible polymers in steady linear flows. *Journal of Fluid Mechanics*, 334(1):251–291. 52, 80, 85, 88, 90

Du, Q., Liu, C., and Yu, P. (2005). Fene dumbbell model and its several linear and nonlinear closure approximations. *Multiscale Modeling and Simulation*, 4(3):709–731. 52

Echenique, P., Calvo, I., and Alonso, J. L. (2006). Quantum mechanical calculation of the effects of stiff and rigid constraints in the conformational equilibrium of the alanine dipeptide. *Journal of Computational Chemistry*, 27(14):1733–1747. 69

Erhardt, R., Zhang, M., Bker, A., Zettl, H., Abetz, C., Frederik, P., Krausch, G., Abetz, V., and Mller, A. (2003). Amphiphilic janus micelles with polystyrene and poly (methacrylic acid) hemispheres. *Journal of the American Chemical Society*, 125(11):3260–3267. 2, 7

Everaers, R., Milchev, A., and Yamakov, V. (2002). The electrostatic persistence length of polymers beyond the osf limit. *The European Physical Journal E: Soft Matter and Biological Physics*, 8(1):3–14. 26

Fetsko, S. W. and Cummings, P. T. (1995). Brownian dynamics simulation of bead–spring chain models for dilute polymer solutions in elongational flow. *Journal of Rheology*, 39(2):285–299. 52

Grzelczak, M., Vermant, J., Furst, E. M., and Liz-Marzan, L. M. (2010). Directed self-assembly of nanoparticles. *ACS Nano*, 4(7):3591–3605. 2

Hara, M. (1993). *Polyelectrolytes: Science and Technologies.* CRC Press. 37

Hardin, R., Sloane, N., and Smith, W. (2008). Spherical codes. *See http://www.research.att.com/ njas/packings.* 10

Hassager, O. (1974). Kinetic theory and rheology of bead-rod models for macromolecular solutions. i. equilibrium and steady flow properties. *The Journal of Chemical Physics*, 60(5):2111–2124. 69

Hoda, N. and Kumar, S. (2008). Brownian dynamics simulations of polyelectrolyte adsorption in shear flow: Effects of solvent quality and charge patterning. *The Journal of Chemical Physics*, 128(16):164907. 53

Hong, L., Cacciuto, A., Luijten, E., and Granick, S. (2006). Clusters of charged janus spheres. *Nano letters*, 6(11):2510–2514. 3, 7, 8

Hsieh, C.-C. and Larson, R. G. (2004). Modeling hydrodynamic interaction in brownian dynamics: Simulations of extensional and shear flows of dilute solutions of high molecular weight polystyrene. *Journal of Rheology*, 48(5):995–1021. 53

Hsu, H.-P. and Binder, K. (2012). Stretching semiflexible polymer chains: Evidence for the importance of excluded volume effects from monte carlo simulation. *The Journal of Chemical Physics*, 136(2):024901–20. 29, 56

Hsu, H.-P., Paul, W., and Binder, K. (2013). Estimation of persistence lengths of semiflexible polymers: Insight from simulations. *arXiv preprint arXiv:1303.2543.* 37

Hur, J., Shaqfeh, E., and Larson, R. (2000). Brownian dynamics simulations of single dna molecules in shear flow. *Journal of Rheology*, 44(4):713–742. 52, 90

Hur, J. S., Shaqfeh, E. S., Babcock, H. P., and Chu, S. (2002). Dynamics and configurational fluctuations of single dna molecules in linear mixed flows. *Physical Review E*, 66(1):011915. 88

Hur, J. S., Shaqfeh, E. S., Babcock, H. P., Smith, D. E., and Chu, S. (2001). Dynamics of dilute and semidilute dna solutions in the start-up of shear flow. *Journal of Rheology*, 45:421. 88

Hynninen, A.-P. and Dijkstra, M. (2005). Phase diagram of dipolar hard and soft spheres: Manipulation of colloidal crystal structures by an external field. *Physical review letters*, 94(13):138303. 8

Janovà, J. (2011). Applications of a constrained mechanics methodology in economics. *European Journal of Physics*, 32(6):1443. 69

Jendrejack, R., De Pablo, J., and Graham, M. (2002). Stochastic simulations of dna in flow: Dynamics and the effects of hydrodynamic interactions. *The Journal of Chemical Physics*, 116:7752. 52

Jendrejack, R., Graham, M., and De Pablo, J. (2000). Hydrodynamic interactions in long chain polymers: Application of the chebyshev polynomial approximation in stochastic simulations. *The Journal of Chemical Physics*, 113:2894. 71

Jendrejack, R. M., Schwartz, D. C., de Pablo, J. J., and Graham, M. D. (2004). Shear-induced migration in flowing polymer solutions: Simulation of long-chain dna in microchannels. *The Journal of Chemical Physics*, 120(5):2513–2529. 53

Jiang, S., Schultz, M. J., Chen, Q., Moore, J. S., and Granick, S. (2008). Solvent-free synthesis of janus colloidal particles. *Langmuir*, 24(18):10073–10077. 7, 13

Katchalsky, A., Künzle, O., and Kuhn, W. (1950). Behavior of polyvalent polymeric ions in solution. *Journal of Polymer Science*, 5(3):283–300. 26

Katchalsky, A., Lifson, S., and Mazur, J. (1953). The electrostatic free energy of polyelectrolyte solutions. i. randomly kinked macromolecules. *Journal of Polymer Science*, 11(5):409–423. 26

Kim, J., Lee, D., Shum, H., and Weitz, D. (2008). Colloid surfactants for emulsion stabilization. *Advanced Materials*, 20(17):3239–3243. 7

Kirkwood, J. G. and Riseman, J. (1948). The intrinsic viscosities and diffusion constants of flexible macromolecules in solution. *The Journal of Chemical Physics*, 16:565. 69

Kramers, H. A. (1946). The behavior of macromolecules in inhomogeneous flow. *The Journal of Chemical Physics*, 14:415. 69

Kuhn, W. and Grün, F. (1946). Statistical behavior of the single chain molecule and its relation to the statistical behavior of assemblies consisting of many chain molecules. *Journal of Polymer Science*, 1(3):183–199. 3

Lattuada, M. and Hatton, T. A. (2011). Synthesis, properties and applications of janus nanoparticles. *Nano Today*, 6(3):286–308. 17

Liang, Z., Gimbutas, Z., Greengard, L., Huang, J., and Jiang, S. (2013). A fast multipole method for the rotnprageryamakawa tensor and its applications. *Journal of Computational Physics*, 234:133–139. 71

Liu, S., Ashok, B., and Muthukumar, M. (2004). Brownian dynamics simulations of bead-rod-chain in simple shear flow and elongational flow. *Polymer*, 45(4):1383–1389. 72

Liu, T. W. (1989). Flexible polymer chain dynamics and rheological properties in steady flows. *The Journal of Chemical Physics*, 90(10):5826–5842. 32, 90

Lyulin, A. V., Adolf, D. B., and Davies, G. R. (1999). Brownian dynamics simulations of linear polymers under shear flow. *The Journal of Chemical Physics*, 111(2):758–771. 52, 90

Maier, B. and Rdler, J. (1999). Conformation and self-diffusion of single dna molecules confined to two dimensions. *Physical review letters*, 82(9):1911–1914. 4

Marciel, A. B. and Schroeder, C. M. (2013). New directions in single polymer dynamics. *Journal of Polymer Science Part B: Polymer Physics*, 51(7):556–566. 69

Marko, J. F. and Siggia, E. D. (1995). Stretching dna. *Macromolecules*, 28(26):8759–8770. 56

Miller, W. L. and Cacciuto, A. (2009). Hierarchical self-assembly of asymmetric amphiphatic spherical colloidal particles. *Physical Review E*, 80(2):021404. 8

Miyamoto, S. and Kollman, P. A. (1992). Settle: an analytical version of the shake and rattle algorithm for rigid water models. *Journal of computational chemistry*, 13(8):952–962. 69

Morse, D. C. (2004). Theory of constrained brownian motion. *Advances in Chemical Physics*, 128(65-189):110. 71, 81

Muthukumar, M. (1987). Adsorption of a polyelectrolyte chain to a charged surface. *The Journal of Chemical Physics*, 86(12):7230–7235. 26, 30

Neelov, I. M., Adolf, D. B., Lyulin, A. V., and Davies, G. R. (2002). Brownian dynamics simulation of linear polymers under elongational flow: Bead–rod model with hydrodynamic interactions. *The Journal of Chemical Physics*, 117(8):4030–4041. 72, 92

Öttinger, H. (1996). *Stochastic processes in polymeric fluids.* Springer Berlin. 32, 52, 80, 82

Öttinger, H. C. (1994). Brownian dynamics of rigid polymer chains with hydrodynamic interactions. *Physical Review E*, 50(4):2696–2701. 69, 80

Pamies, R., Lopez Martinez, M. C., Hernandez Cifre, J. G., and Garcia de la Torre, J. (2005). Non-newtonian viscosity of dilute polymer solutions. *Macromolecules*, 38(4):1371–1377. 53

Panwar, A. S. and Kumar, S. (2005). Brownian dynamics simulations of polyelectrolyte adsorption in shear flow. *The Journal of Chemical Physics*, 122(15):154902–12. 53

Park, B. J., Brugarolas, T., and Lee, D. (2011). Janus particles at an oil-water interface. *Soft Matter*, 7(14):6413–6417. 17

Pasquali, M. and Morse, D. C. (2002). An efficient algorithm for metric correction forces in simulations of linear polymers with constrained bond lengths. *The Journal of Chemical Physics*, 116:1834. 112

Pattanayek, S. and Prakash, J. R. (2008). Is the electrostatic blob model relevant to dilute polyelectrolyte solutions undergoing shear flow? *Macromolecules*, 41(6):2260–2270. 30

Perkins, T., Smith, D., and Chu, S. (1997). Single polymer dynamics in an elongational flow. *Science*, 276(5321):2016–2021. 3

Petera, D. and Muthukumar, M. (1999). Brownian dynamics simulation of beadrod chains under shear with hydrodynamic interaction. *The Journal of Chemical Physics*, 111:7614. 72, 90

Pham, T. T., Sunthar, P., and Prakash, J. R. (2008). An alternative to the bead-rod model: Bead-spring chains with successive fine graining. *Journal of Non-Newtonian Fluid Mechanics*, 149(13):9–19. 61

Pincus, P. (1976). Excluded volume effects and stretched polymer chains. *Macromolecules*, 9(3):386–388. 53, 61

Radhakrishnan, R. and Underhill, P. T. (2012). Impact of solvent quality on the hysteresis in the coilstretch transition of flexible polymers in good solvents. *Macromolecules*, 46(2):548–554. 53

Radhakrishnan, R. and Underhill, P. T. (2013). Fluctuations in the coil-stretch transition of flexible polymers in good solvents: A peak due to nonlinear force relation. *Physical Review E*, 88(1):012606. 53

Ren, B., Ruditskiy, A., Song, J. H., and Kretzschmar, I. (2012). Assembly behavior of iron oxide-capped janus particles in a magnetic field. *Langmuir*, 28(2):1149–56. 17

Rey, A., Freire, J., and de la Torre, J. (1992). Brownian dynamics simulation of flexible polymer chains with excluded volume and hydrodynamic interactions. a comparison with monte carlo and theoretical results. *Polymer*, 33(16):3477–3481. 35, 72

Rief, M., Oesterhelt, F., Heymann, B., and Gaub, H. (1997). Single molecule force spectroscopy on polysaccharides by atomic force microscopy. *Science*, 275(5304):1295. 3

Rubinstein, M. and Colby, R. H. (2003). *Polymer physics.* OUP Oxford. xi, 36, 52

Ryckaert, J.-P., Ciccotti, G., and Berendsen, H. J. (1977). Numerical integration of the cartesian equations of motion of a system with constraints: molecular dynamics of¡ i¿ n¡/i¿-alkanes. *Journal of Computational Physics*, 23(3):327–341. 69

Saleh, O. A., McIntosh, D. B., Pincus, P., and Ribeck, N. (2009). Nonlinear low-force elasticity of single-stranded dna molecules. *Physical Review Letters*, 102(6). xiii, 3, 28, 29, 44, 48, 69

Schäfer, L. and Elsner, K. (2004). Calculation of the persistence length of a flexible polymer chain with short-range self-repulsion. *The European Physical Journal E*, 13(3):225–237. 37, 39

Schieber, J. D. and Obasanjo, O. (2005). On estimating stress in free-draining kramers chain simulations using stochastic filtering. *Journal of Non-Newtonian Fluid Mechanics*, 127(2):89–93. 80

Schmidt, R. R., Cifre, J. G. H., and de la Torre, J. G. (2011). Comparison of brownian dynamics algorithms with hydrodynamic interaction. *The Journal of Chemical Physics*, 135(8):084116–10. 71

Schroeder, C., Shaqfeh, E., and Chu, S. (2004). Effect of hydrodynamic interactions on dna dynamics in extensional flow: Simulation and single molecule experiment. *Macromolecules*, 37(24):9242–9256. 53

Schulz, M. (2003). *Statistical physics and economics: concepts, tools and applications*, volume 184. Springer. 69

Sciortino, F., Giacometti, A., and Pastore, G. (2009). Phase diagram of janus particles. *Physical review letters*, 103(23):237801. 8

Sendner, C. and Netz, R. (2009). Single flexible and semiflexible polymers at high shear: Non-monotonic and non-universal stretching response. *The European Physical Journal E*, 30(1):75–81. 90

Shaqfeh, E. S. (2005). The dynamics of single-molecule dna in flow. *Journal of Non-Newtonian Fluid Mechanics*, 130(1):1–28. 90

Sim, H., Khomami, B., and Sureshkumar, R. (2007). Flowinduced chain scission in dilute polymer solutions: Algorithm development and results for scission dynamics in elongational flow. *Journal of Rheology*, 51(6):1223–1251. 72, 80, 92

Skolnick, J. and Fixman, M. (1977). Electrostatic persistence length of a wormlike polyelectrolyte. *Macromolecules*, 10(5):944–948. 26

Smith, D., Babcock, H., and Chu, S. (1999). Single-polymer dynamics in steady shear flow. *Science*, 283(5408):1724–1727. 3

Smith, D. E., Perkins, T. T., and Chu, S. (1996). Dynamical scaling of dna diffusion coefficients. *Macromolecules*, 29(4):1372–1373. 85

Smith, S., Finzi, L., and Bustamante, C. (1992a). Direct mechanical measurements of the elasticity of single dna molecules by using magnetic beads. *Science*, 258(5085):1122. 3

Smith, S., Finzi, L., and Bustamante, C. (1992b). Direct mechanical measurements of the elasticity of single dna molecules by using magnetic beads. *Science*, 258(5085):1122. 69

Somani, S., Shaqfeh, E. S. G., and Prakash, J. R. (2010). Effect of solvent quality on the coil-stretch transition. *Macromolecules*, 43(24):10679–10691. 53

Somasi, M., Khomami, B., Woo, N., Hur, J., and Shaqfeh, E. (2002). Brownian dynamics simulations of bead-rod and bead-spring chains: numerical algorithms and coarse-graining issues. *Journal of Non-Newtonian Fluid Mechanics*, 108(1-3):227–255. 32, 52, 55, 70

Stevens, M. J., McIntosh, D. B., and Saleh, O. A. (2012). Simulations of stretching a strong, flexible polyelectrolyte. *Macromolecules*, 45(14):5757–5765. 29

Stoltz, C., de Pablo, J. J., and Graham, M. D. (2007). Simulation of nonlinear shear rheology of dilute salt-free polyelectrolyte solutions. *The Journal of Chemical Physics*, 126(12):124906. 30

Sukhishvili, S., Chen, Y., Mller, J., Schweizer, K., Gratton, E., and Granick, S. (2000). Diffusion of a polymer pancake. *Nature*, 406(6792):146–146. 4

Suzuki, D., Tsuji, S., and Kawaguchi, H. (2007). Janus microgels prepared by surfactant-free pickering emulsion-based modification and their self-assembly. *Journal of the American Chemical Society*, 129(26):8088–8089. 7, 13

Tanner, R. and Stehrenberger, W. (1971). Stresses in dilute solutions of beadnonlinear-spring macromolecules. i. steady potential and plane flows. *The Journal of Chemical Physics*, 55:1958. 57

Toan, N. M. and Thirumalai, D. (2012). On the origin of the unusual behavior in the stretching of single-stranded dna. *The Journal of Chemical Physics*, 136(23):235103–5. 29, 30

Torchilin, V. P. (2001). Structure and design of polymeric surfactant-based drug delivery systems. *J Control Release*, 73(2-3):137–72. 7

Trahan, D. W. and Doyle, P. S. (2010). Simulating the relaxation of stretched dna in slitlike confinement. *Macromolecules*, 44(2):383–392. 53

Whitesides, G. M. and Grzybowski, B. (2002). Self-assembly at all scales. *Science*, 295(5564):2418–2421. 2

Woo, N. J., Shaqfeh, E. S., and Khomami, B. (2004). Effect of confinement on dynamics and rheology of dilute dna solutions. i. entropic spring force under confinement and a numerical algorithm. *Journal of Rheology*, 48(2):281–298. 53

Xu, Q., Kang, X., Bogomolni, R. A., and Chen, S. (2010). Controlled assembly of janus nanoparticles. *Langmuir*, 26(18):14923–14928. 7, 17

Appendix

Appendix A

A.1   The Metric force formulation

The metric force is defined as $F^{(m)} = \frac{kT}{2} \frac{\partial}{\partial R} \ln \left[\det \left(\hat{G} \right) \right]$, where $\hat{G} = \frac{1}{m} N \cdot N^\dagger$ and $N^i_\mu = \dfrac{\partial c^i}{\partial R^\mu}$. It is more convenient to calculate the metric force using the following identity:

$$F^{(m)} = \frac{kT}{2} \frac{\partial}{\partial R} \ln \left[\det \left(\hat{G} \right) \right] = \frac{kT}{2} \hat{G}^{-1} : \frac{\partial \hat{G}}{\partial R} \tag{A.1}$$

Since N is a bidiagonal matrix, $\hat{G}$ will be a (symmetric) tridiagonal matrix:

$$\hat{G}_{i,i} = (\nabla_R C)_{i,i} \cdot (\nabla_R C)_{i,i} + (\nabla_R C)_{i,i+1} \cdot (\nabla_R C)_{i,i+1} = 4u_i \cdot u_i + 4(-u_i) \cdot (-u_i) = 8u_i \cdot u_i$$

$$\hat{G}_{i,i+1} = (\nabla_R C)_{i,i+1} \cdot (\nabla_R C)_{i+1,i+1} = -4u_i \cdot u_{i+1}$$

which is basically the same result as Pasquali and Morse (2002), however a factor of 4 is missing in their original work. Calculation of $\hat{G}^{-1}$ is trivial and $\frac{\partial \hat{G}}{\partial R}$ produces a 3rd rank tensor: $A_{ijk} = \frac{\partial \hat{G}_{ij}}{\partial R_k}$. Since $\hat{G}$ is tridiagonal, its only necessary to consider limited terms in the **A** tensor, namely:

$$\hat{G}_{i,i} = f(R_{i+1}, R_i)$$

$$\hat{G}_{i+1,i} = \hat{G}_{i,i+1} = f(R_{i+2}, R_{i+1}, R_i)$$

$$\frac{\partial \hat{G}_{i,i}}{4\partial R_i} = -4u_i \qquad \frac{\partial \hat{G}_{i+1,i}}{4\partial R_i} = \frac{\partial \hat{G}_{i,i+1}}{4\partial R_i} = +u_{i+1}$$

$$\frac{\partial \hat{G}_{i,i}}{4\partial R_{i+1}} = 4u_i \qquad \frac{\partial \hat{G}_{i+1,i}}{4\partial R_{i+1}} = \frac{\partial \hat{G}_{i,i+1}}{4\partial R_{i+1}} = -u_{i+1} + u_i$$

$$\frac{\partial \hat{G}_{i+1,i}}{4\partial R_{i+2}} = \frac{\partial \hat{G}_{i,i+1}}{4\partial R_{i+2}} = -u_i$$

In other words the non-zero elements of $\mathbf{A}$ are:

$$\begin{bmatrix} o & a_{i-2,i-1,i} & o & o \\ a_{i-1,i-2,i} & a_{i-1,i-1,i} & a_{i-1,i,i} & o \\ o & a_{i,i-1,i} & a_{i,i,i} & a_{i,i+1,i} \\ o & o & a_{i+1,i,i} & o \end{bmatrix} =$$

$$\begin{bmatrix} o & a_{i-2,i-1} & o & o \\ a_{i-1,i-2} & a_{i-1,i-1} & a_{i-1,i} & o \\ o & a_{i,i-1} & a_{i,i} & a_{i,i+1} \\ o & o & a_{i+1,i} & o \end{bmatrix}_i = 4 \begin{bmatrix} o & -u_{i-2} & o & o \\ -u_{i-2} & 4u_{i-1} & -u_i + u_{i-1} & o \\ o & -u_i + u_{i-1} & -4u_i & u_{i+1} \\ o & o & u_{i+1} & o \end{bmatrix}_i$$

$$\begin{aligned}
F_k^{(m)} &= \mathrm{g}_{ij}\mathrm{A}_{ijk} \\
&= \mathrm{g}_{kk}\mathrm{A}_{kkk} + \mathrm{g}_{k-1,k-1}\mathrm{A}_{k-1,k-1,k} \\
&\quad + 2\left(\mathrm{g}_{k,k+1}\mathrm{A}_{k,k+1,k} + \mathrm{g}_{k-1,k}\mathrm{A}_{k-1,k,k} + \mathrm{g}_{k-2,k-1}\mathrm{A}_{k-2,k-1,k}\right)
\end{aligned} \tag{A.2}$$

This means $O(5N)$ operation is required in order to assemble the metric force vector.

A.2   Multipole expansion of RPY-HI tensor

A.2.1   Recursive formulas for Multipole moments of the tree

Multipole expansion of $1/r$ potential of a group of particles is performed around their center of mass (charge or force):

$$r_{C,\alpha,N} = \frac{\sum\limits_{1}^{N} |v_{i,\alpha}| r_i}{\sum\limits_{1}^{N} |v_{i,\alpha}|},$$

which reads as center of α-component of v for N particles. Obviously:

$$
\begin{aligned}
r_{C,\alpha,N+1} &= \frac{\sum_{i=1}^{N+1} |v_{i,\alpha}| r_i}{\sum_{i=1}^{N+1} |v_{i,\alpha}|} \\[2mm]
&= \frac{\sum_{i=1}^{N} |v_{i,\alpha}| r_i + |v_{N+1,\alpha}| r_{N+1}}{\sum_{i=1}^{N} |v_{i,\alpha}| + |v_{N+1,\alpha}|} \\[2mm]
&= \frac{r_{C,\alpha,N} \sum_{i=1}^{N} |v_{i,\alpha}| + |v_{N+1,\alpha}| r_{N+1}}{\sum_{i=1}^{N} |v_{i,\alpha}| + |v_{N+1,\alpha}|} \\[2mm]
&= \frac{r_{C,\alpha,N} \sum_{i=1}^{N} |v_{i,\alpha}| + r_{C,\alpha,N} |v_{N+1,\alpha}| - r_{C,\alpha,N} |v_{N+1,\alpha}| + |v_{N+1,\alpha}| r_{N+1}}{\sum_{i=1}^{N} |v_{i,\alpha}| + |v_{N+1,\alpha}|} \\[2mm]
&= r_{C,\alpha,N} + \frac{|v_{N+1,\alpha}| (r_{N+1} - r_{C,\alpha,N})}{\sum_{i=1}^{N} |v_{i,\alpha}| + |v_{N+1,\alpha}|}
\end{aligned}
$$

Therefor if variable $M_{|v|,\alpha,N} = \sum_{i=1}^{N} |v_{i,\alpha}|$ has already been calculated, the new center of v can be found easily based on the previously calculated values of r_C and $M_{|v|}$:

$$
r_{C,\alpha,N+1} = r_{C,\alpha,N} + \frac{|v_{N+1,\alpha}| (r_{N+1} - r_{C,\alpha,N})}{M_{|v|,\alpha,N} + |v_{N+1,\alpha}|} \tag{A.3}
$$

Similarly, this method can be utilized for the higher order expansion coefficients. *Monopole* term is simply the coefficient of the first term in the Taylor expansion of the objective potential around the center of mass:

$$
M_\alpha = \sum_{i=1}^{N} v_{i,\alpha}
$$

Dipole term is:

$$
\vec{D}_\alpha = \sum_{i} v_{i,\alpha} \left(r_i - r_{C,N,\alpha} \right)
$$

In order to find $D_{\alpha,N+1}$ from $\vec{D}_\alpha$:

$$\vec{D}_{\alpha,N+1}$$

$$= v_{N+1,\alpha}\left(r_{N+1} - r_{C,N+1,\alpha}\right) + \sum_i^N v_{i,\alpha}\left(r_i - r_{C,N+1,\alpha}\right)$$

$$= v_{N+1,\alpha}\left(r_{N+1} - r_{C,N+1,\alpha}\right) + \sum_i^N v_{i,\alpha}\left(r_i - r_{C,\alpha,N} - \frac{|v_{N+1,\alpha}|(r_{N+1} - r_{C,\alpha,N})}{M_{|v|,\alpha,N} + |v_{N+1,\alpha}|}\right)$$

$$= v_{N+1,\alpha}\left(r_{N+1} - r_{C,N+1,\alpha}\right) + \sum_i^N v_{i,\alpha}\left(r_i - r_{C,\alpha,N}\right) - \frac{|v_{N+1,\alpha}|(r_{N+1} - r_{C,\alpha,N})}{M_{|v|,\alpha,N} + |v_{N+1,\alpha}|}\sum_i^N v_{i,\alpha}$$

$$= v_{N+1,\alpha}\left(r_{N+1} - r_{C,N+1,\alpha}\right) + \vec{D}_{\alpha,N} - \frac{|v_{N+1,\alpha}|(r_{N+1} - r_{C,\alpha,N})}{M_{|v|,\alpha,N} + |v_{N+1,\alpha}|}M_{\alpha,N}$$

Further simplification by substitution in the first term:

$$\vec{D}_{\alpha,N+1} = v_{N+1,\alpha}\left(r_{N+1} - r_{C,\alpha,N}\right.$$

$$\left. - \frac{|v_{N+1,\alpha}|(r_{N+1} - r_{C,\alpha,N})}{M_{|v|,\alpha,N} + |v_{N+1,\alpha}|}\right) + \vec{D}_{\alpha,N} - \frac{|v_{N+1,\alpha}|(r_{N+1} - r_{C,\alpha,N})}{M_{|v|,\alpha,N} + |v_{N+1,\alpha}|}M_{\alpha,N}$$

$$= \vec{D}_{\alpha,N} + v_{N+1,\alpha}\left(r_{N+1} - r_{C,\alpha,N}\right) - \frac{|v_{N+1,\alpha}|(r_{N+1} - r_{C,\alpha,N})}{M_{|v|,\alpha,N} + |v_{N+1,\alpha}|}\left(v_{N+1,\alpha} + M_{\alpha,N}\right)$$

$$\vec{D}_{\alpha,N+1} = \vec{D}_{\alpha,N} + v_{N+1,\alpha}\left(r_{N+1} - r_{C,\alpha,N}\right) - \frac{|v_{N+1,\alpha}|(r_{N+1} - r_{C,\alpha,N})}{M_{|v|,\alpha,N} + |v_{N+1,\alpha}|}M_{\alpha,N+1} \quad \text{(A.4)}$$

If $|v_\alpha| = v_\alpha$ then the Dipolar term will become $\vec{D}_{\alpha,N+1} = \vec{D}_{\alpha,N} = \vec{D}_{\alpha,1} = 0$.

Finally the *quadrupole* term (for $1/r$ potential):

$$\bar{\bar{Q}}_{a,N} = 3\sum_{i=1}^N v_{i,a}\left(r_i - r_{C,\alpha,N}\right)\left(r_i - r_{C,\alpha,N}\right) - \sum_{i=1}^N v_{i,a}\left(r_i - r_{C,\alpha,N}\right)\cdot\left(r_i - r_{C,\alpha,N}\right)\bar{\bar{I}}$$

This can be written as:

$$\bar{\bar{Q}}_{\alpha,N} = 3\bar{\bar{S}}_{\alpha,N} - \text{tr}(S_{\alpha,N})\bar{\bar{I}}$$

When a new particle is added to the box, *quadrupole* term must be updated as:

$$\bar{\bar{Q}}_{\alpha,N+1} = 3\bar{\bar{S}}_{\alpha,N+1} - \text{tr}(S_{\alpha,N+1})\bar{\bar{I}}$$

$$
S_{\alpha,N+1} = \left\{
\begin{aligned}
&S_{\alpha,N} + \left(v_{N+1,a} - \left(\frac{|v_{N+1,\alpha}|}{M_{|v|,\alpha,N+1}}\right)^2 M_{\alpha,N+1}\right)(r_{N+1} - r_{C,\alpha,N})(r_{N+1} - r_{C,\alpha,N})\\
&- \left(\frac{|v_{N+1,\alpha}|}{M_{|v|,\alpha,N+1}}\right) D_{\alpha,N+1}(r_{N+1} - r_{C,\alpha,N})\\
&- \left(\frac{|v_{N+1,\alpha}|}{M_{|v|,\alpha,N+1}}\right) [D_{\alpha,N+1}(r_{N+1} - r_{C,\alpha,N})]^{\dagger}
\end{aligned}
\right\}
$$

(A.5)

Rewriting the quadropole equation:

$$
\bar{\bar{Q}}_{\alpha,N+1} =
$$
$$
\bar{\bar{Q}}_{\alpha,N}
$$
$$
+ \left[
\begin{aligned}
&3\left(v_{N+1,a} - \left(\frac{|v_{N+1,\alpha}|}{M_{|v|,\alpha,N+1}}\right)^2 M_{\alpha,N+1}\right)(r_{N+1} - r_{C,\alpha,N})(r_{N+1} - r_{C,\alpha,N})\\
&- 3\left(\frac{|v_{N+1,\alpha}|}{M_{|v|,\alpha,N+1}}\right) D_{\alpha,N+1}(r_{N+1} - r_{C,\alpha,N})\\
&- 3\left(\frac{|v_{N+1,\alpha}|}{M_{|v|,\alpha,N+1}}\right) [D_{\alpha,N+1}(r_{N+1} - r_{C,\alpha,N})]^{\dagger}-\\
&\mathrm{tr}\left(
\begin{aligned}
&\left(v_{N+1,a} - \left(\frac{|v_{N+1,\alpha}|}{M_{|v|,\alpha,N+1}}\right)^2 M_{\alpha,N+1}\right)(r_{N+1} - r_{C,\alpha,N})(r_{N+1} - r_{C,\alpha,N})+\\
&2\left(\frac{|v_{N+1,\alpha}|}{M_{|v|,\alpha,N+1}}\right) D_{\alpha,N+1}(r_{N+1} - r_{C,\alpha,N})
\end{aligned}
\right)\bar{\bar{I}}
\end{aligned}
\right]
$$

defining $C = \left(\frac{|v_{N+1,\alpha}|}{M_{|v|,\alpha,N+1}}\right)$:

$$
\bar{\bar{Q}}_{\alpha,N+1} = \bar{\bar{Q}}_{\alpha,N} + \left[
\begin{aligned}
&3\left(v_{N+1,a} - C^2 M_{\alpha,N+1}\right)(r_{N+1} - r_{C,\alpha,N})(r_{N+1} - r_{C,\alpha,N})\\
&- 3CD_{\alpha,N+1}(r_{N+1} - r_{C,\alpha,N}) - 3C[D_{\alpha,N+1}(r_{N+1} - r_{C,\alpha,N})]^{\dagger}-\\
&\mathrm{tr}\left(
\begin{aligned}
&\left(v_{N+1,a} - C^2 M_{\alpha,N+1}\right)(r_{N+1} - r_{C,\alpha,N})(r_{N+1} - r_{C,\alpha,N})+\\
&2CD_{\alpha,N+1}(r_{N+1} - r_{C,\alpha,N})
\end{aligned}
\right)\bar{\bar{I}}
\end{aligned}
\right]
$$

(A.6)

117

A.2.2   Computationally Efficient Multipole expansion of RPY

The objective here is to calculate the matrix-vector multiplication:

$$F = D \cdot v$$

, where F is the Hydrodynamic force (without the self term),D is hydrodynamic tensor and v is the sum of all forces on the source particle. For RPY matrix at distances greater than the bead diameter D will have the form:

$$F_{\alpha,i} = c_1 \frac{1}{\mathrm{r}_{ij}} v_{j,\alpha} + c_2 \frac{1}{\mathrm{r}_{ij}^3} v_{j,\alpha} + c_1 \frac{r_{ij,\alpha}\left(r_{ij} \cdot v_j\right)}{\mathrm{r}_{ij}^3} - c_2 \frac{3 r_{ij_\alpha}\left(r_{ij} \cdot v_j\right)}{\mathrm{r}_{ij}^5} \qquad \text{(Sum for all the} j \neq i)$$

Substituting r_{ij} in the above formula:

$$F_{\alpha,i} = \sum_j \left(c_1 \frac{1}{\mathrm{r}_{ij}} v_{j,\alpha} + c_2 \frac{1}{\mathrm{r}_{ij}^3} v_{j,\alpha} + c_1 \frac{(r_i - r_j)_\gamma r_{ij,\alpha} v_{j,\gamma}}{\mathrm{r}_{ij}^3} - c_2 \frac{3(r_i - r_j)_\gamma r_{ij,\alpha} v_{j,\gamma}}{\mathrm{r}_{ij}^5} \right)$$

$$F_{\alpha,i} = \begin{bmatrix} c_1 \sum_j \frac{1}{\mathrm{r}_{ij}} v_{j,\alpha} + c_2 \sum_j \frac{1}{\mathrm{r}_{ij}^3} v_{j,\alpha} - c_1 r_{i,\gamma} \sum_j \frac{d}{dr_\alpha}\left(\frac{v_{j,\gamma}}{\mathrm{r}_{ij}}\right) + c_2 r_{i,\gamma} \sum_j \frac{d}{dr_\alpha}\left(\frac{v_{j,\gamma}}{\mathrm{r}_{ij}^3}\right) \\ + c_1 \sum_j \frac{d}{dr_\alpha}\left(\frac{r_{j,\gamma} v_{j,\gamma}}{\mathrm{r}_{ij}}\right) - c_2 \sum_j \frac{d}{dr_\alpha}\left(\frac{r_{j,\gamma} v_{j,\gamma}}{\mathrm{r}_{ij}^3}\right) \end{bmatrix}$$

$$\tag{A.7}$$

$$F_{\alpha,i} = c_1 \phi_{1/r,\alpha,i} + c_2 \phi_{1/r^3,\alpha,i} - c_1 \psi_{1/r,\alpha,i} + c_2 \psi_{1/r^3,\alpha,i} + c_1 \chi_{1/r,\alpha,i} - c_2 \chi_{1/r^3,\alpha,i} \tag{A.8}$$

The above equation defines $\phi(v,r)$, $\psi(v,r)$ and $\chi(v,r)$. Both ϕ and ψ can be constructed from the same multipole moments and sources, therefore reducing the overhead significantly as its shown below. The χ terms also share the same multipole moments and with additional analytical work it's calculation in the code can be merged into one tree built up and force calculation routine. Consider the above

potential at $r_{ij} = r_i - r_j = r_i - r_{c,N} + (r_{c,N} - r_j)$

$$\bar{r}_{ij} = \bar{R}_{i,c} + \delta \bar{R}_{c,N}$$

$$R = \bar{R}_{i,c} \equiv r_i - r_{c,N}$$

$$\delta R = \delta \bar{R}_{c,j} \equiv (r_{c,N} - r_j)$$

Note R is only function of the destination not the sources and it can be factored out of the sum.

$$f_{\alpha,i}(R + \delta R) = \sum_j^N \left[f_{\alpha,i}(R) + \frac{\partial f_{\alpha,i}(r_i)}{\partial r_i}|_{x=R} \cdot \delta R_{c,j} + \frac{1}{2} \delta R \cdot \frac{\partial^2 f_{\alpha,i}(r_i)}{\partial r_i \partial r_i}|_{x=R} \cdot \delta R_{c,j} \right]$$

Therefore:

$$\phi_{1/r,\alpha}(v,r) = \frac{M_\alpha}{R} + \frac{R.D_\alpha}{R^3} + \frac{1}{2}\frac{R.Q_\alpha.R}{R^5} \tag{A.9}$$

$$\phi_{1/r^3,\alpha}(v,r) = \frac{M_\alpha}{R^3} + 3\frac{R.D_\alpha}{R^5} + \frac{15}{2}\frac{R.Q_{1/r^3,\alpha}.R}{R^7} \tag{A.10}$$

With $\bar{M} = \sum_j \bar{v}_j$, $\bar{\bar{D}} = \delta_\alpha \delta_\gamma D_{\alpha\gamma} = \delta_\alpha \delta_\gamma \sum_{j\neq i} v_{j,\alpha}(r_j - r_{c,N})_\gamma$ and $\bar{\bar{Q}} = \sum_{j\neq i}^N v_j(r_j - r_{c,N})(r_j - r_{c,N})$.
Now for the first type of field terms:

$$\psi_{1/r,\alpha,i} = r_i.\frac{d\phi_{1/r}}{dr_\alpha} = r_{i,\gamma}\frac{d\phi_{1/r,\gamma}}{dr_\alpha}$$

$$\frac{d\phi_{1/r,\gamma}}{dr} = \frac{d}{dr_\alpha}\left(\frac{M_\gamma}{R} + \frac{R.D_\gamma}{R^3} + \frac{1}{2}\frac{R.Q_\gamma.R}{R^5} \right)$$

$$\left(\frac{d\phi_{1/r}}{dr} \right)_{\gamma,\alpha} = \frac{d\phi_{1/r,\gamma}}{dr_\alpha} = -\left(\frac{R_\alpha M_\gamma}{R^3} + \frac{3R_\alpha R.D_\gamma}{R^5} - \frac{D_{\gamma,\alpha}}{R^3} + \frac{5}{2}\frac{R_\alpha(R.Q_\gamma.R)}{R^7} - \frac{R_\alpha Q_{\gamma,\alpha}}{R^5} \right)$$

$$\psi_{1/r,\alpha,i} = r_i.\frac{d\phi_{1/r}}{dr_\alpha} = -r_{i,\gamma}\left(\frac{R_\alpha M_\gamma}{R^3} + \frac{3R_\alpha R.D_\gamma}{R^5} - \frac{D_{\gamma,\alpha}}{R^3} + \frac{5}{2}\frac{R_\alpha(R.Q_\gamma.R)}{R^7} - \frac{R.Q_{\gamma,\alpha}}{R^5} \right)$$
$$\tag{A.11}$$

119

$$\psi_{1/r^3,\alpha,i} = r_i \cdot \frac{d\phi_{1/r^3}}{dr_\alpha} = r_{i,\gamma}\frac{d\phi_{1/r^3,\gamma}}{dr_\alpha}$$

$$\frac{d\phi_{1/r^3,\gamma}}{dr} = \frac{d}{dr_\alpha}\left(\frac{M_\gamma}{R^3} + 3\frac{R \cdot D_\gamma}{R^5} + \frac{15}{2}\frac{R \cdot Q_{1/r^3;\gamma} \cdot R}{R^7}\right)$$

$$\frac{d\phi_{1/r^3,\gamma}}{dr_\alpha} = -\left(3\frac{R_\alpha M_\gamma}{R^5} + 15\frac{R_\alpha R \cdot D_\gamma}{R^7} - 3\frac{D_{\gamma,\alpha}}{R^5} + \frac{105}{2}\frac{R_\alpha R \cdot Q_{1/r^3;\gamma} \cdot R}{R^9} - 15\frac{Q_{1/r^3;\gamma,\alpha} \cdot R}{R^7}\right)$$

$$\psi_{1/r^3,\alpha,i} = -r_i \cdot \left(3\frac{R_\alpha M_\gamma}{R^5} + 15\frac{R_\alpha R \cdot D_\gamma}{R^7} - 3\frac{D_{\gamma,\alpha}}{R^5} + \frac{105}{2}\frac{R_\alpha R \cdot Q_{1/r^3;\gamma} \cdot R}{R^9} - 15\frac{Q_{1/r^3;\gamma,\alpha} \cdot R}{R^7}\right)$$

$$\psi_{1/r^3,\alpha,i} = r_{i,\gamma}\frac{d\phi_{1/r^3,\gamma}}{dr_\alpha} =$$
$$-r_{i,\gamma}\left(3\frac{R_\alpha M_\gamma}{R^5} + 15\frac{R_\alpha R \cdot D_\gamma}{R^7} - 3\frac{D_{\gamma,\alpha}}{R^5} + \frac{105}{2}\frac{R_\alpha R \cdot Q_{1/r^3;\gamma} \cdot R}{R^9} - 15\frac{Q_{1/r^3;\gamma,\alpha} \cdot R}{R^7}\right)$$

<div align="right">(A.12)</div>

The last two field terms can be found in a similar fashion, provided that the source term is calculated as $r_j.v_j$:

$$\chi_{1/r,\alpha} = \sum_j \frac{d}{dr_\alpha}\left(\frac{r_{j,\gamma}v_{j,\gamma}}{r_{ij}}\right) = \frac{d\phi_{1/r}(r_j \cdot v_j, r)}{dr_\alpha}$$

$$\chi_{1/r^3,\alpha} = \sum_j \frac{d}{dr_\alpha}\left(\frac{r_{j,\gamma}v_{j,\gamma}}{r_{ij}^3}\right) = \frac{d\phi_{1/r^3}(r_j \cdot v_j, r)}{dr_\alpha}$$

Note that $r_j.v_j$ is scalar therefore in this case the subscript α is removed from the ϕ potential.

$$\chi_{1/r,\alpha} = \sum_j \frac{d}{dr_\alpha}\left(\frac{r_{j,\gamma}v_{j,\gamma}}{r_{ij}}\right) = -\left(\frac{R_\alpha M}{R^3} + \frac{3R_\alpha R.D}{R^5} - \frac{D_\alpha}{R^3} + \frac{5}{2}\frac{R_\alpha(R.Q.R)}{R^7} - \frac{R_\alpha Q_a}{R^5}\right)$$

<div align="right">(A.13)</div>

$$\chi_{1/r^3,\alpha} = \sum_j \frac{d}{dr_\alpha}\left(\frac{r_{j,\gamma}v_{j,\gamma}}{r_{ij}^3}\right) =$$
$$-\left(3\frac{R_\alpha M}{R^5} + 15\frac{R_\alpha R \cdot D}{R^7} - 3\frac{D_\alpha}{R^5} + \frac{105}{2}\frac{R_\alpha R \cdot Q_{1/r^3} \cdot R}{R^9} - 15\frac{Q_{1/r^3,\alpha} \cdot R}{R^7}\right)$$

<div align="right">(A.14)</div>

In χ equations, $M = \sum_j r_j.v_j$, $\bar{D} = \sum_j (r_j.v_j\delta R)$ and $\bar{\bar{Q}} = \sum_j (r_j.v_j\delta R\delta R)$.

Assembling back the force vector from potential and fields

$$F_{\alpha,i} = c_1\phi_{1/r,\alpha,i} + c_2\phi_{1/r^3,\alpha,i} - c_1\psi_{1/r,\alpha,i} + c_2\psi_{1/r^3,\alpha,i} + c_1\chi_{1/r,\alpha,i} - c_2\chi_{1/r^3,\alpha,i}$$

$$F_{\alpha,i} = \begin{cases} c_1\left(\dfrac{M_\alpha}{R} + \dfrac{R\cdot D_\alpha}{R^3} + \dfrac{1}{2}\dfrac{R\cdot Q_\alpha\cdot R}{R^5}\right) \\[2mm] + \dfrac{c_2}{R^2}\left(\dfrac{M_\alpha}{R} + 3\dfrac{R\cdot D_\alpha}{R^3} + \dfrac{15}{2}\dfrac{R\cdot Q_{1/r^3;\alpha}\cdot R}{R^5}\right) \\[2mm] + c_1 r_{i,\gamma}\left(\dfrac{R_\alpha M_\gamma}{R^3} + \dfrac{3R_\alpha R\cdot D_\gamma}{R^5} - \dfrac{D_{\gamma,\alpha}}{R^3} + \dfrac{5}{2}\dfrac{R_\alpha(R\cdot Q_\gamma\cdot R)}{R^7} - \dfrac{Q_{\gamma,\alpha}\cdot R}{R^5}\right) \\[2mm] - c_2 r_{i,\gamma}\left(\begin{array}{l}3\dfrac{R_\alpha M_\gamma}{R^5} + 15\dfrac{R_\alpha R\cdot D_\gamma}{R^7} - 3\dfrac{D_{\gamma,\alpha}}{R^5} + \dfrac{105}{2}\dfrac{R_\alpha R\cdot Q_{1/r^3;\gamma}\cdot R}{R^9} \\[2mm] - 15\dfrac{Q_{1/r^3;\gamma,\alpha}\cdot R}{R^7}\end{array}\right) \\[2mm] - c_1\left(\dfrac{R_\alpha m}{R^3} + \dfrac{3R_\alpha R.d}{R^5} - \dfrac{d_\alpha}{R^3} + \dfrac{5}{2}\dfrac{R_\alpha(R.q.R)}{R^7} - \dfrac{R_\alpha\cdot q_a}{R^5}\right) \\[2mm] + c_2\left(3\dfrac{R_\alpha m}{R^5} + 15\dfrac{R_\alpha R\cdot d}{R^7} - 3\dfrac{d_\alpha}{R^5} + \dfrac{105}{2}\dfrac{R_\alpha R\cdot q_{1/r^3}\cdot R}{R^9} - 15\dfrac{q_{1/r^3,\alpha}\cdot R}{R^7}\right) \end{cases}$$

$$\text{(A.15)}$$

It is also possible to rewrite the cell (multipole) contribution to the force in terms of matrix-vector multiplication which is only practical up to the dipole term.

A.3 Fully implicit corrector step of bead-spring BD simulation

Definitions

n_s: Number of entropic springs

n_b: Number of beads $= n_s + 1$

R: Bead position vector of $3n_b$ members. Laid out as :

$$
\begin{bmatrix}
x_{bead=1} & y_{bead=1} & z_{bead=1} & x_{bead=2} & y_{bead=2} & \cdot_{\cdots} & y_{bead=n_b} & z_{bead=n_b}
\end{bmatrix}^{\dagger}
$$

r_{ij}: Bead to bead vector of 3 members $=R_i - R_j$

Q: Connector vector with $3n_s$ elements $=r_{v+1,v}$

F: Spring force vector of $3n_s$ members, (e.g. for the dimensionless FENE $=\frac{Q}{1-\frac{Q \cdot Q}{b}}$

)

I : Identity matrix of rank $3n_s$

ι: Identity matrix of rank 3

Ω: RPY diffusion tensor with elements

$$
\Omega_{ij} =
\begin{cases}
\frac{3a}{4|r_{ij}|} \left[\left(1 + \frac{2a^2}{3|r_{ij}|^2}\right) \iota + \left(1 - \frac{2a^2}{|r_{ij}|^2}\right) \frac{r_{ij}r_{ij}}{|r_{ij}|^2} \right] & r_{ij} \geq 2a \\[3ex]
\left[\left(1 - \frac{9|r_{ij}|}{32a}\right) \iota + \left(\frac{3}{32a|r_{ij}|}\right) r_{ij}r_{ij} \right] & r_{ij} < 2a
\end{cases}
$$

$$
\Upsilon = \frac{kT dt}{\zeta} (I+\Omega) = \mathsf{S} \cdot \mathsf{S}^{\dagger}
$$

with dt defined as magnitude of time step (In non dimensional format:$\Upsilon=\frac{dt}{4}(I+\Omega)$)

B: Grand Rouse matrix $(3n_s \times 3n_b)$ =
$$
\begin{bmatrix}
-\iota & \iota & o & o & o \\[2ex]
o & -\iota & \iota & o & o \\[2ex]
o & o & \ddots & \ddots & o \\[2ex]
o & o & o & -\iota & \iota
\end{bmatrix}
$$

122

K: Tridiagonal Grand κ matrix of rank $3n_s$ (In non dimensional diagonal terms are consisting of $dt\mathrm{Pe}\kappa_{3\times3}$)

W: Vector with $3n_b$ Gaussian random number with variance of $\frac{1}{2dt}$

Formulation

Subsequent to nondimensionalization, for predictor step:

$$Q^* = Q^n + \mathrm{K} \cdot Q - \mathrm{B} \cdot \Upsilon \cdot \mathrm{B}^\dagger \cdot F + \mathrm{B} \cdot \mathsf{S} \cdot W$$

If now we define:

$$\mathrm{M} = \mathrm{B} \cdot \Upsilon \mathrm{B}^\dagger = \Sigma \cdot \Sigma^\dagger = \mathrm{B} \cdot \mathsf{S} \cdot \mathsf{S}^\dagger \cdot \mathrm{B}^\dagger$$

Diagonal terms of M are:

Diagonal terms of M are found to be :

$$\mathrm{M}_{ii} = -2\Upsilon_{i,i+1} + \Upsilon_{i+1,i+1} + \Upsilon_{i,i} = 2\iota - 2\Upsilon_{i,i+1}$$

$$2\Upsilon_{i,i+1} = 2dt\Omega_{i,i+1} = \begin{cases} \frac{3adt}{2|Q_i|}\left[\left(1 + \frac{2a^2}{3|Q_i|^2}\right)\iota + \left(1 - \frac{2a^2}{|Q_i|^2}\right)\frac{Q_iQ_i}{|Q_i|^2}\right] & r_{ij} \geq 2a \\[3mm] 2dt\left[\left(1 - \frac{9|Q_i|}{32a}\right)\iota + \left(\frac{3}{32a|Q_i|}\right)Q_iQ_i\right] & r_{ij} < 2a \end{cases} \tag{A.16}$$

In the corrector step, segment s will be updated according to the following equation:

$$Q_s^{**} + \mathrm{M}_{ss} \cdot F_s^{**} = Q_s^n + \frac{1}{2}\left(\mathrm{K}_{ss} \cdot Q_s^* + \mathrm{K}_{ss} \cdot Q_s^n\right) + \mathrm{M}_{s,1:s-1} \cdot F_{1:s-1}^{**} + \mathrm{M}_{s,s+1:n_s} \cdot F_{s+1:n_s}^* + \Sigma \cdot W \tag{A.17}$$

The coefficient of F^{**} is explicitly determined in the established approach. The rest of this appendix proves that this inconsistency in the semi-implicit method can be resolved for FENE force law, or in general, for any force law that is formulated in terms of a real function. At the end of each iteration, values of Q^* are replaced by those of Q^{**}. If iteration converges under the imposed tolerance the variables are

123

substituted in Q^{n+1}. For the FENE chain with C_s^* defined as the right hand side of eq. A.17:

$$Q_s^{**} + \frac{\mathrm{M}_{ss} \cdot Q_s^{**}}{1 - \frac{|Q_s^{**}|^2}{b}} = C_s^*$$

$$\left(1 - \frac{|Q_s^{**}|^2}{b}\right) Q_s^{**} + \mathrm{M}_{ss} \cdot Q_s^{**} = C_s^* \left(1 - \frac{|Q_s^{**}|^2}{b}\right)$$

Substitution for M_{ss}:

$$\left(1 - \frac{|Q_s^{**}|^2}{b}\right) Q_s^{**} + (2\iota - 2\Upsilon_{i,i+1}) \cdot Q_s^{**} = C_s^* \left(1 - \frac{|Q_s^{**}|^2}{b}\right)$$

$$\left(3 - \frac{|Q_s^{**}|^2}{b}\right) Q_s^{**} - 2\Upsilon_{i,i+1} \cdot Q_s^{**} = C_s^* \left(1 - \frac{|Q_s^{**}|^2}{b}\right)$$

For $Q_s > 2a$:

$$\left(3 - \frac{|Q_s^{**}|^2}{b}\right) Q_s^{**}$$
$$- dt \frac{3a}{2} \left[\left(1 + \frac{2a^2}{3|Q_s|}\right) \iota + \left(1 - \frac{2a^2}{|Q_s|^2}\right) Q_s Q_s\right] \cdot Q_s^{**} = C_s^* \left(1 - \frac{|Q_s^{**}|^2}{b}\right)$$

$$\left(3 - \frac{|Q_s^{**}|^2}{b}\right) Q_s^{**}$$
$$- \frac{3adt}{2} \left[\left(1 + \frac{2a^2}{3|Q_s^{**}|}\right) \iota \cdot Q_s^{**} + \left(1 - \frac{2a^2}{|Q_s^{**}|^2}\right) Q_s^{**}Q_s^{**} \cdot Q_s^{**}\right] = C_s^* \left(1 - \frac{|Q_s^{**}|^2}{b}\right)$$

$$\tag{A.18}$$

At the last step we have introduced M_s^{**} instead of M_s^n. This is more accurate since now the largest value of mobility tensor is calculated implicitly. In any case, since $\nabla \cdot \Upsilon = 0$ and for small δt, this modification affects accuracy of order $\mathrm{O}\left((dt)^2\right)$ which is negligible. Now using identity $\delta_i \delta_j \cdot \delta_k = \delta_i \left(\delta_j \cdot \delta_k\right)$, Eq. A.18 becomes:

$$\left(3 - \frac{|Q_s^{**}|^2}{b}\right) Q_s^{**} -$$
$$\frac{3adt}{2} \left[\left(1 + \frac{2a^2}{3|Q_s^{**}|}\right) \iota \cdot Q_s^{**} + \left(1 - \frac{2a^2}{|Q_s^{**}|^2}\right) Q_s^{**}|Q_s^{**}|^2\right] = C_s^* \left(1 - \frac{|Q_s^{**}|^2}{b}\right)$$

$$\left(3 - \frac{|Q_s^{**}|^2}{b}\right) Q_s^{**} -$$

$$\frac{3adt}{2} \left(1 + \frac{2a^2}{3|Q_s^{**}|}\right) Q_s^{**} - \frac{3adt}{2} Q_s^{**}|Q_s^{**}|^2 + \frac{2a^2}{|Q_s^{**}|^2} Q_s^{**}|Q_s^{**}|^2 = C_s^* \left(1 - \frac{|Q_s^{**}|^2}{b}\right)$$

Now we can easily take the magnitude of both sides to be equal:

$$\left(3 - \frac{|Q_s^{**}|^2}{b}\right) |Q_s^{**}| -$$

$$\frac{3adt}{2} \left(1 + \frac{2a^2}{3|Q_s^{**}|}\right) |Q_s^{**}| - \frac{3adt}{2} |Q_s^{**}||Q_s^{**}|^2 + 2a^2|Q_s^{**}| = |C_s^*| \left(1 - \frac{|Q_s^{**}|^2}{b}\right)$$

For convenience we define $q = Q_s^{**}$ and $c = |C_s^*|$ then:

$$\left(3 - \frac{q^2}{b}\right) q - \frac{3adt}{2} \left(1 + \frac{2a^2}{3q}\right) q - \frac{3adt}{2} q^3 + 2a^2 q = c \left(1 - \frac{q^2}{b}\right)$$

$$2 \left(3b - q^2\right) q - 3abdt \left(1 + \frac{2a^2}{3q}\right) q - 3abdtq^3 + 4a^2bq = 2c \left(b - q^2\right)$$

$$6 \left(3b - q^2\right) q - 3abdt \left(3q + 2a^2\right) - 9abdtq^3 + 12a^2bq = 6c \left(b - q^2\right)$$

$$\left(18bq - 6q^3\right) - \left(9abdtq + 6a^3bdt\right) - 9abdtq^3 + 12a^2bq = 6bc - 6cq^2$$

$$\left(18bq - 6q^3\right) - \left(9abdtq + 6a^3bdt\right) - 9abdtq^3 + 12a^2bq - 6bc + 6cq^2 = 0$$

$$\left(-6 - 9abdt\right) q^3 + 6cq^2 + \left(18b - 9abdt + 12a^2b\right) q - 6a^3bdt - 6bc = 0$$

$$q^3 - \frac{2c}{2 + 3abdt} q^2 - \frac{\left(6b - 3abdt + 4a^2b\right)}{2 + 3abdt} q + \frac{2a^3bdt + 2bc}{2 + 3abdt} = 0 \tag{A.19}$$

Eq. A.19 is the new cubical equation for multi segment chain with HI when $q \geq 2a$.

For the case where $q < 2a$ similar treatment yields:

$$\left(3 - \frac{|Q_s^{**}|^2}{b}\right) Q_s^{**} - 2 \left[\left(1 - \frac{9|Q_s^{**}|}{32a}\right) \iota + \left(\frac{3}{32a|Q_s^{**}|}\right) Q_s^{**} Q_s^{**}\right] \cdot Q_s^{**} = C_s^* \left(1 - \frac{|Q_s^{**}|^2}{b}\right)$$

$$\left(3 - \frac{|Q_s^{**}|^2}{b}\right) Q_s^{**} - 2 \left(1 - \frac{9|Q_s^{**}|}{32a}\right) Q_s^{**} - 2 \left[\left(\frac{3}{32a|Q_s^{**}|}\right) Q_s^{**} Q_s^{**} \cdot Q_s^{**}\right] = C_s^* \left(1 - \frac{|Q_s^{**}|^2}{b}\right)$$

$$\left(3 - \frac{|Q_s^{**}|^2}{b}\right) Q_s^{**} - 2\left(1 - \frac{9|Q_s^{**}|}{32a}\right) Q_s^{**} - \left(\frac{6|Q_s^{**}|}{32a}\right) Q_s^{**} = C_s^* \left(1 - \frac{|Q_s^{**}|^2}{b}\right)$$

$$\left(3 - \frac{|Q_s^{**}|^2}{b} - 2 + \frac{18|Q_s^{**}|}{32a} - \frac{6|Q_s^{**}|}{32a}\right) Q_s^{**} = C_s^* \left(1 - \frac{|Q_s^{**}|^2}{b}\right)$$

$$\left(1 - \frac{q^2}{b} + \frac{12q}{32a}\right) q = c\left(b - q^2\right)$$

$$\left(b - q^2 + \frac{12bq}{32a}\right) q = c\left(b - q^2\right)$$

$$q^3 - \left(\frac{12b}{32a} + c\right) q^2 - bq + cb = 0 \qquad\qquad \text{(A.20)}$$

Vita

Mahdy Malekzadeh Moghani was born in Mashhad, Iran in 1982. He attended the Amirkabir University of Technology (Tehran Polytechnic) and received his B.Sc. degree in Polymer Engineering. Later he continued his education at the M.Sc. level in polymer engineering field at the Iran Polymer and Petrochemical Institute, a research center focused on graduate level education and advanced research. In 2008, he joined the University of Tennessee Chemical and Biomolecular Enginnering program where he received his M.Sc. and PhD. During his academic career Mahdy has been focused on the application of various computational methods towards fundamental understanding of polymeric and colloidal materials to enhance industrial processes and development of new polymeric materials' functionality. Mahdy has maintained a keen and persistent interest in Rheology, numerical methods for material modeling, computational techniques and chocolates.